WWU
MÜNSTER

Background reduction by the inner wire electrode and set-up of the condensed krypton source at the neutrino mass experiment KATRIN

Stephan Dyba, Dissertation 2018

wissen.leben
WWU Münster

Institut für Kernphysik
Westfälische Wilhelms-Universität Münster

Experimentelle Physik

Dissertationsthema

Background reduction by the inner wire electrode and set-up of the condensed krypton source at the neutrino mass experiment KATRIN

Inaugural-Dissertation
zur Erlangung des Doktorgrades der Naturwissenschaften
im Fachbereich Physik
der Mathematisch-Naturwissenschaftlichen Fakultät
der Westfälischen Wilhelms-Universität Münster

vorgelegt von
Stephan Dyba
aus Lingen (Ems)

— 2018 —
(überarbeitete Version, Januar 2019)

WWU
MÜNSTER

Dekan: Prof. Dr. Gerhard Wilde

Erster Gutachter: Prof. Dr. Christian Weinheimer

Zweiter Gutachter: Prof. Dr. Anton Andronic

Tag der mündlichen Prüfung: 29.01.2019

Tag der Promotion: 29.01.2019

Per aspera ad astra.

— Seneca, *Hercules Furens*

Abstract

Since the observation of neutrino oscillations proved that neutrinos have a mass [Nob15], the experimental efforts to measure this property have increased. The neutrino mass is an important parameter in astrophysics and cosmology, as well as in nuclear and particle physics. A model independent method to measure the average neutrino mass (m_{ν_e}) can be achieved by precise investigation of the endpoint region of the β-decay spectrum. Measurements with tritium as β-emitter, applying an electrostatic filter of the MAC-E type, provide the lowest upper limit for this observable to the present day. Experiments in Mainz and Troitsk independently deduced an upper limit of ~2 eV.

With the **KA**rlsruhe **TRI**tium **N**eutrino experiment (KATRIN) an improvement of this limit by one order of magnitude is anticipated, corresponding to a mass sensitivity of 0.2 eV (90% C.L.). The β-electrons are emitted in a Windowless Gaseous Tritium Source (WGTS), guided through a transport section to eliminate tritium flow towards the spectrometers and are analyzed by a tandem of MAC-E filter type spectrometers. Inside the main spectrometer, a wire electrode system is integrated to reduce background from secondary electrons originating from the vessel hull and shape the electric potential inside the spectrometer.

During baking the spectrometer, in order to improve the vacuum conditions, the ability to fully use the wire electrode in a double layer mode has been partially lost by short circuits. In a repair attempt, the functionality of the double layer could be partially restored. Measurements with a partially operative double layer to investigate background rates, are covered within this thesis.

During first commissioning measurements with the KATRIN main spectrometer it has been found, that the overall background level exceeds the anticipated design goal. Various test measurements and detailed analysis lead to an understanding of numerous background sources, but could not provide a complete picture. This work covers the measurement of a shift of the MAC-E filter analyzing plane towards the spectrometer entrance and exit, in order to characterize the volume dependency of the background and to test measurement settings, which can reduce this background. For this purpose alternative potential configurations of the inner wire electrode and the aircoil system have been investigated. Furthermore the shifted analyzing plane enables a spectroscopic measurement of the overall background energy composition.

Since the KATRIN experiment relies on a ultra precise high voltage system to reach the anticipated neutrino mass sensitivity, calibration sources are required. The **C**ondensed **Kr**ypton **S**ource provides a nuclear standard by the monoenergetic conversion electrons of a thin condensed $^{83\mathrm{m}}$Kr film. The source can be moved within the complete magnetic flux tube of the CPS beam tube and therefore illuminate individual pixels of the detector system. Within this work, the set-up and commissioning of the CKrS will be discussed. During the krypton measurement campaign in 2017, the performance of the CKrS regarding rate and energy stability was demonstrated and spectroscopic measurements of various conversion electron lines were performed.

Zusammenfassung

Seit der Nachweis von Neutrinooszillationen gezeigt hat, dass Neutrinos eine Masse besitzen [Nob15], wurden die experimentellen Bemühungen diese zu messen verstärkt. Die Neutrinomasse ist ein wichtiger Parameter in der Astrophysik und Kosmologie, aber auch in der Kern- und Teilchenphysik. Eine modellunabhängige Bestimmung der mittleren Neutrinomasse (m_{ν_e}) kann durch präzise Vermessung der Enpunktregion des β-Zerfallsspektrums erreicht werden. Messungen des Tritium β-Spektrums mit einem elektrostatischen MAC-E Filter liefern derzeit die niedrigste Obergrenze für direkte Neutrinomassenexperimente. Die Experimente in Mainz und Troitsk haben unabhängig voneinander eine Obergrenze von ~2 eV bestimmt.

Mit dem **KA**rlsruhe **TRI**tium **N**eutrino Experiment (KATRIN) wird eine verbesserte Massensensitivität von 0.2 eV (90% C.L.) angestrebt. Die β-Elektronen werden hierbei in einer fensterlosen, gasförmigen Tritiumquelle (engl.: WGTS) emittiert, entlang eines Transportsystems zur Reduktion des Tritiumflusses transportiert und anschließend in einem Tandem aus MAC-E Filtern anhand ihrer Energie gefiltert. Innerhalb des Hauptspektrometers befindet sich ein Drahtelektrodensystem, das dazu dient Sekundärelektronen, die in der Spektrometerhülle entstehen, zu unterdrücken und das elektrische Feld im Inneren des Spektrometers zu formen.

Aufgrund einer Ausheizphase des Spektrometers, die dazu diente das Vakuum zu verbessern, ist die Möglichkeit die Drahtelektrode vollständig in einem zweilagigen Modus zu betreiben nicht mehr nutzbar. In einem Reparaturversuch konnte die Doppellagigkeit teilweise wieder hergestellt werden. In dieser Arbeit werden die doppellagige Drahtelektrode und Untergrundmessungen mit dieser besprochen.

Während der ersten Inbetriebnahme des KATRIN Experiments wurde festgestellt, dass die Untergrundrate die angestrebten Designwerte überschreitet. Viele Untersuchungen und Analysen haben zu einem weitgehenden Verständnis verschiedener Untergrundprozesse geführt, können diese aber nicht vollständig erklären. In dieser Arbeit werden Messungen mit einer verschobenen Analysierebene des MAC-E Filters vorgestellt, um die Volumenabhängigkeit des Untergrunds zu untersuchen und mögliche Betriebsmodi zu testen, mit denen dieser Untergrund reduziert werden kann. Um dies durchzuführen werden alternative Potentialeinstellungen der Drahtelektrode und des Luftspulensystems untersucht. Weiterhin ermöglicht die verschobene Analysierebene eine Spektroskopie der energetischen Untergrundzusammensetzung.

Das KATRIN Experiment ist von einem ultra präzisen Hochspannungssystem abhängig, um die angestrebte Sensitivität zu erreichen und benötigt daher Kalibrationsquellen. Die kondensierte Kryptonquelle (engl.: CKrS) liefert monoenergetische Konversionselektronen von einem dünnen kondensierten $^{83\mathrm{m}}$Kr Film. Diese Quelle kann im gesamten magnetischen Flussschlauch im Strahlrohr der CPS bewegt werden und so individuelle Pixel des Detektorsystems (FPD) ausleuchten. In dieser Arbeit wird der Aufbau und die Inbetriebnahme der CKrS erörtert. Ferner war es möglich in der Krypton Messkampagne 2017 die Leistungsfähigkeit der CKrS im Bezug auf Raten und Energiestabilität zu demonstrieren und spektroskopische Messungen der verschiedenen Konversionselektronenlinien durchzuführen.

Contents

Chapter 1

Introduction to neutrino physics

1.1 History of neutrino physics

Around the beginning of the last century radioactive decays of atoms have been discovered and were intensively investigated. The β-decay was initially assumed to be a two-body process, resulting in a monochromatic line in the energy spectrum. Investigations by L. Meitner and O. Hahn indicated a continuous spectrum instead, which was confirmed by J. Chadwick in 1914 [Cha14]. This finding appeared to represent a violation of the fundamental principle of energy and momentum conservation.

First through W. Pauli in 1930 this contradiction found a possible solution. He postulated a new particle, called "neutron" at the time, converting the former two-body decay to a three-body type [Pau30], thus preserving the fundamental conservation laws. This particle should be electrically neutral, have spin ½ and interact on a weaker scale with all other particles since it was not observed beforehand. Furthermore he assumed the new particle to have a rest mass of the order of the electron rest mass.

Within the following years E. Fermi renamed the particle to "neutrino" and introduced a theoretical description for the shape of the β-spectrum [Fer34]. In his so-called "golden rule" the rate of electrons produced within a certain energy interval is proportional to the nuclear matrix element of the transition and a phase space factor, which, among others, contains the mass of the neutrino proceed alongside the electron in the decay. The neutrino mass has the largest influence on the spectral shape at the very end of the β-spectrum, the position with maximal electron energy. Hence a precise measurement of the endpoint shape of the spectrum allows a determination of the neutrino mass.

The experimental confirmation for the existence of the neutrino succeeded in 1956 in the Poltergeist experiment, performed by C. Cowan and F. Reines [CRH$^+$56]. This measurement was the successor of the experiment "Herr Auge", which was not conclusive regarding the extraction of a neutrino signal. The Poltergeist experiment was dedicated to the direct detection of electron neutrinos and therefore placed near the Savannah River nuclear power plant. Here a high flux of neutrinos from the reactor was utilizable. In this experiment the inverse β-decay was chosen as detection principle:

$$p + \bar{\nu}_e \longrightarrow n + e^+ \,. \tag{1.1}$$

Therefore two tanks, filled with a water and cadmium chloride mixture, were stacked in a sandwich-like set-up between scintillation light detectors. The protons in the water represented the target for the incoming neutrino beam. The interaction of the neutrino leads to a generation of a neutron and positron. Shortly after the interaction the positron annihilates with an electron, creating two 511 keV photons propagating with an angle of 180°, which can be detected. The neutron thermalizes within a few microseconds and gets captured by cadmium. In this process a third photon is emitted. With the delayed coincidence of the signals, this technique provides a good background rejection and allows to measure the small amount of neutrino interactions. F. Reines were awarded with the Nobel price in 1995 for their groundbreaking finding [Nob95].

The knowledge of neutrinos and particle physics in general was vastly expanded by numerous experiments since the discovery of the neutrino. At present, the standard model of particle physics represents a comprehensive theory for elementary particles and interactions at different energy scales with tremendous precision. Still it is clear that the standard model is not complete since the neutrino obtains no mass within this theory.

1.2 The standard model and neutrino oscillation

In the following section, neutrino oscillations, mass and the relation to the standard model of particle physics will be discussed. The standard model includes 6 quarks and 6 leptons, which are represented in table 1.1. Additionally every particle has a corresponding anti-particle with a charge of the opposing sign, but equivalent spin and mass. The leptonic sector holds the electron, muon and tau and their three associated neutrino flavors. Each lepton and neutrino form a weak isospin doublet, which can be arranged into three different generations (I., II. and III.). The 6 quarks do not form pure weak isospin

Table 1.1: Fermions and anti-fermions of the standard model.

	I.		II.		III.	
quarks	u	$\bar{\mathrm{u}}$	c	$\bar{\mathrm{c}}$	t	$\bar{\mathrm{t}}$
	d'	$\bar{\mathrm{d}}'$	s'	$\bar{\mathrm{s}}'$	b'	$\bar{\mathrm{b}}'$
leptons	e^-	e^+	μ^-	μ^+	τ^-	τ^+
	ν_e	$\bar{\nu}_\mathrm{e}$	ν_μ	$\bar{\nu}_\mu$	ν_τ	$\bar{\nu}_\tau$

doublets, but eigenstates of the strong interaction. Their weak partners, a mixture of strong eigenstates, for instance the d', consists of fractions of d, s and b eigenstates. A proper relation between weak eigenstates and eigenstates of the strong interaction was found as a mixing matrix. This so-called CKM matrix was derived by N. Cabbibo, M. Kobayashi and T. Maskawa and rewarded with the Nobel price in 2008 [Nob08]:

$$\begin{pmatrix} \mathrm{d}' \\ \mathrm{s}' \\ \mathrm{b}' \end{pmatrix} = U_{\mathrm{CKM}} \cdot \begin{pmatrix} \mathrm{d} \\ \mathrm{s} \\ \mathrm{b} \end{pmatrix} . \tag{1.2}$$

The mediators of the fundamental forces within the standard model are γ, $\mathrm{W}^\pm$, Z^0, g and H bosons. The latter Higgs boson named after P. Higgs, who predicted the particle in the 1960s, was experimentally observed in 2012 by the Large Hadron Collider experiments ATLAS [col12a] and CMS [col12b]. This particle is the mediator of the Higgs field, that introduces mass to the fundamental particles.

A similar case of mixing is found for the leptons, where three flavor states of the neutrinos are connected to mass eigenstates. The flavors correspond to the eigenstates of the weak interaction. For this case B. Pontecorvo, Z. Maki, M. Nakagawa and S. Sakata formulated the PNMS mixing matrix [M⁺62], leading to the following equation:

$$\begin{pmatrix} \nu_\mathrm{e} \\ \nu_\mu \\ \nu_\tau \end{pmatrix} = U_{\mathrm{PNMS}} \cdot \begin{pmatrix} \nu_1 \\ \nu_2 \\ \nu_3 \end{pmatrix} . \tag{1.3}$$

The PNMS matrix itself can be expressed by three matrices, which represent three mixing angles θ_{ij} and a CP-violating phase δ [OW08]:

$$U_{\mathrm{PNMS}} = \begin{pmatrix} 1 & 0 & 0 \\ 0 & c_{23} & s_{23} \\ 0 & -s_{23} & c_{23} \end{pmatrix} \begin{pmatrix} c_{13} & 0 & s_{13}e^{i\delta} \\ 0 & 1 & 0 \\ -s_{13}e^{i\delta} & 0 & c_{13} \end{pmatrix} \begin{pmatrix} c_{12} & s_{12} & 0 \\ -s_{12} & c_{12} & 0 \\ 0 & 0 & 1 \end{pmatrix} . \tag{1.4}$$

Herein s_{ij} and c_{ij} are abbreviations for $\sin(\theta_{ij})$ and $\cos(\theta_{ij})$. On the assumption, that the phase δ is non-zero, a CP-violation likewise observed in the quark sector is introduced. Up to now, the phase is not known, but future oscillation experiments could have the ability to obtain this value.

In nature neutrinos are generated in one of three flavor eigenstates $|\nu_\alpha\rangle$ by the weak interaction. The produced flavor state is a superposition of the mass eigenstates:

$$|\nu_\alpha\rangle = \sum_i U_{\alpha i}|\nu_i\rangle \,. \tag{1.5}$$

If the latter have different, non-zero masses, neutrino oscillations are introduced in the propagation of the flavor states. This is due to the different phase velocities of the mass eigenstates, which are represented by:

$$|\nu_i(t)\rangle = e^{-iE_i t}|\nu_i\rangle \,, \tag{1.6}$$

with $E_i = \sqrt{p_i^2 + m_i^2}$ and $\hbar = c = 1$. Thus the neutrino flavor can change during propagation.

Carried on by the previous considerations, the probability for a pure neutrino flavor to change from a state α to β while propagating through vacuum for a given time t can be expressed as:

$$P(\alpha \to \beta, t) = \left| \sum_i U_{\beta i} e^{-iE_i t} U^*_{\alpha i} \right|^2 \,. \tag{1.7}$$

As a demonstrative approach, the formalism is reduced to a set of two neutrino flavors, α and β, and mass eigenstates ν_1 and ν_2. Hence the mixing is scaled down to one mixing angle ϑ and one squared mass difference $\Delta m^2_{21} \equiv m^2_2 - m^2_1$. By equation 1.7 and the previous consideration, the probability for the transition is

$$P(\alpha \to \beta) = \sin^2(2\vartheta) \sin^2\left(\frac{\Delta m^2_{21}}{4} \frac{L}{E}\right) \,, \tag{1.8}$$

wherein E denotes the neutrino energy and L the path length. In figure 1.1 the three neutrino flavor case is visualized as described by equation 1.7. The amplitude of oscillation is determined by the mixing angle, while the frequency depends on the squared mass difference. A measurement of the flavor composition at different distances gives access to both depending parameters. However a determination of the absolute neutrino mass is not possible with experiments measuring the oscillation behavior.

To probe the parameter space of neutrino oscillation, various experiments have been developed and performed, considering all neutrino flavors and

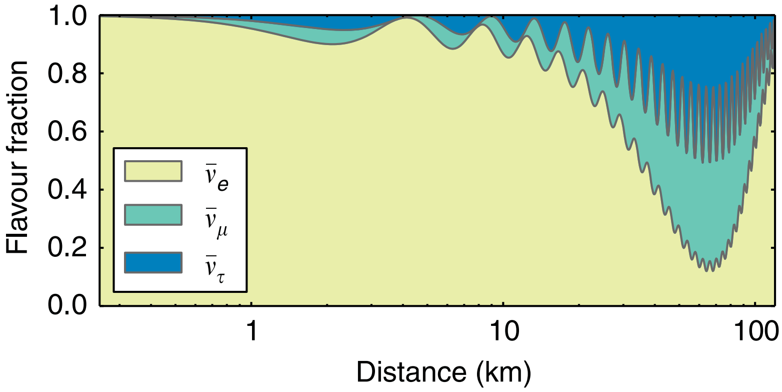

Figure 1.1: Composition of flavor eigenstates within a neutrino beam during propagation. The flavor of an incoming beam of $4\,\mathrm{MeV}$ $\bar{\nu}_\mathrm{e}$'s changes with increasing distance to the source. Figure from [V+15].

eigenstates. During the 1960s, R. Davis found the first experimental hints for neutrino oscillation in the Homestake experiment. Davis, as well as M. Koshiba and R. Giaconni were awarded with the Nobel price in 2002 for their discoveries [Nob02]. The Homestake experiment was designed to observe the flux of solar ν_e neutrinos originating from the sun's nuclear fusion processes by radiochemical methods. The measurements revealed that only 30 % of the predicted flux has been detected [C+98]. This lack of rate was later called the *solar neutrino problem*, because at the time it could not be clarified if the underlying model was incorrect or the experiment deficient.

A conclusion to the problem was introduced, when the Super-Kamiokande succeeded in a direct observation of neutrino oscillation in 1998 [F+98]. With this experiment it was possible to measure the flux of two different flavors, ν_e and ν_μ, of atmospheric neutrinos. Further validation was introduced by the SNO experiment in 2002, that made the total flux off all three flavors of solar neutrinos accessible [AAA+02] [AAB+04]. In the field of reactor and accelerator neutrinos, oscillation was also observed in dedicated experiments, like KamLand [AEE+05] and K2K [AAA+06].

Due to recent reactor experiments, Daya Bay [A+12c], Double Chooz [A+12a] and RENO [A+12b], the parameter space of neutrino oscillation was further explored, presenting a complete picture of all mixing angles and mass splittings. However the mass hierarchy, the CP-violating phase δ and the possibility of Majorana nature of neutrinos remain unknown up to now. In table 1.2 the current measurement values and uncertainties of said parameters are given.

When looking at the standard model of particle physics, the neutrino mass is not included per default. The standard model introduces mass by a coupling of left-handed fermion isospin doublets with right-handed fermion singlets to

Table 1.2: Current parameter values of neutrino oscillation. The indications of NH and IH represent normal and inverted mass hierarchy. This differentiation has to be acknowledged, since the sign of Δm^2_{23} still remains unknown [OG14].

mixing angles		mass splitting	
$\sin^2(2\theta_{12})$	$0.846(21)$	Δm^2_{21}	$7.53(15) \cdot 10^{-5}\,\mathrm{eV}^2$
$\sin^2(2\theta_{23})$	$\begin{cases} 0.999(2)\,\text{[NH]} \\ 1.000(2)\,\text{[IH]} \end{cases}$	$\lvert\Delta m^2_{23}\rvert$	$\begin{cases} 2.42(6) \cdot 10^{-3}\,\mathrm{eV}^2\,\text{[NH]} \\ 2.49(6) \cdot 10^{-3}\,\mathrm{eV}^2\,\text{[IH]} \end{cases}$
$\sin^2(2\theta_{13})$	$8.5(5) \cdot 10^{-2}$	Δm^2_{13}	$\approx \lvert\Delta m^2_{23}\rvert$

the Higgs doublet. This mechanism is called *Yukawa coupling* and describes the mass of all fermions. By contrast, there are left-handed (ν_{L}) neutrinos and right-handed ($\bar{\nu}_{\mathrm{R}}$) anti-neutrinos, which have no other-handed singlet partners. Therefore, the neutrino mass is not generated within the framework of the standard model.

In order to resolve the missing neutrino mass, right-handed neutrinos and respectively left-handed anti-neutrinos can be postulated. These allow an introduction of Dirac mass terms, which produce a mass, but also require a-priori parameters, e.g. extremely small coupling constants to generate the small neutrino masses. Another possibility is presented, if the neutrino is a Majorana particle, i.e. neutrinos are their own anti-particles. In this case, additional "Majorana" mass terms are added to the Lagrangian, that can explain the observed small neutrino masses. In this formalism a heavy right-handed neutrino and a light left-handed neutrino per generation is created. Due to the asymmetry between both masses, this mechanism is called *see-saw type I*, because one neutrino mass is pushed upwards by the other. A third prominent formalism, *see-saw type II*, announces an additional Higgs triplet providing neutrino masses by symmetry breaking. In super-symmetric extensions of the standard model this Higgs triplet is already introduced.

Since there are even more possible solutions to motivate neutrino mass, it is crucial to accomplish an absolute neutrino mass measurement. Approaches to measure the mass originate from various fields of physics, with the next chapter giving insights on these methods.

1.3 Absolute ν-mass determination

Different methods to obtain the absolute mass scale of neutrinos have been established. Each of these methods provides certain advantages and disadvantages, concerning the observables and sensitivity to the neutrino mass. In this section, different approaches will be discussed, closing with pure kinematic methods, as used by the KATRIN experiment.

1.3.1 Cosmology

Structure formation in the universe is directly affected by the non-vanishing neutrino mass. Neutrinos smeared out structures in the scale of their free streaming length, which is connected to the sum of the three neutrino masses $\sum_i m_i$. With the cool down and the expansion of the early universe, the thermal equilibrium of neutrinos, electrons, positrons and photons broke and neutrinos decoupled around 1 s after the Big Bang. The decoupling caused small density fluctuations, that evolved into large scale structures as seen today. Furthermore, are the neutrino properties imprinted in the photons of the *Cosmic Microwave Background* (CMB). Hence the anisotropy in the temperature spectrum of the CMB allows conclusions to the neutrino mass.

In order to investigate the neutrino mass within the framework of cosmological models, various experiments, installed on satellites, have been carried out. These probes, like WMAP and Planck, scanned the CMB with high precision or mapped todays structures of the universe in large sky surveys [PD$^+$15] [BM14] [A$^+$14]. From a combined analysis [OG14] different upper mass limits for the sum of neutrino masses have been estimated:

$$\sum m_\nu < 0.23\,\mathrm{eV} \quad \text{Planck + WMAP} \tag{1.9}$$

$$\sum m_\nu < 0.12\,\mathrm{eV} \quad \text{SDS-III + Planck} \tag{1.10}$$

These limits strongly rely on the sophisticated and rather complex cosmological models [LP06] used to analyze the experimental data.

1.3.2 Neutrinoless double beta decay

Another opportunity to investigate the neutrino masses arises from neutrinoless double beta decay, abbreviated by $0\nu\beta\beta$. This decay needs neutrinos of Majorana-type, otherwise this decay is not possible. The case, where two neutrinos (anti-neutrinos) and electrons (positrons), $2\nu\beta\beta$, are emitted simultaneously from the same nucleus occurs, when the binding energy of the daughter nucleus is larger then the mother isotope, while the intermediate isotope has a lower binding energy. With Majorana-type neutrinos, $\nu = \bar{\nu}$, the neutrino of the one β-decay is directly absorbed by the other, hence no neutrinos are emitted. As a result, the complete kinetic energy is stored in the electrons, which results in a sharp peak at the end of the decay spectrum. The corresponding decay rate Γ of the $0\nu\beta\beta$-decay scales with the squared effective Majorana mass $m_{\beta\beta}$, as long as no further process in the standard model dominates the decay:

$$\Gamma \propto \left| \sum_i U_{ei}^2 m_i \right|^2 \equiv m_{\beta\beta}^2 \,. \tag{1.11}$$

This mass term represents the coherent sum of the three neutrino mass eigenstates, but holds the possibility, that contributions are cancelled partially, due to the phase factors of the PNMS matrix. Furthermore the decay rate depends on the model-based precalculated nuclear matrix element. This matrix element is subject to large systematic uncertainties within the calculations.

The experiments GERDA, KamLAND-Zen and EXO-200 investigate double beta decay-spectra to find the $0\nu\beta\beta$ signature, aiming to establish if neutrinos are Majorana particles and for neutrino mass determination. As the $0\nu\beta\beta$-decay has not been observed, upper mass limits given by the isotope used and the underlying nuclear matrix element can be extracted. For germanium, using enriched ^{76}Ge as source and detector material in GERDA, the calculated mass limit is:

$$|m_{\beta\beta}(^{76}\text{Ge})| \leq 0.25\,\text{eV - }0.52\,\text{eV}\,, \tag{1.12}$$

whereas a combined analysis of KamLAND-Zen and EXO-200 for ^{136}Xe [DGMR13] results in:

$$|m_{\beta\beta}(^{136}\text{Xe})| \leq 0.11\,\text{eV - }0.25\,\text{eV}\,. \tag{1.13}$$

In 2006 the Heidelberg-Moscow collaboration claimed an observation of the $0\nu\beta\beta$-decay, which has been published. Their analysis revealed a mass of 0.3 eV [KKK06] for a germanium based detector, but this has been excluded by the new experiments [MAC14].

1.3.3 Supernovae explosions

The cosmic event of a supernovae allows an estimation of neutrino mass by time of flight. Here the relative flight time of photons and neutrinos originating from a collapsing star and reaching the earth is compared. The time difference between both particles arises due to the mass of the neutrino and is therefore less model dependent as previous methods. Nevertheless the exact start time is not obtainable, which again needs a model of the processes within the dying star. In contrast to the neutrinoless double beta-decay, supernovae studies aim for an average mass of the electron neutrino, which does not exhibit the possible cancellation of mass eigenstates. This leads to a formulation of the observable given by:

$$m_{\nu_e} = \sqrt{\sum_i |U_{ei}|^2 m_i^2}\,. \tag{1.14}$$

The Kamiokande experiment and IMB were able to detect 24 neutrino events originating from the supernovae SN 1987A. This cataclysmic explosion occurred in the Large Magellan Cloud at a distance of ca. $168 \cdot 10^3\,\mathrm{ly}$. It is assumed, that all neutrinos were created at the same time, left the supernovae in a single event and the neutrinos traveled more or less unaffected by the matter between supernovae and earth. All events occurred in a time interval t_{arrival} of ~13 s, had an energy between 10 MeV and 40 MeV and emitted during a time t_{emission}. Due to the mass, the neutrinos travel below speed of light, which allows to write their time of flight (t_{tof}) by means of mass m_{ν_e}, kinetic energy E_ν and distance L:

$$t_{\text{tof}} = t_{\text{arrival}} - t_{\text{emission}} = \frac{L}{v} = \frac{L}{c}\frac{E_\nu}{p_\nu c} = \frac{L}{c}\frac{E_\nu}{\sqrt{E_\nu^2 - m_\nu^2 c^4}} \approx \frac{L}{c}\left(1 + \frac{m_\nu^2 c^4}{2E^2}\right)\,. \tag{1.15}$$

For neutrinos with different times of arrival $t_{\text{arrival,1}}$ and $t_{\text{arrival,2}}$ and energies E_1 and E_2, the time difference on earth can be described by:

$$\Delta t_{\text{arrival}} = t_{\text{arrival,2}} - t_{\text{arrival,1}} \tag{1.16}$$

$$= t_{\text{tof,2}} - t_{\text{tof,1}} + \Delta t_{\text{emission}} \tag{1.17}$$

$$= \frac{L}{2c} m_\nu^2 c^4 \left(\frac{1}{E_2^2} - \frac{1}{E_1^2}\right) + \Delta t_{\text{emission}}\,. \tag{1.18}$$

With given energies E_1 and E_2, flight distance L and arrival interval $\Delta t_{\text{arrival}}$ from the supernovae SN 1987A, a model dependent neutrino mass estimation is reasonable. The model dependency is introduced in the emission time interval $\Delta t_{\text{emission}}$. By [AR87] this estimation gives rise to an upper limit to the neutrino mass of:

$$m_{\nu_e} < 5.8\,\mathrm{eV}\,. \tag{1.19}$$

1.3.4 Kinematic measurements

From a kinematic point of view, the neutrino mass can be determined by a precise measurement of the β-decay spectrum. The electron energy herein ranges between zero and a maximal value given by $E_0 = Q - E_{\text{rec}} - m_{\nu_e}c^2$, which is defined by the total decay energy Q, the recoil energy of the nucleus E_{rec} and the ν-mass. In a β-decay an electron and a neutrino are created, thus the decay energy is distributed to both particles. Therefore, at the endpoint of the spectrum the maximal available energy is stored in the electron. With a non-vanishing neutrino mass, the endpoint position and shape is modified by the neutrino rest mass, see figure 1.2.

The general case of β-decay in a nucleus is described by:

$$(\mathrm{Z, A}) \to (\mathrm{Z+1, A}) + \mathrm{e}^- + \bar{\nu}_{\mathrm{e}}\,, \tag{1.20}$$

leaving a nucleus with an increased proton number and an emitted electron and anti-neutrino. The electrons kinetic energy spectrum can be calculated with Fermi's golden rule, giving a decay rate for the energy interval $[E{,}E+dE]$:

$$\frac{dN^2}{dt\,dE} = \frac{d\dot{N}}{dE} = \frac{2\pi}{\hbar}|M|^2\rho(E)\,. \tag{1.21}$$

Herein M represents the nuclear matrix element of the decay and $\rho(E)$ the phase-space density. Since the nucleus mass is significantly higher than

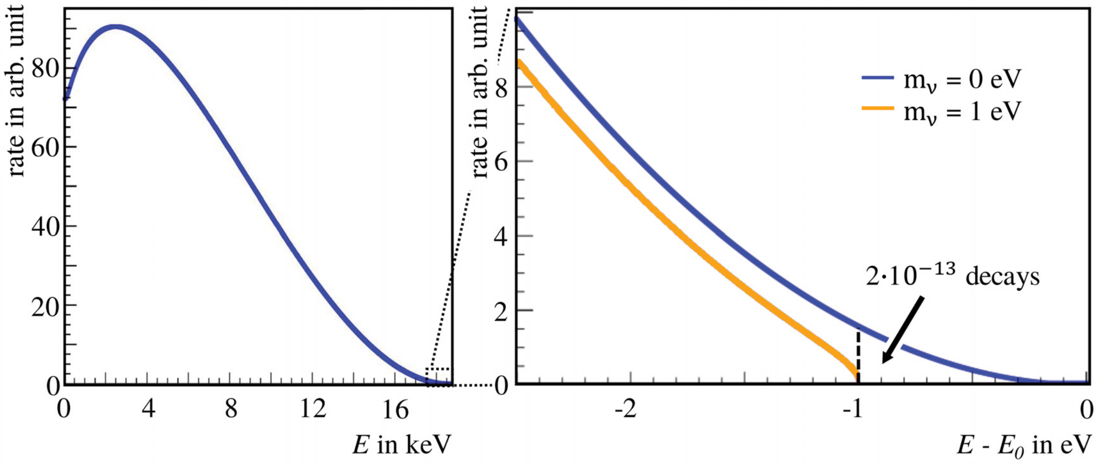

Figure 1.2: Differential spectrum of the tritium β-decay. Due to the non-vanishing neutrino mass the shape of the spectrum is modified close to the endpoint. Only a fraction of all emitted electrons have energies in this region making a source with high activity mandatory. Figure adapted from [Val09].

the electron or neutrino mass, their phase-space factors can be separated. Additionally the nuclear recoil energy can be neglected, leading to a density:

$$\begin{aligned}\rho(E) &= \frac{dn_\mathrm{e}}{dE_\mathrm{e}}\frac{dn_\nu}{dE_\nu} = \frac{p_\mathrm{e}E_\mathrm{e}p_\nu E_\nu}{4\pi^4\hbar^6}V^2 \\ &= \frac{V^2}{4\pi^4\hbar^6}p_\mathrm{e}(E+m_\mathrm{e}c^2)\sqrt{(E_0-E)^2-m_\nu^2c^4}(E_0-E)\,, \end{aligned} \tag{1.22}$$

given a normalization volume V and $E_\nu = E_0 - E$, with E_0 as energy of the spectrum endpoint and E the kinetic energy of the electron. The nuclear matrix element can be written by means of a hadronic and leptonic part:

$$|M| = G_F\cos(\theta_C)\cdot M_\mathrm{nuc}\cdot M_\mathrm{lep}\,, \tag{1.23}$$

with the Fermi coupling G_F and the Cabibbo angle $\theta_C = 13°$. For a super-allowed transition the leptonic part can be written by the Fermi function F and a normalization volume V:

$$|M_\mathrm{lep}|^2 = \frac{1}{V^2}F(E,Z+1) \tag{1.24}$$

All these formulas at hand, the β-spectrum can be derived [WA03]:

$$\begin{aligned}\frac{dN^2}{dEdt} &= A\cdot F(E,Z+1)\cdot p_\mathrm{e}(E+m_\mathrm{e}c^2)(E_0-E) \\ &\quad\cdot\sqrt{(E_0-E)^2-m_\nu^2c^4}\cdot\Theta((E_0-E)-m_\nu c^2)\,, \end{aligned} \tag{1.25}$$

including a pre-factor:

$$A = \frac{G_F^2\cos^2(\theta_C)}{2\pi^3\hbar^7}|M_\mathrm{nuc}|^2\,. \tag{1.26}$$

To give a complete picture, corrections for e.g. final states distributions, finite mass of the nucleus etc., have to be implemented, which are discussed in detail in [DHMW08].

The neutrino mass in equation 1.25 is introduced by the neutrino momentum:

$$p_\nu = \sqrt{(E_0-E)^2-m_\nu^2c^4}\,, \tag{1.27}$$

which is most significantly influenced by m_ν near the endpoint E_0 of the β-decay spectrum. Sources with a low endpoint energy improve the sensitivity, since a greater fraction of electrons are located there. Furthermore this circumstance allows for a generally better energy resolution in an experiment.

In nature ^{187}Rh is the β-emitter with the lowest endpoint energy of $E_0 = 2.5\,\mathrm{keV}$, making this isotope a candidate for neutrino mass measurements. However, rhenium has a complicated electronic structure and a half-life of the order of 10^{10} y since the decay proceeds via a forbidden transition. The MARE project planned to use rhenium in a set-up where the isotope is source and detector material at the same time.

Since the neutrino mass is still unknown, the most sensitive upper limit to this value from kinematic measurements is obtained from tritium β-spectra. Molecular tritium has the second lowest known endpoint energy of $E_0 = (18\,571.8 \pm 1.2)\,\mathrm{eV}$ and due to its rather short half-life, $T_{1/2} = 12.6\,\mathrm{y}$, and simple electronic structure, tritium represents a good candidate as source material [OW08]. Experiments using tritium are usually subdivided into a source section, providing a high decay rate and a spectrometer section with a high energy resolution. For this purpose a MAC-E filter type spectrometer is advantageous, because these grant a large angular acceptance and the needed energy resolution.

Two experiments were developed following such a set-up, which currently provide the best upper limits on the neutrino mass; the Mainz and Troitsk neutrino mass experiments. They provide the following limits:

$$m(\nu_\mathrm{e}) < 2.3\,\mathrm{eV} \qquad \text{Mainz [KBB}^{+}\text{04]} \tag{1.28}$$

$$m(\nu_\mathrm{e}) < 2.05\,\mathrm{eV} \qquad \text{Troitsk [ABB}^{+}\text{11]}\,. \tag{1.29}$$

The successor of these kinematic measurements, which use tritium as β-emitter, is the KATRIN experiment. KATRIN aims to measure the neutrino mass with a sensitivity of $0.2\,\mathrm{eV/c^2}$ at 90 % C.L., providing an improvement of one order of magnitude over previous experiments. In the next chapter, design and set-up of the experiment will be explained in detail.

Neutrino mass cannot only obtained from β-emitters, but also by electron capture processes, e.g. in ^{163}Ho. Here holmium captures an electron, altering the nucleus to an exited dysprosium $^{163}\mathrm{Dy}_i^*$ nucleus and releasing an electron-neutrino. The following de-excitation leads to an energy spectrum with several energy lines E_i:

$$^{163}\mathrm{Ho}^+ + \mathrm{e}^- \rightarrow {}^{163}\mathrm{Dy}_i^* + \nu_\mathrm{e} \rightarrow {}^{163}\mathrm{Dy} + E_i + \nu_\mathrm{e}\,. \tag{1.30}$$

The neutrino mass is again imprinted into the spectral shape, which is measured by special bolometers in the ECHo project [BDD$^+$13] [GBD$^+$13].

1.4 Thesis outline

Chapter 2 presents an overview of the KATRIN experimental set-up and its major components. The focus of this chapter is on the MAC-E filter principle, as one of the key techniques of the experiment and on an introduction of the following investigations. Furthermore the effect of systematic and statistical uncertainties of the experiment on the neutrino mass sensitivity will be discussed. In that context background processes occurring in the main spectrometer, affecting the neutrino mass measurements, are introduced.

Chapter 3 will discuss possibilities for background reduction with the main spectrometers inner wire electrode system, which was affected by short circuits during baking of the spectrometer. This chapter summarizes the repair action, which partially restored the double layer functionality of the electrode. Measurements with effective potentials and temperature gradients, that allowed an investigation of the background reduction with double wire layers, are presented.

Chapter 4 introduces a method to investigate the spectrometer background characteristics by adjusting the magnetic field and electric potential in order to shift the analyzing plane to either flat cone region of the main spectrometer. The chapter also discusses spectroscopic measurements with the shifted analyzing plane, that lead to an energy reconstruction of the volume dependent background. Finally the feasibility of a tritium β-measurement mode with the shifted analyzing plane is presented and studied with a monoenergetic and angular selective electron source.

Chapter 5 changes the topic and focuses on the set-up and commissioning of a quench Condensed Krypton Source (CKrS), which uses $^{83\mathrm{m}}$Kr gas condensed on a cooled HOPG substrate as source material. After discussing the available conversion electron lines and the ellipsometry system used to characterize thin films, a detailed overview of the CKrS set-up and all crucial components will be given. This chapter summarizes the commissioning and characterization of the CKrS prior to and within the krypton measurement campaign in 2017 and discusses the performance of the complete set-up.

Chapter 6 summarizes the main results of this thesis and presents an outlook to ongoing and future measurements.

Chapter 2

The KATRIN experiment

The **Ka**rlsruhe **Tr**itium **N**eutrino mass experiment, KATRIN, is designed to perform a measurement of the tritium β-spectrum with highest precision, reaching for a neutrino mass sensitivity of 0.2 eV/c^2 at 90 % C.L.. The KATRIN experiment is situated at the Karlsruhe Institute of Technnology, KIT, because of the already excellent infrastructure for tritium handling within the Tritium Laboratory Karlsruhe, TLK. Due to the outstanding anticipated sensitivity all involved technologies are pushed to the technical feasible limit.

The following sections provide an overview of the experiment in its entirety as well of the major components necessary to perform the measurements.

2.1 Experimental set-up

The KATRIN experiment is set up with a source, where the tritium β-decay takes place, a separate spectrometer for electron energy filtering and a detector to count the filtered decay electrons. KATRIN has dimensions of 70 m in overall length and 10 m diameter at the spectrometer. In figure 2.1 the complete assembly of KATRIN is shown. The source is a windowless gaseous tritium source (WGTS), which provides a high rate of β-electrons and is connected to a transport section, where the electrons are guided magnetically towards the spectrometer. Within the transport section two different pumping concepts, differential and cryogenic pumping, reduce the amount of tritium flow towards the spectrometer section and ensure that no contamination appears. The following two spectrometers, pre- and main spectrometer, allow high precision energy filtering of the decay electrons, which then can be detected at a segmented Si-PIN detector, called focal plane detector (FPD).

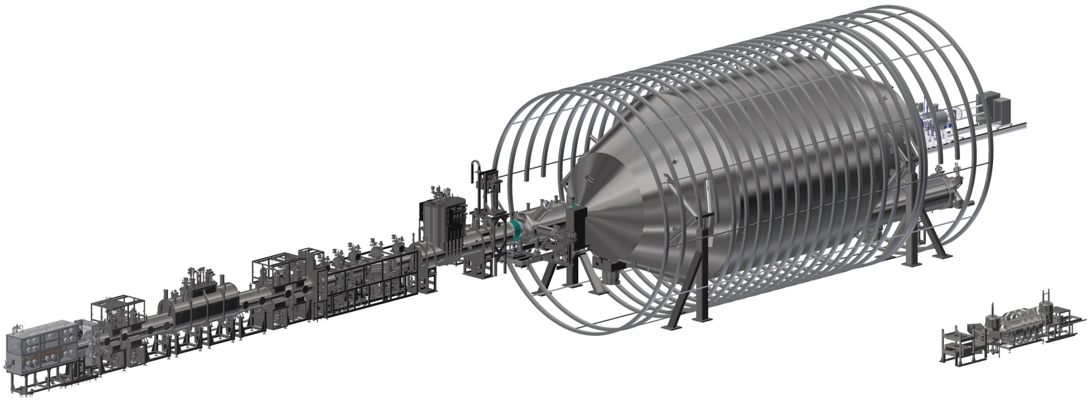

Figure 2.1: Complete assembly of the KATRIN beamline. The KATRIN experiment consists of three key components. The source and transport section, consisting of the high rate windowless gaseous tritium source followed by a beamline for transport of electrons and pumping for tritium retention. Subsequently the spectrometer section with pre- and main spectrometer for electron energy filtering and the detector section with a segmented detector for counting high energy electrons that passed the spectrometer.

2.1.1 Rear Section

The rear section (figure 2.2) represents the very first part of the KATRIN experiment, since this section closes the rear end of the WGTS. The rear section contains monitoring systems to observe parameters like the source activity. Furthermore the plasma potential of the gaseous tritium within the source can be controlled with the rear section, because the magnetic flux tube connects the plasma with the gold-plated rear wall. This wall separates the tritium source and the rear section and can be illuminated to emit electrons via the photoelectric effect to prevent a charging up of the tritium gas. Within the rear section an electron source is housed, which is used to determine transmission properties of the complete beamline. The well-defined electron beam allows to probe the inelastic scattering cross-sections in the tritium source [A$^+$05] [Bab14] [HHW$^+$17].

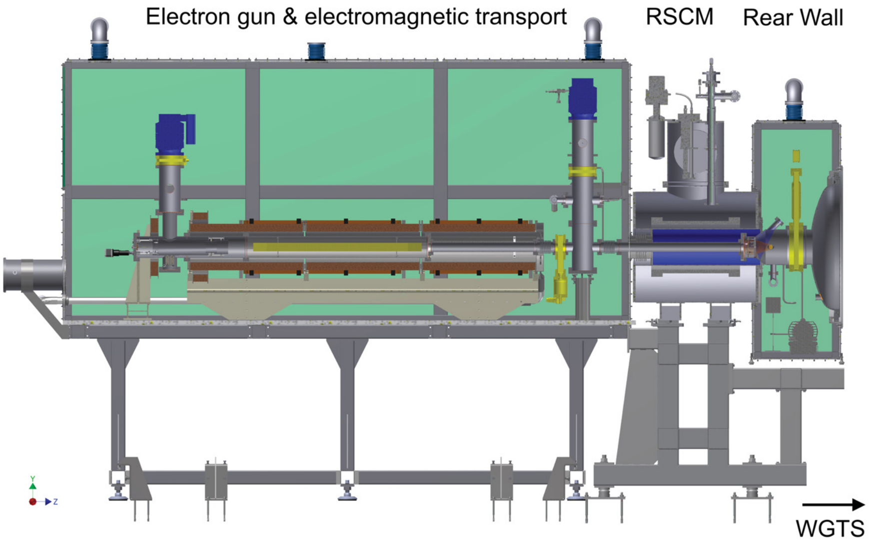

Figure 2.2: Technical drawing of the rear section. The left-hand side of the image shows the second containment for the electron source (e-gun) including the electromagnetic transport elements for the electrons. On the right side is the rear wall chamber closing the WGTS volume towards the rear section [Bab14].

2.1.2 Source and transport section

The source and transport section comprises the **windowless gaseous tritium source** (WGTS) as well as the **differential pumping section** (DPS) and **cryogenic pumping section** (CPS).

The **windowless gaseous tritium source**, depicted in figure 2.3, provides the source material, molecular tritium, for the KATRIN experiment. Due to the yearly throughput of 10 kg of tritium the source generates enough rate to reach the statistical sensitivity needed. The tritium itself is contained in a closed loop system, that reclaims the gas for reprocessing. To achieve an activity of 10^{11} Bq the column density inside the WGTS is $\rho d = 5 \cdot 10^{17}$ molecules / cm^2, which is accomplished by an inlet pressure $p_{\text{in}} = 3.4 \cdot 10^{-3}$ mbar and a temperature $T = 30$ K. During the operation the column density has to be known with a precision of 0.1 % [A$^+$05]. The WGTS cryostat houses the 10 m long and 90 mm wide beam tube, in which the tritium is injected. By a two-phase neon cooling system the temperature inside the tube can be adjusted with 30 mK stability. For the electron transport, the beam tube is surrounded by superconducting magnets with a strength of 3.6 T. The tritium injection occurs in the center of the beam tube and at the ends the gas is pumped back into the closed loop system by two differential pumping sections, DPS1-R and F,

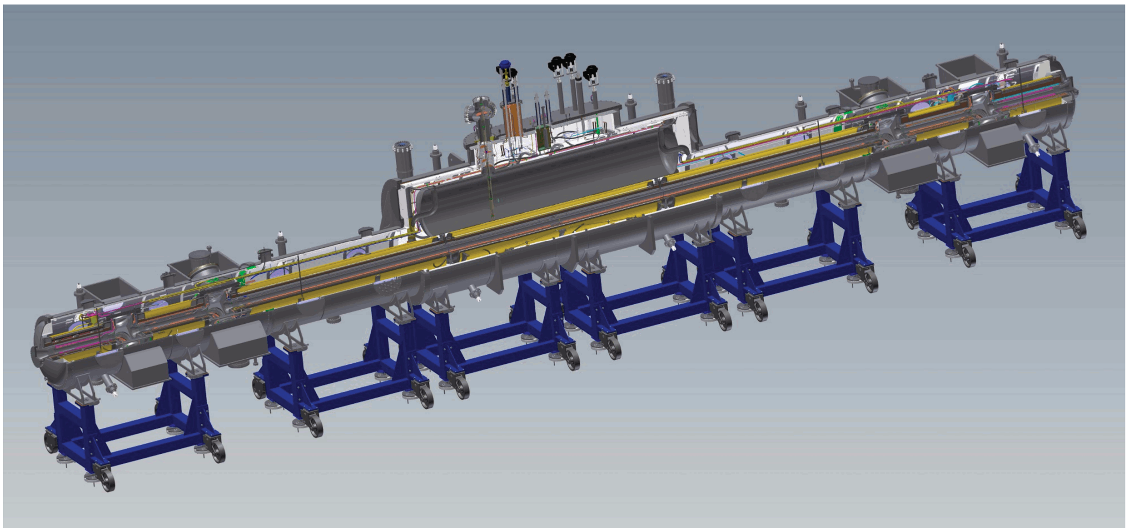

Figure 2.3: CAD drawing of windowless gaseous tritium source (WGTS). The cross section shows the cryostat with the 10 m long beam tube, surrounded by superconducting magnets. At both ends are differential pumping sections, DPS1-R/F, which decrease the tritium flow towards the rear section, respectively the transport and spectrometer section. The tritium is injected at the center of the cryostat creating a symmetric density profile towards the ends of the WGTS.

figure 2.4 (a). To keep systematic uncertainties below the required levels, the working parameters of the WGTS need to be known to the 10^{-3} level. These parameter are for example tritium gas temperature, injection pressure or tritium purity. The gas purity is monitored by the so-called LARA-system, which is a Laser-Raman spectrometer integrated into the closed loop system (figure 2.4 (b)) [Bab14]. Here the composition of the inlet gas, which consists to $> 95\,\%$ of molecular tritium, is measured with a sensitivity of $0.1\,\%$ [Fis14].

The required temperature stability at $T = 30\,\mathrm{K}$ of $30\,\mathrm{mKh}^{-1}$ is ensured by the neon-cooling system shown in figure 2.5. Pt500 and vapor pressure sensors along the beam tube observe the temperature during the operation [Bab14].

Since the WGTS is is not closed, tritium gas could propagate towards the spectrometer and produce background events. To avoid this, the flow has to be reduced by 14 orders of magnitude. Hence the KATRIN experiment has, additionally to DPS1-R/F, a differential pumping section and cryogenic pumping section implemented between the source and spectrometer section.

The **differential pumping section**, called DPS2-F, follows the WGTS towards the spectrometer and is displayed in figure 2.6. The DPS is subdivided into five beam tubes with a length of 1 m each, set up an angle of 20° between every beam tube. This way the beamline shapes a chicane, prohibiting a direct

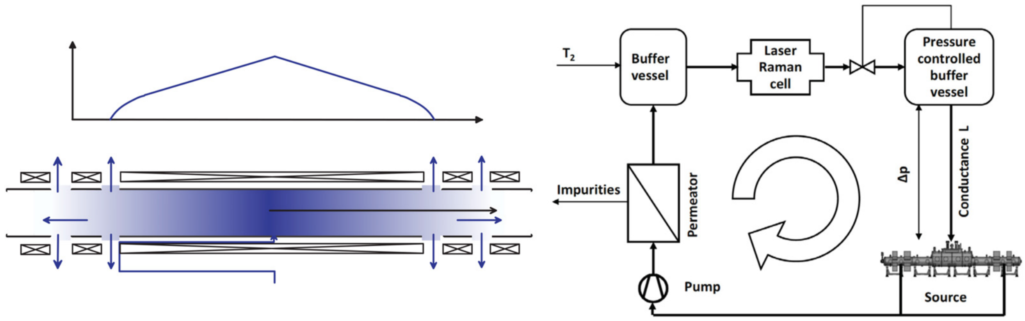

(a) (b)

Figure 2.4: Overview of beam pipe set-up and loop system of WGTS. The tritium gas is injected into the beam tube at the center and pumped out again at the ends, which creates a symmetric density profile inside the WGTS as shown in (a) [A$^+$05]. After pumping, the gas re-enters a closed loop system for re-processing and control by Laser-Raman spectroscopy (b).

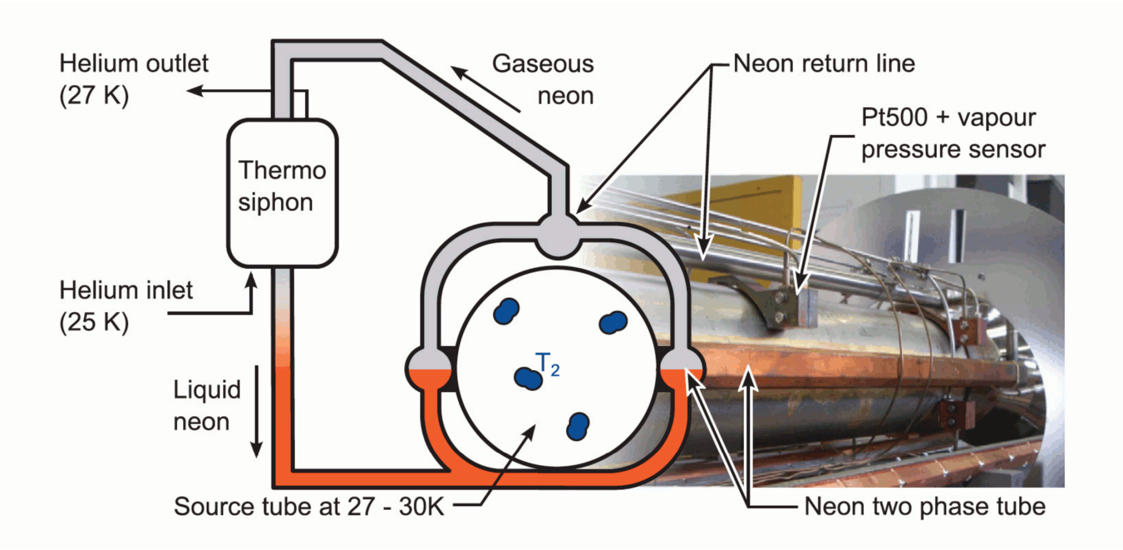

Figure 2.5: Temperature control of the beam tube by two-phase neon. The neon is cooled by heat exchange in a thermo siphon in a helium bath. Monitoring of the temperature is perfomed with Pt500 and vapor pressure sensors [Bab14].

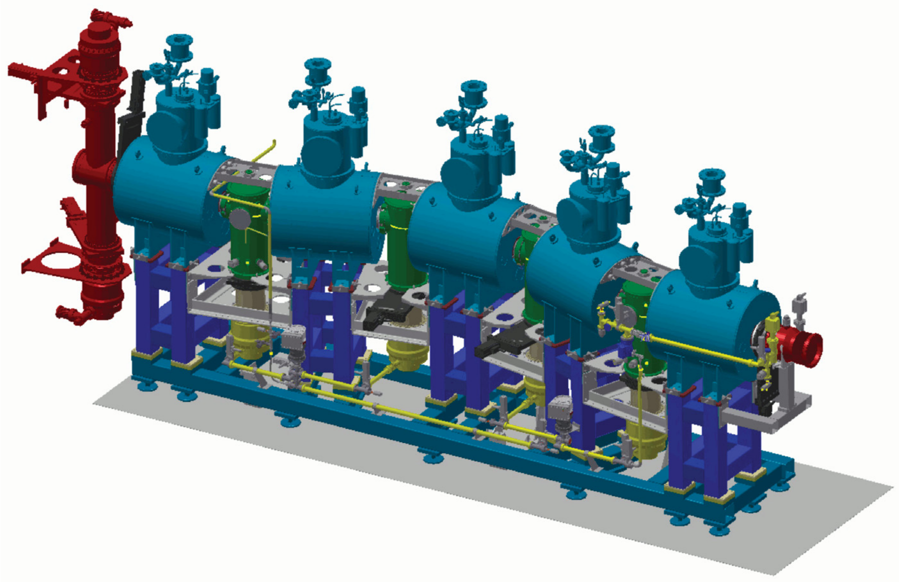

Figure 2.6: Assembly of the differential pumping section (DPS2-F). The segmented design of the DPS2-F is shaped as a chicane to prevent a direct line of sight between source and spectrometer. Electrons from the source are guided by five superconducting magnets along the beamline, whereas neutral tritium gas molecules hit the walls. The last segment houses ring-shaped and dipole electrodes to drift charged ions out of the beamline. With turbo-molecular pumps at the interconnections of each segment, the gas flow reduced by a factor 10^5. Figure from [Jan15].

line of sight from WGTS to spectrometer. Every segment is surrounded by a superconducting magnet with a field strength up to 5.5 T, which guides the decay electrons through the chicane. Neutral particles, e.g. remaining tritium molecules move straight into the bends of the beamline and are removed by turbomolecular pumps.

The last segment of the DPS2-F is equipped with ring shaped blocking electrodes, which prevent ions from entering the spectrometer by a positive blocking potential. Additionally dipole electrodes are installed in the DPS2-F, that deflect ions towards the walls by introducing $\vec{E} \times \vec{B}$ drift fields [Rei09] [Hac15].

At the interconnection joints of the beam tubes, turbo-molecular pumps, type TURBOVAC MAGW 2800, with a suction capacity of $2400\,\mathrm{l\,s^{-1}}$ are installed. With these, a retention of tritium in the order of 10^5 is achieved, which adds up to 10^7 when combining with the DPS1-F. The final pressure inside the beamline needs to reach $6 \cdot 10^{-10}$ mbar, since the ultra high vacuum conditions of the spectrometer have to be matched [LDH$^+$06] [LBB$^+$12] [Kos12].

Placed directly in front of the spectrometer is the **cryogenic pumping section** (CPS). The CPS is intended to reduce the tritium amount by an additional seven orders of magnitude, leading to a total retention factor of 10^{14} for the complete transport section. To this end the beam pipe again follows a shape with several bends and is cooled down to 3 K. The inner surface is covered with an argon frost layer which increases the overall surface drastically. The argon frost layer acts as a very effective cryo pump, achieving a 10^{7} reduction of neutral gas atoms. The pre-condensed frost will be renewed bi-monthly to remove the accumulated activity.

From a technical point of view, the CPS is segmented into seven sections surrounded by superconducting magnets, depicted in figure 2.7. The first five segments shape a chicane like the DPS2-F and are separated by the last two beam tubes via the cold gate valve V3. Per definition the tritium area ends after this valve, which will be closed during argon replacement or in case of safety issues [GBB^{+}10].

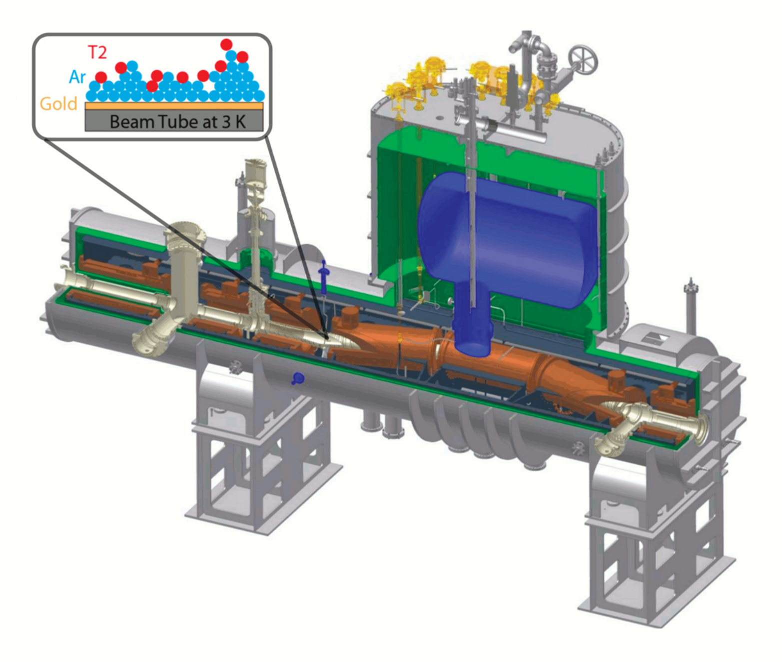

Figure 2.7: Schematic drawing of the cryogenic pumping section (CPS). The CPS follows a similar chicane set-up like the DPS2-F to prevent a direct line of sight along the beamline. To enhance the retention factor by seven orders of magnitude the beam tube of the CPS is cooled to 3 K and covered with an argon frost layer. This cold surface acts as a cold trap for tritium gas passing through. At port P2 the forward beam monitor and condensed krypton source can enter the beamline for activity and calibration measurements. Schematic drawing adapted from [Wan13]

Between the sixth and seventh beam tube segment, two ports are placed (P2), allowing a horizontal and vertical entrance to the beamline. Horizontally the **forward beam monitor** (FBM) can be introduced, a detector to scan the activity of the source during tritium operations. From above the **condensed krypton source** (CKrS) will be lowered into the beam tube to fulfill calibration and transmission function measurements with a condensed $^{83\mathrm{m}}$Kr film. A detailed description of this source will be given in chapter 5.

2.1.3 Spectrometer section

Following the transport section is the tandem of **pre-spectrometer** (PS) and **main spectrometer** (MS). These are based on the MAC-E filter principle and are dedicated to perform a precise energy analysis of the tritium β-decay electrons. In figure 2.8 the smaller PS, left side, and the prominent MS, right side, of the KATRIN experiment are displayed. Both spectrometers are designed to filter the electron energy by applying a retarding to potential U_{ret}, which can only be overcome by electrons with energies $E_{\mathrm{e}} > qU_{\mathrm{ret}}$. Varying the retarding potential allows to record an integral spectrum at the detector (see section 2.1.4) [Zac14] [Val09] [P^{+}92b].

The **pre-spectrometer** is a vacuum vessel with a length of 3.4 m and diameter of 1.7 m. At the entrance and exit superconducting magnets are positioned,

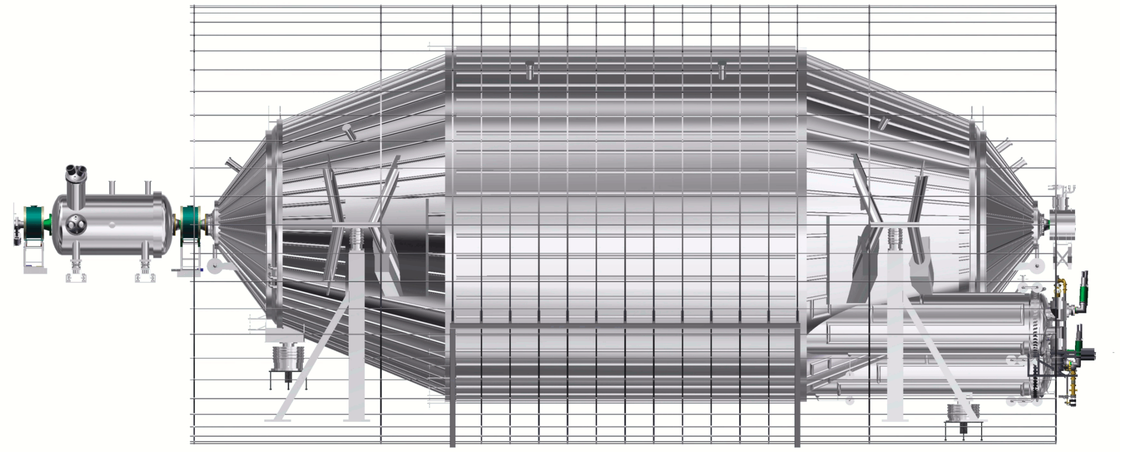

Figure 2.8: Tandem of pre- and main spectrometer. The purpose of the spectrometers are the energy filtering of electrons originating from the tritium β-decay. The pre-spectrometer, set to a potential of −18.3 kV blocks the bulk of the electrons, since they do not carry information of the neutrino mass. By varying the retarding potential of the main spectrometer around the endpoint region, ∼−18.6 kV, an integral spectrum can be obtained.

able to generate a 4.5 T magnetic field. The pre-spectrometer operates at a potential of −18.3 kV to reject the low energy part of the electron spectrum, which provides no information to the neutrino mass. Furthermore the reduction of the electron flux lowers the scattering probability with residual gas and thus improves the background in the main spectrometer.

Following this, the **main spectrometer** extends over 23.3 m in length and a diameter of 10 m. The size of the spectrometer was determined by the electromagnetic design, allowing the required adiabatic transport and precise energy analysis. Both spectrometers operate at ultra high vacuum conditions below 10^{-11} mbar to reduce scattering processes, which would increase the background. To reach this exceptional pressure in a vessel with a volume of $1240\,\mathrm{m}^3$, the MS has three pump ports fitted with a combination of TMP's and non-evaporable getter stripes (NEG). The TMP's provide a total pumping speed of 10^4 l/s and the NEG pump up to 10^6 l/s for hydrogen [ABB$^+$16] [Har15].

For the energy filtering, the vessel is set to an electric potential near −18.6 kV. A fine shaping of the electric potential in the analyzing plane, where the electron energy filtering is performed, is introduced by the inner wire electrode (section 3.1). Furthermore, the wire electrode is used for background reduction by generating a blocking potential for charged particles originating from the vessel walls [Pra11] [Val09] [Zac09]. To reach the outstanding precision, which is mandatory for the experiment, two ultra precise high voltage dividers have been developed for KATRIN [Bau13] [Thü07]. These are directly connected to the spectrometer HV power supplies and scale down the voltage by a factor 2000. This allows voltage measurements with commercial precision volt meters in the 10 V range. The HV divider is calibrated by a reference divider at the Physikalische Technische Bundesanstalt (PTB), which allows an absolute calibration. Additionally a low voltage calibration against a precision 10 V reference potential, traced back to a Josephson voltage standard, can be accomplished on-site. In [Res19] a newly developed absolute calibration method is described, that allows an absolute high voltage calibration on-site at KIT. Hence the calibration can be performed more frequently and the systematic uncertainties for the potential stability decrease.

A further approach to observe the retarding potential stability is the **monitor spectrometer** (MoS). This third spectrometer is the refurbished spectrometer of the Mainz Neutrino Mass Experiment and is now used as monitoring device. The MoS, depicted in figure 2.9, receives the same high voltage as the main spectrometer. The source material for the monitor spectrometer is $^{83\mathrm{m}}$Kr implanted in HOPG. The krypton provides monoenergetic conversion electrons, thus providing a natural energy standard. By taking an integral spectrum of these conversion electrons in a regular manner the line position can be analyzed for stability, which directly correlates to the stability of the retarding potential of the main spectrometer [EBB+14] [Sle15] [Erh16].

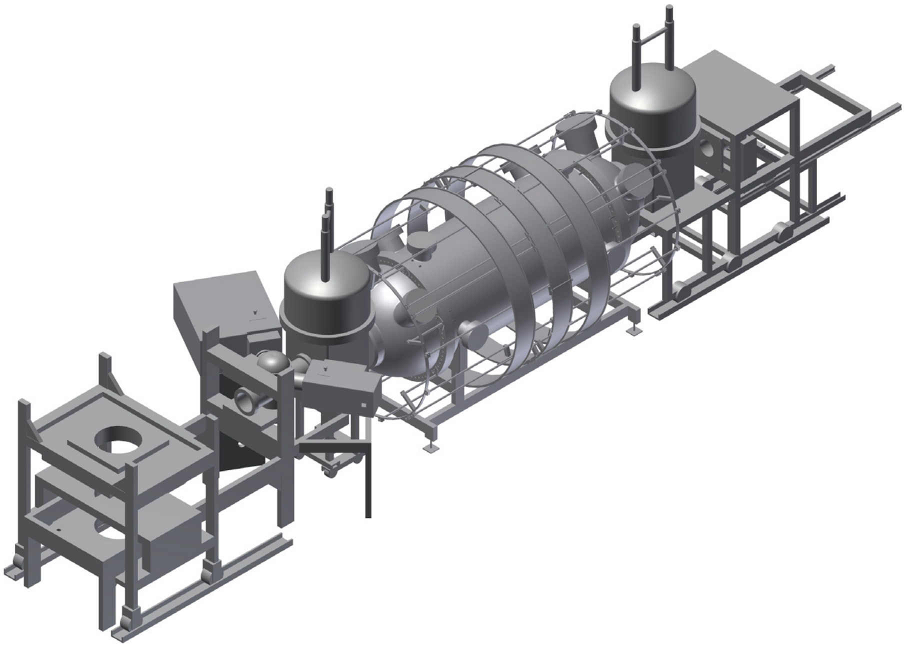

Figure 2.9: Depiction of the monitor spectrometer. The former spectrometer of the Mainz Neutrino Experiment is refurbished and used as calibration device for the KATRIN experiment. Integral measurements of $^{83\mathrm{m}}$Kr conversion electron lines, performed with the vessel potential shared by the main spectrometer and the monitor spectrometer, allow for precision stability analysis of the retarding potential.

2.1.4 Detector system

The last part of the KATRIN experiment is the **Focal Plane Detector** (FPD). Every electron with energy exceeding the retarding potential in the MS, hits the detector and is counted. Except from counting incoming electrons, their energy can be measured with a resolution of 1.4 keV FWHM. This is sufficient to perform energy depended cuts for background and electric noise rejection. The detector itself is a silicon wafer, Si-PIN diode, which is segmented into 148 area normalized pixels with a dead layer of 100 nm. The wafer is connected to read-out electronics positioned inside a separate high vacuum chamber (10^{-6} mbar). To reduce intrinsic electronic noise, the system is cooled to −30 °C. Since the complete set-up operates on HV potential, the communication between detector and data acquisition (DAQ) is linked through optical fiber [Har15]. All counting events, recognized by the DAQ system are

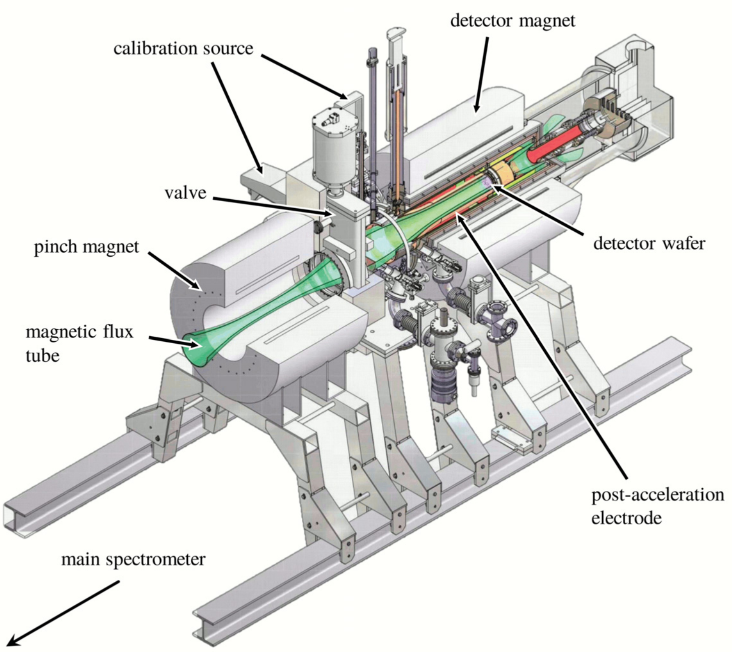

Figure 2.10: Cross section of the detector system. Electrons from the tritium β-decay are magnetically guided onto the focal plane detector (FPD). The segmented Si-PIN wafer of the FPD allows a spatially resolved detection of the electrons, thus making a correction for field and potential inhomogeneities possible. The post acceleration electrode enhances the signal-to-noise ratio and enables access to low energetic electrons. Figure from [Hac17].

processed and distributed by the ORCA software package. ORCA reviews all incoming data, sorts and stores the data stream for later offline analysis. Furthermore ORCA provides an interface to all parameters to operate the FPD. In figure 2.10 a cross section of the detector displays the general set-up.

In front of the detector, a post acceleration electrode (PAE) is positioned. This electrode can be used to accelerate electrons with an additional potential of up to 10 kV, which improves the signal-to-noise ratio of the system. Furthermore electrons with energies below 5 keV become detectable by the FPD, since they gain enough energy through the acceleration [Har15].

The segmentation of the detector wafer allows a position determination for each counted electron. Thus by simulation, the electron trajectories can be reconstructed to a certain level. The main reason for a multi pixel detector is to compensate for spatial inhomogeneities in the magnetic field or the electric potential. With detailed position information, an energy normalization for every pixel can be implemented, which results in a decrease in systematic uncertainties.

2.2 MAC-E filter

The precision electron energy filtering takes place in the main spectrometer of the KATRIN experiment. The filter method is based on magnetic adiabatic collimation with electrostatic filtering, with the abbreviation MAC-E filter. First published in 1981 [BPT81], the technique was later used in various experiments [LS85] [P+92a]. To analyze the tritium β-decay electrons, the electrons with energies exceeding the filter potential are counted. Then by varying the potential, an integral spectrum can be obtained, which inherits the neutrino mass information. The KATRIN main spectrometer MAC-E filter is designed to have an energy resolution of 0.93 eV and an acceptance angle of 51° in the forward direction. In the next subsection the properties of MAC-E filters will be discussed.

2.2.1 Adiabatic collimation

The MAC-E filter of the main spectrometer has two major components. At the entrance and exit of the main spectrometer two superconducting solenoids are placed, which provide the magnetic field. The electrons entering the spectrometer from the source side are guided along the magnetic field lines to the detector side exit. Along their flight the electrons experience a decrease in the magnetic field strength of several orders of magnitude. The solenoids generate magnetic fields up to $B_{\text{max}} = 6\,\text{T}$ in their center, while the field at the central plane of the spectrometer drops to a minimum of $B_{\text{min}} \approx 0.3\,\text{mT}$. The other component of the MAC-E filter is the retardation of the electrons by an electrostatic filter. The filtering potential is introduced by applying a voltage $U_{\text{ret}} \approx -18.6\,\text{keV}$ to the spectrometer vessel and the inner wire electrode. At the central plane the magnetic field minimum and electric potential maximum overlap, defining the so-called analyzing plane. The schematic overview of the KATRIN MAC-E filter in figure 2.11 displays key components of the filter technique.

The electrons entering the spectrometer are guided magnetically along the field lines. Depending on their pitch angle $\theta = \measuredangle(\vec{p},\vec{B})$, which is defined as the angle between the electron momentum $\vec{p}$ and the local magnetic field direction $\vec{B}$ at the starting point of the electron, the electron has a certain amount of transverse energy. This energy component leads to a gyration of the electron around the magnetic field line. Therefore the total kinetic energy E_{kin} of the

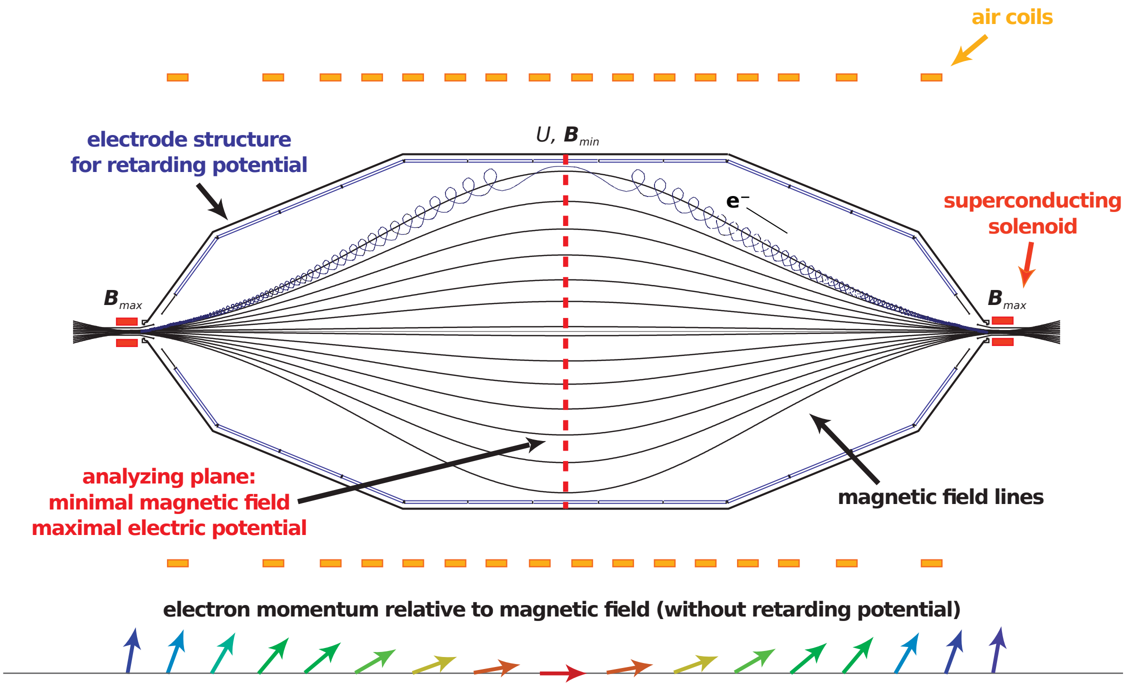

Figure 2.11: MAC-E filter technique. The magnetic guiding field is introduced by two superconducting solenoids at the entrance and exit of the spectrometer. Electrons entering the spectrometer follow the magnetic field lines and propagate with cyclotron motion. Fine shaping of the magnetic field is achieved by an air coil system, surrounding the spectrometer. The retarding potential is generated by applying high voltage to the vessel and the inner electrode system inside. To surpass the analyzing plane, given by the overlap of minimal magnetic field and maximal electric potential, electrons need to have a longitudinal energy component above the retarding energy. Since the transport is adiabatic the transversal electron energy component is transformed into the longitudinal component as the electrons move towards the lower magnetic field of the analyzing plane. The maximum amount of the transversal energy component remaining in the analyzing plane determines the energy resolution of the spectrometer. This figure is adapted from [Val09].

electron is composed of a longitudinal $E_{\|}$ and a transversal $E_{\perp}$ component:

$$E_{\|} = E_{\mathrm{kin}} \left(\frac{\vec{B} \cdot \vec{p}}{|\vec{B}||\vec{p}|} \right)^2 = E_{\mathrm{kin}} \cdot \cos^2(\theta) \tag{2.1}$$

$$E_{\perp} = E_{\mathrm{kin}} - E_{\|} = E_{\mathrm{kin}} \cdot \sin^2(\theta)\,. \tag{2.2}$$

The cyclotron motion of the electron causes an orbital magnetic moment μ. In the non-relativistic approximation this is given by:

$$\mu = |\vec{\mu}| = \frac{q}{2m_{\mathrm{e}}}|\vec{l}| = \frac{E_{\perp}}{B}\,, \tag{2.3}$$

with an angular momentum $\vec{l}$.

As an electron passes through the spectrometer it experiences a magnetic field gradient. This gradient leads to a force $\vec{F}_{\nabla}$, that causes an acceleration of the electron parallel to the magnetic field line, in the direction of the magnetic field minimum. In the non-relativistic case, this can be written as:

$$\vec{F}_{\nabla} = \nabla(\vec{\mu} \cdot \vec{B})\,. \tag{2.4}$$

If the transport of the electron happens adiabatically, the total kinetic energy of the electron is conserved. Thus the increase of the longitudinal energy leads to an according decrease in the transversal component.

The electrostatic potential applied to the spectrometer is not only needed for the energy analysis of the electrons, but also ensures the adiabaticity of the energy transformation. The deceleration of the electrons, beginning at the spectrometer entrance, reduces the relative change of the magnetic field strength along one cyclotron revolution to a sufficiently low level. In the adiabatic limit, expressed by:

$$\frac{1}{B}\frac{d\vec{B}}{dt} \ll \omega_{\mathrm{cycl}} = \frac{qB}{\gamma m_{\mathrm{e}}}\,, \tag{2.5}$$

the product of the relativistic Lorentz factor γ and the absolute value of the magnetic moment $|\vec{\mu}|$ are conserved in the motion.

Electrons originating from tritium β-decays have a maximal γ-factor of 1.04, which allows a non-relativistic approximation. Thus the orbital magnetic moment is a conserved quantity, leading to the formulation:

$$\mu = \frac{E_{\perp}}{B} = \text{const.}\,. \tag{2.6}$$

With this equations at hand, one can derive the transformation of the transversal energy component by:

$$\frac{E_\perp}{B} = \frac{E'_\perp}{B'} \tag{2.7}$$

$$\Rightarrow \sin^2(\theta') = \sin^2(\theta) \cdot \frac{B'}{B} \,. \tag{2.8}$$

Hence the pitch angle, and therefore the transversal energy component, is solely defined by the ratio between different magnetic fields.

A MAC-E filter utilizes this effect, because it leads to a collimation of the electron momentum. Electrons entering the spectrometer with large pitch angles transform their transversal momentum to longitudinal momentum due to energy conservation. At the analyzing plane, the pitch angle is at its minimum and the longitudinal momentum component has a maximum.

2.2.2 Energy resolution

The MAC-E filter acts as a high-pass filter for electrons with a threshold defined by the retarding potential. Due to the adiabatic collimation, an acceptance angle of 2π is theoretically allowed. With the consideration of subsection 2.2.1 an energy resolution for an MAC-E filter can be derived and calculated for the KATRIN spectrometer.

In a realistic MAC-E filter the magnetic field strength along the field lines decreases to a finite minimum, which exceeds 0. Therefore the transversal electron energy cannot be transformed completely. Due to this, electrons with pitch angles near 90° require larger kinetic energies to surpass the filter. Under the assumption that all kinetic energy is stored transversally at the spectrometers entrance, $E_\text{kin} = E_\perp^\text{start}$ and the pitch angle is maximal, $\theta = 90°$, the longitudinal energy fraction at the magnetic field minimum is computed. This fraction corresponds to the energy spread between electrons with minimal and maximal pitch angle, which determines the spectrometer resolution ΔE:

$$\Delta E = E_\perp^\text{max} - E_\perp^\text{min} = E_\perp^\text{start} \cdot \frac{B_\text{min}}{B_\text{max}} = E_\text{kin} \cdot \frac{B_\text{min}}{B_\text{max}} \,. \tag{2.9}$$

Herein B_min and B_max denote the magnetic field extrema inside the spectrometer. Furthermore $E_\perp^\text{min} = 0\,\text{eV}$ describes the transversal energy for electrons with a vanishing pitch angle.

With nominal operation settings the magnetic field has a maximal field strength of $B_\text{max} = 6\,\text{T}$ at the pinch magnet, which decreases to $B_\text{min} = 0.3\,\text{mT}$. At the tritium β-spectrum endpoint, electrons carry kinetic energies near $E_0 \approx 18.6\,\text{keV}$. This results in a $\Delta E = 0.93\,\text{meV}$ resolution of the KATRIN main spectrometer.

2.2.3 Electron transmission

The transmission properties discussed in this section are based on an isotropically emitting electron source, which is the case for the WGTS. During the characterization of the spectrometer properties an angular selective electron source with defined energies, called e-gun, has been used [Beh16]. In the course of this thesis, see section 5, a condensed krypton source (CKrS) has been implemented into the KATRIN experiment. This CKrS allows transmission measurements and pixel-wise calibration of the retarding potential with isotropically emitted electrons from a frozen $^{83\mathrm{m}}$Kr film, which provides conversion electrons with well-defined energies in various monoenergetic lines.

Electrons transmitted through the MAC-E filter fulfill the basic equation:

$$E_{\|}(E_{\text{start}},\theta_{\text{start}},\vec{r}) + qU > 0\,, \tag{2.10}$$

where qU represents the retarding energy defined by the retarding potential. E_{start} and θ_{start} describe the initial state of the electron, namely starting energy and pitch angle. As derived in section 2.2.1 the initial pitch angle of the electron is transformed approaching the analyzing plane. Hence the transmission conditions at the analyzing plane can be written as:

$$E_{\|}^{\text{ana}} - qU_{\text{ana}} = E_{\text{start}} - E_{\perp}^{\text{ana}} - qU_{\text{ana}} = E_{\text{start}} - E_{\text{start}} \sin^2(\theta_{\text{start}}) \cdot \frac{B_{\text{ana}}}{B_{\text{start}}} > 0\,. \tag{2.11}$$

If the maximal magnetic field B_{max}, encountered by the electrons on their way to the detector, is larger than the starting field B_{start}, electrons with a starting angle θ_{start} exceeding a certain cut-off angle θ_{max} are magnetically reflected. This θ_{max} is given by:

$$\theta_{\text{max}} = \arcsin\sqrt{\frac{B_{\text{start}}}{B_{\text{ana}}}}\,. \tag{2.12}$$

All starting angles up to θ_{max} form a cone with a fixed solid angle $\Delta\Omega$ in which electrons can be transmitted through the spectrometer.

From the above considerations a transmission function for electrons can be derived. It depends on the kinetic energy of the electron E_{start}, the properties of the analyzing plane (U_{ana}, B_{ana}), the source magnetic field B_{source} and the maximal field B_{max}:

$$\begin{aligned} &T(E_{\text{start}},U_{\text{ana}}) = \\ &= \begin{cases} 0 & E_{\text{start}} < qU_{\text{ana}} \\ 1 - \sqrt{1 - \frac{(E_{\text{start}} - qU_{\text{ana}})}{E_{\text{start}}} \cdot \frac{B_{\text{source}}}{B_{\text{ana}}}} & qU_{\text{ana}} \leq E_{\text{start}} \leq qU_{\text{ana}} + \Delta E \\ 1 - \sqrt{1 - \frac{B_{\text{source}}}{B_{\text{max}}}} & E_{\text{start}} > qU_{\text{ana}} \frac{B_{\text{max}}}{B_{\text{max}} - B_{\text{ana}}} \end{cases} \end{aligned} \tag{2.13}$$

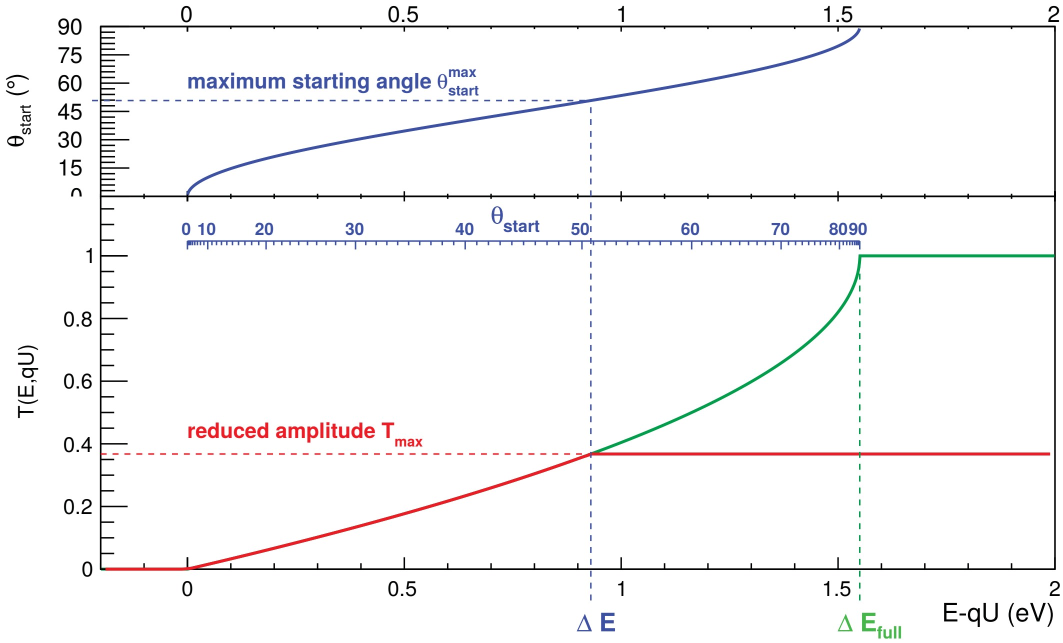

Figure 2.12: Simulated transmission properties of the KATRIN MAC-E filter. The upper illustration shows the electron starting angle θ_{start} for electrons near the spectrum endpoint that corresponds to a given surplus energy. The lower part of the plot shows the transmission probability $T(E_{\text{start}}, U_{\text{ana}})$ denoted in equation 2.13 [Zac14].

In figure 2.12 an analytically calculated transmission function for the nominal main spectrometer settings is displayed. There the resolution of the spectrometer is plotted against the starting pitch angle of an electron. The shown transmission probability T is reduced because of magnetic mirroring at the pinch magnet at the exit of the spectrometer, which is due to the asymmetric magnetic field strength of the superconducting magnets at entrance and exit.

2.2.4 Realistic MAC-E filter

In the previous section the theoretical aspects of the MAC-E filter technique and the corresponding advantages have been laid out. This subsection focuses on the actual constrains of said filter, which have to be accounted for. Since the spectrometer energy resolution is given by the magnetic field ratio between the two extrema, B_{min} and B_{max}, the size of the used spectrometer depends on this. Furthermore the transmission of electrons is affected by inhomogeneities in the electromagnetic fields, which can not be avoided in a realistic set-up.

The size of the spectrometer is depending on the conserved magnetic flux:

$$\Phi = \int_0^{r_{\max}} 2\pi r \vec{B}(r) d\vec{r} \approx B \cdot A = \text{const.}\,, \tag{2.14}$$

Since the magnetic field decreases towards the analyzing plane, the area enlarges to conserve the flux. At the minimal magnetic field, the flux tube of 191 T cm^2 [A$^+$05] has a corresponding radius of 5 m.

The retarding potential is generated by applying high voltage to the spectrometer and the inner electrode. Nevertheless, the potential is modified by the ground potential at the entrance and exit electrodes of the spectrometer, which cannot be shielded. The effective potential therefore becomes less negative towards the central beam axis because there the influence of the ground potential is most prominent. Due to this potential penetration, the analyzing potential is spatially deformed. The transmission properties and studies, regarding the field deformations, are described in [Beh16] [Erh16].

The spatial inhomogeneities of magnetic field and electric potential lead to modifications in the transmission function of the spectrometer. Therefore the focal plane detector is segmented into 148 pixel to address this effect. For each single pixel the variations in the transmission function for its related volume element of the spectrometer are less severe. With a pixel-wise calibration the design goal in terms of energy resolution is achievable.

2.3 Neutrino mass sensitivity

The measured electron rates depend on the retarding potential U_{ana} and the magnetic field, which determine the transmission function $T(E,qU)$ of the MAC-E filter. Uncertainties in the electromagnetic fields have a direct impact on the electron rate at the detector and therefore increase the systematic uncertainties of the measurement. Another source of uncertainties is given by the tritium gas pressure in the WGTS. Fluctuations in the column density translate to rate fluctuations at the detector. A further source of systematic uncertainties are energy losses due to inelastic scattering inside the WGTS. In [BBB$^+$12] it is stated, that 40 % of the emitted electrons leave the WGTS without interaction, whereas the remaining electrons scatter at least once during their propagation. The response function $R(E,qU)$ takes such processes into account. This function is a convolution of the MAC-E filter transmission function and a model of the energy loss [HHW$^+$17] [A$^+$05].

Based on this preconditions the electron rate, measured at the detector, $\dot{N}_{\text{signal}}$ is obtainable. Herein E_0 represents the energy at the tritium endpoint, m_{ν_e} the mass of the neutrino and N_{tot} the total number of tritium nuclei in the source:

$$\dot{N}_{\text{signal}}(qU,E_0,m_{\nu_{\text{e}}}) = N_{\text{tot}} \cdot \int_0^{E_0} \frac{d\dot{N}_\beta}{dE}(E,E_0,m^2_{\nu_{\text{e}}}) \cdot R(E,qU)dE\,. \tag{2.15}$$

Background electrons with low energies, originating form the volume inside the spectrometer, can reach the detector and alter the observed rate. Thus the electron signal from the tritium β-decay is overlapped, which can be expressed by:

$$\dot{N}_{\text{detected}}(qU,E_0,m_{\nu_{\text{e}}},\dot{N}_{\text{signal}},\dot{N}_{\text{back}}) = \dot{N}_{\text{signal}}(qU,E_0,m_{\nu_{\text{e}}}) + \dot{N}_{\text{back}}\,, \tag{2.16}$$

with $\dot{N}_{\text{signal}}$ corresponding to the β-decay signal (1.23) and $\dot{N}_{\text{back}}$ covering additional background electrons. This theoretical model is fitted to the measured β-spectrum to obtain the neutrino mass information. The fit has four free parameters: the neutrino mass $m_{\nu_{\text{e}}}$, the endpoint energy E_0, the signal amplitude N_{tot} and the background level $\dot{N}_{\text{back}}$. The sensitivity for the neutrino mass is highest in the region of the endpoint (figure 2.13). Yet part of the measurement time is needed to gather information about the background level at energies above the endpoint E_0. In [Kle14] comprehensive studies regarding an optimized measurement time distribution have been performed.

2.3.1 Systematics

The theoretical estimates of the ν-mass sensitivity are affected by several systematic and statistical uncertainties within the KATRIN experiment. As stated in section 2.2.4 the shape of the **transmission function** is modified by various parameters, which can cause deviations from the theoretical predictions. Inhomogeneities in the retarding potential and the minimal magnetic field at the analyzing plane cause spatial variations in the transmission function. Another systematic uncertainty is given by **fluctuations** in the high voltage and magnetic field generation, which arise from the power supplies, superconducting magnets and air coils. To reach the desired sensitivity of KATRIN, the uncertainty budget for each of the major systematic uncertainties needs to stay below 0.0075 eV^2. For the high voltage this corresponds to a maximum of 61 mV variation at the vessel voltage of −18.6 kV [A$^+$05]. The **column density** in the tritium source introduces further systematics. The decay rate of tritium is determined by the column density and the scattering probability is linked likewise. Therefore, an optimization is needed to find a density with a maximal decay rate, to gain sufficient signal events, and a minimal scattering, to reduce energy losses. In order to monitor the column

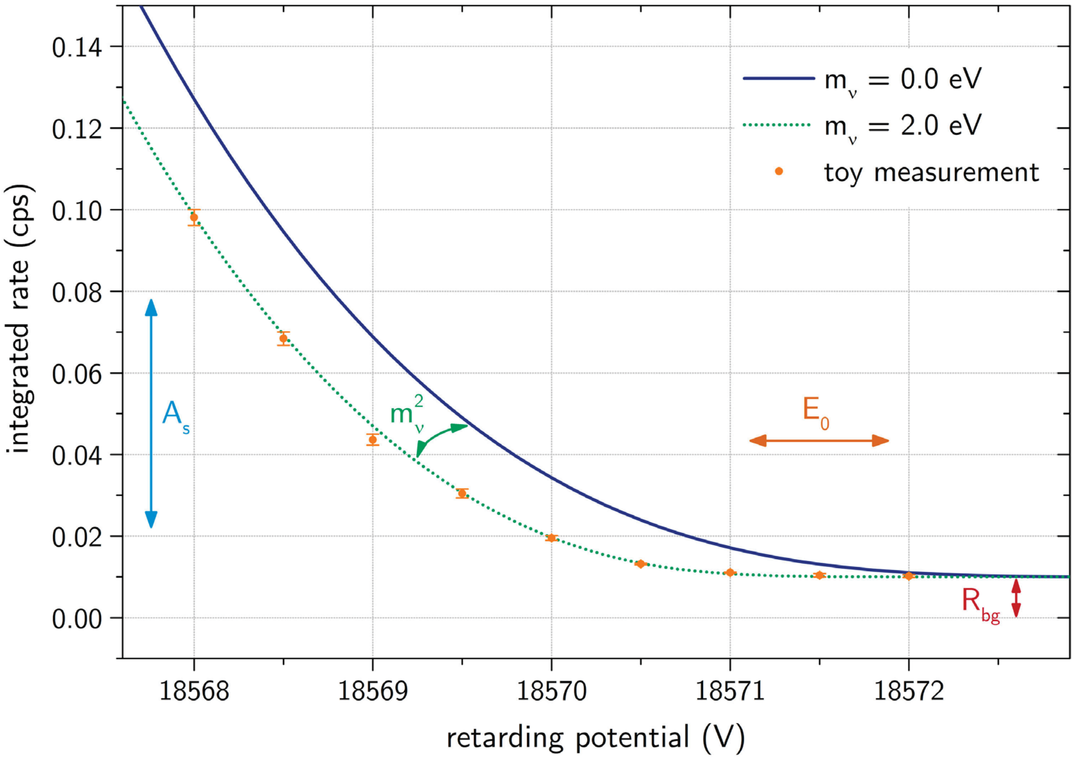

Figure 2.13: Simulation of integrated tritium β-spectrum for the KATRIN experiment. The blue line represents the theoretical spectrum for a vanishing neutrino mass $m_\nu = 0\,\mathrm{eV}$. The plotted green curve assumes a mass $m_\nu = 2$ eV. A simulated measurement regarding a neutrino mass of $m_\nu = 2$ eV is shown by orange points, which considers Poisson statistics for signal and background rates. Taken from [Kle14].

density, regular measurements with the rear section electron source [Bab14] are planned. Additionally a system observes x-rays at the rear-wall of the source by means of Beta Induced X-Ray Spectroscopy (BIXS) and the so-called Forward Beam Monitor measures the “halo” at the flux tube surrounding, which originate from the β-decay. The composition of the inlet gas is examined by means of Laser-Raman spectroscopy (LARA), since it affects the final states distribution [BBB$^+$12] [Fis14]. Furthermore a precise knowledge of the electron energy losses inside the WGTS is crucial for the response function. For this, the **energy loss function** needs to be determined with the rear section electron source [HHW$^+$17]. The **distribution of final states** of the tritium β-decay introduces additional systematic uncertainties. With an energy of 24 eV the first excited state of the daughter molecule (^{3}HeT)$^+$ becomes relevant for the endpoint region. The majority of decays, ∼57 %, leave the daughter molecule in the ground state. The sharpness of the spectrum endpoint is smeared out by rotational-vibrational excitations of the ground state, as well as further contributions by different molecules, like TH or TD, which need to be accounted for in an analysis [OW08] [A$^+$05] [Kle14]. In the various subparts and systems of the KATRIN experiment more sources of uncertainties are inherited. Nevertheless, the overall budget for systematic uncertainties is limited to $\sigma_{\text{tot,sys}} \leq 0.017\,\text{eV}^2$ to achieve the desired neutrino mass sensitivity.

2.3.2 Statistics

Near the endpoint of the tritium β-spectrum the statistical uncertainty of the KATRIN experiment is mainly determined by the background rate $\dot{N}_{\text{back}}$ and the signal rate. The rate for tritium β-decay electrons $\dot{N}_{\text{signal}}$, in a given energy interval ΔE, is affected by the filter energy $qU = E_0 - \Delta E$ of the MAC-E filter. An approximation for the total rate can be expressed by [OW08]:

$$\dot{N}_{\text{det}}(\Delta E) = \dot{N}_{\text{back}} + \dot{N}_{\text{signal}} \tag{2.17}$$

$$= \dot{N}_{\text{back}} + A \cdot \left(\Delta E^3 - \frac{3}{2} \Delta E \cdot \sum_i |U_{ei}|^2 m_i^2 \right) . \tag{2.18}$$

Herein A denotes the β-spectrum amplitude and the sum describes the average mass of the electron anti-neutrino, which is measured by the experiment, likewise to equation 1.3.3.

In measurements with a large energetic distance to the endpoint E_0, the cubed term is most significant. Otherwise the linear term, which is sensitive to the neutrino mass, affects the measured rate in the region near the endpoint. In direct vicinity to E_0 the background rate dominates the signal electrons. Far into in the spectrum the signal noise increases with $\sqrt{\Delta E^3}$ and therefore the neutrino mass signal is covered by noise. Hence an optimal measuring point ΔE_{opt} is formed for $\dot{N}_{\text{signal}}(\Delta E_{\text{opt}}) = 2\dot{N}_{\text{back}}$. Here the influence of the neutrino mass onto the measured spectrum reaches a maximum.

From this approximation the statistical uncertainty can be derived for a data point at a fixed retardation potential over the time t. When the neutrino mass is the only fit parameter considered, the uncertainty is given by [OW08]:

$$\delta m_{\nu_e}^2 \propto \dot{N}_{\text{signal}}^{-4/6} \cdot \dot{N}_{\text{back}}^{1/6} \cdot t^{1/2} . \tag{2.19}$$

Apparently a source with high activity is preferable for the experiment, since the uncertainties decrease more pronounced with the signal rate, then they increase by the background. Detailed calculations and investigations on the topic of uncertainties and measurement time distribution can be found in [Kle14].

The design goal for KATRIN aims for a total background rate of 10 mcps, which translates into a statistical uncertainty of $\sigma_{\text{tot,stat}} = 0.018\,\text{eV}^2$. Therefore the total uncertainty budget adds up to $\delta m^2_{\nu_e} = \sigma_{\text{tot}} = \sqrt{\sigma^2_{\text{tot,sys}} + \sigma^2_{\text{tot,stat}}} = 0.025\,\text{eV}^2$, corresponding to a neutrino mass sensitivity of $0.2\,\text{eV/c}^2$ at 90 % C.L. [A$^+$05]. Since the background rate was found higher then expected, the next section (2.4) focuses on background sources and processes that induce additional background signals.

2.4 Spectrometer background

As described previously, background events affect the neutrino mass measurement and need to be understood and minimized. In this section the most prominent background processes and mechanisms, which occur inside the KATRIN spectrometer, will be discussed.

Due to the electric potentials and magnetic fields needed for electron transport and filtering, the creation of **Penning traps** is possible. Penning traps are a localized phenomenon, emerging when specific electromagnetic field configurations result in particle storage. Low energetic electrons created in a potential U_0 can be trapped between cathodes with $U < U_0$ in axial direction. Radial movement is prevented by the Lorentz force, confining the electrons to magnetic field lines inside the MAC-E filter, see figure 2.14 (left-hand side). The stored electrons can ionize residual gas along their flight path, which results in generation of secondary electrons, positive ions and photons. This process can enhance creation of tertiary electrons causing an accumulation of charged particles inside the Penning trap. In severe cases the accumulation of low energy electrons lead to creation of an unstable plasma, which can break down. Such a Penning discharge can cause damages to the system and a careful design of the electromagnetic system is therefore required [Val09].

Another source of background is given by **magnetically stored particles**. Electrons created in the vicinity of the minimal magnetic field B_{min} inside the spectrometer can be reflected at high magnetic fields. This so called magnetic mirroring leads to a turn over of the electrons momentum vector and therefore change its trajectory. In case of the MAC-E filter, high magnetic fields are present at the entrance and exit, hence the electron is trapped by two mirrors, called magnetic bottle. The right side of figure 2.14 visualizes the electron movement in the magnetic bottle.

In consequence of the enormous size of the KATRIN main spectrometer vessel, the large inner surface area is a non-negligible source of background. **Elec-**

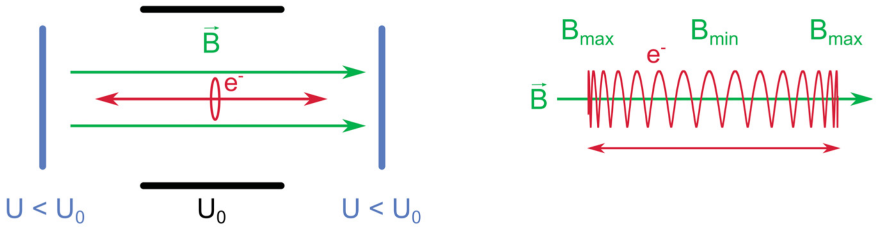

Figure 2.14: Particle trapping in MAC-E filter set up. **Left:** Electrons are stored electromagnetically in a Penning trap. **Right:** Due to specific magnetic field settings, the electron motion is kept inside a so-called magnetic bottle. [Gro10].

tron emission of the inner surface can originate from several processes. Cosmic rays and high energy γs from the environment radioactivity can penetrate the vessel hull at any time [Lei14] and create low energy secondary electrons. Additionally the decay of radioactive isotopes, which have been previously absorbed onto the surface or are implanted in the sub-surface layers emit electrons with various energies into the spectrometer volume. Furthermore low energy electrons can arise from field emission at surface areas with high electric field strength [For12]. Although the electromagnetic design and mechanical production of components has been performed with care, sharp edges can remain [SBB$^+$13]. These can cause high localized electric field strength, sufficient enough to emit electrons from the material via tunnel effect.

As a member of the primordial decay chains of ^{235}U, ^{238}U and ^{232}Th the **radon isotopes** ^{219}Rn, ^{220}Rn and ^{222}Rn present one of the largest contribution to low background experiments. In case of the KATRIN experiment radon can emanate from the surface area of the spectrometer vessel ($690\,\mathrm{m}^2$), inner electrode and support structures installed inside, as well as from the NEG material integrated in the pump ports to achieve the UHV conditions ($p \leq 10^{-10}$ mbar). High energy electrons created in radon decays are stored magnetically in the spectrometer and create low energy, secondary electrons. A detailed analysis to this topic is found in [Har15], presenting identification and countermeasures to the radon background.

Beforehand, cosmic radiation has been pointed out as a source of secondary electrons. With a flux of $\sim 10^5$ muons per second a significant impact to the overall background is expected [Lei14]. For that reason the **muon flux**, which penetrates the main spectrometer has been investigated. In a long term measurement with a dedicated muon detector system [Lin15] the data showed no significant correlation between background events and muon flux. This revealed the excellent magnetic shielding of the KATRIN spectrometer.

In the thesis of [Har15] various background measurements, concerning the processes pointed out beforehand, have been performed. Herein the background behavior at different conditions, i.e. vessel temperature, pressure and and magnetic field settings, are investigated. In conclusion to the thesis, a large fraction of the observed spectrometer background could not be explained by the analyzed mechanisms.

Further investigations revealed that a different background process creates electrons, which are distributed homogeneously over the complete spectrometer volume. Besides the event distribution, the background is reduced significantly by spectrometer bakeout, indicating a dependence on the surface conditions. Neutral, but excited unstable particles can propagate freely through the spectrometer and are not influenced by the presence of magnetic fields and electric potentials, which could explain the observed phenomena. These considerations give rise to a background production process by **de-excitation of hydrogen Rydbgerg states** [Dre15].

Rydberg atoms represent highly excited states near the ionization threshold with a radiative lifetime ~ms [Gal88]. This allows a free propagation through the spectrometer volume to create a uniform distribution. Hydrogen is highly abundant at the inner spectrometer surface and desorption from the stainless-steel generates H_2-molecules. Due to the distinct dipole moment of the transition between n-states, Rydberg atoms are sensitive to electromagnetic fields. Therefore, the Rydberg atoms can be ionized by blackbody radiation anywhere within the spectrometer volume and can create background events.

Since the commissioning measurements, which have been performed up to now, have shown an elevated background of a few 100 mcps, new methods for background reduction need to be discussed. The following chapters 3 and 4 aim to improve the background suppression with the inner electrode system in double layer mode and with altered potential settings, which shift the analyzing plane.

Chapter 3

Reduction of spectrometer background with double layer inner wire electrode

3.1 The inner wire electrode

Inside the KATRIN main spectrometer vessel an electrode system, consisting of thin wires on support frames, is installed. It covers the complete inner surface of the 23.3 m long and 10 m in diameter wide spectrometer, corresponding to 650 m^2. The inner wire electrode is designed to reduce background originating from cosmic muons and radioactive decays in the spectrometer vessel. Furthermore it is constructed to facilitate high precision field shaping, by allowing to apply 46 individual potentials to different parts of the electrode system.

In this chapter the working principle, the requirements and the technical design of the wire electrode will be presented. Problems that occurred with electrical short circuits during the first bakeout and the counter-measures taken, will be discussed.

3.1.1 Field shaping and background reduction

The retarding potential of a MAC-E filter, as used in [P$^+$92a], is generated by a system of HV electrodes, arranged cylindrically inside a spectrometer vessel, set to ground potential. In the case of the KATRIN main spectrometer the vessel itself is set to a potential of $U_{\text{vessel}} = -18.4\,\mathrm{kV}$. With an additional,

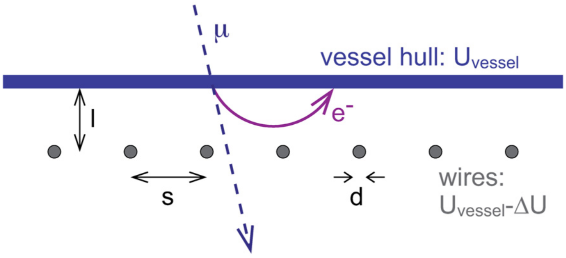

Figure 3.1: Sketch of secondary electron suppression by a wire electrode. The wires of diameter d have a neighboring distance of s and are positioned at a distance l from the vessel. Setting the wires to a potential more negative compared to the vessel will reflect electrons with energies below the potential difference.

variable potential of ca. −200 V on the inner wire electrode, the resulting electric potential in the main spectrometer can be scanned around the endpoint of the tritium β-spectrum. One purpose of the inner wire electrode is to reduce background induced by secondary electrons entering the magnetic flux tube. These electrons can originate from decays inside the vessel material, γ rays from active sources surrounding the experiment or muons generated by cosmic rays. According to [Arl09] the energy of muon induced secondaries entering the spectrometer is less then 100 eV and can therefore obtain cyclotron radii of $\mathcal{O}(0.1\,\mathrm{m})$. At the central part of the main spectrometer the inner radius is 4.9 m, whereas the radius of the magnetic flux tube, imaged on the detector, is 4.5 m. This leads to a magnetic shielding, that prohibits most background electrons from the vessel to reach the detector. Local field inhomogeneities or scattering reactions on rest gas molecules can still enable a certain fraction of electrons to reach the inner spectrometer volume.

To avoid that secondary electrons enter the flux tube a grid of wires is positioned inside the main spectrometer vessel and cover its inner surface. These wires are set to a more negative potential U_{wires} w. r. t. the vessel,

$$U_{\text{wires}} = U_{\text{vessel}} - \Delta U \quad (\Delta U > 0)\,. \tag{3.1}$$

A secondary electron originating from the vessel wall, which inherits a kinetic energy of $E_{\text{kin}} \leq q\Delta U$ can not propagate further into the spectrometer and is rebound to the hull, see figure 3.1. In order to reduce background from the wire electrode itself, it is constructed of thin wires, having a geometrical coverage as low as possible. The feasibility of this electrode design was shown at the former Mainz neutrino experiment [Fla04].

The effective potential U_{eff} inside the MAC-E filter is defined by the potentials of the vessel itself, the ground electrodes at each entrance and the wire electrode. Describing the inner vessel hull of the MAC-E filter as a surface

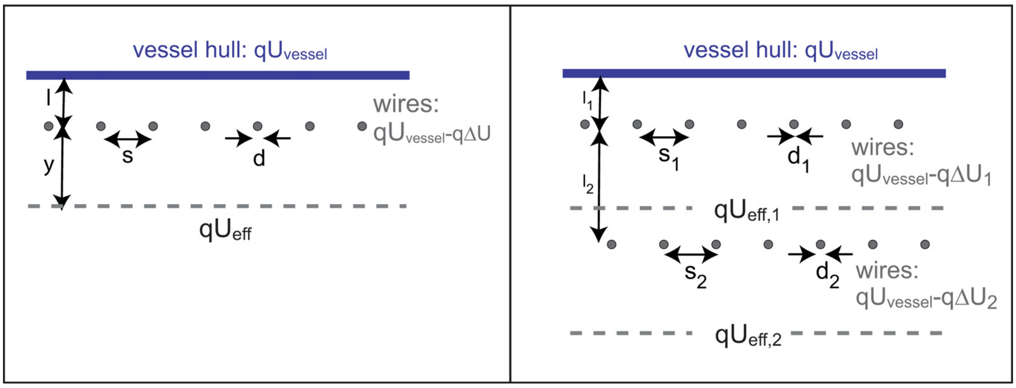

Figure 3.2: Schematic description of a single and double layer wire electrode. **Left:** Creation of an effective potential in the far field by a single wire layer. **Right:** Properties and effective potential introduced by a double wire layer.

with a single wire layer at a distance l and no influence of further electrodes, the effective potential can be expressed via the potentials of vessel U_{vessel} and wires U_{wire} and a screening factor S [Val09]. For a radial distance y larger than the distance between the neighboring wires s (see figure 3.2 on the left) the rippled structure of the retarding potential smears out, leaving a constant offset w. r. t. the vessel:

$$qU_{\text{eff}} = qU_{\text{wire}} + \delta qU \,, \tag{3.2}$$

$$\delta qU = \frac{qU_{\text{vessel}} - qU_{\text{wire}}}{S} \,. \tag{3.3}$$

This gives an effective potential of:

$$qU_{\text{eff}} = qU_{\text{wire}} \cdot \left(1 - \frac{1}{S}\right) + qU_{\text{vessel}} \cdot \frac{1}{S} \,, \tag{3.4}$$

with a screening factor [Glü]:

$$S = 1 + \frac{2\pi l}{s \ln(\frac{s}{\pi d})} \,. \tag{3.5}$$

To obtain the effective potential for an additional layer of wires (see right side of figure 3.2) the calculation can be done analogous to equation 3.4. Therefore, the effective potentials of the first and second layer can be written as:

$$qU_{\text{eff,1}} = qU_{\text{wire,1}} + \frac{qU_{\text{vessel}} - qU_{\text{wire,1}}}{S_1} \quad \text{and} \tag{3.6}$$

$$qU_{\text{eff,2}} = qU_{\text{wire,2}} + \frac{qU_{\text{eff,1}} - qU_{\text{wire,2}}}{S_2} \,. \tag{3.7}$$

Table 3.1: Wire configuration of the double layer electrode

layer	distance to vessel l / mm	wire diameter d / mm	spacing s / mm	screening factor S
1	150	0.3	25	12.5
2	70	0.2	25	5.8

Both formulas can be combined, so that the effective potential underneath the second wire layer is expressed by:

$$qU_{\text{eff,2}} = qU_{\text{wire,2}} + \frac{qU_{\text{wire,1}} - qU_{\text{wire,2}}}{S_2} + \frac{qU_{\text{vessel}} - qU_{\text{wire,1}}}{S_1 \cdot S_2} \,. \tag{3.8}$$

The additional wire layer is expected to further improve the shielding of background electrons and the homogeneity of the electric field in the inner spectrometer volume.

With the parameter set of the actual double layer wire electrode, given in table 3.1, and the anticipated $U_{\text{vessel}} = -18.4\,\mathrm{kV}$, $U_{\text{wire,1}} = -18.5\,\mathrm{kV}$ and $U_{\text{wire,2}} = -18.6\,\mathrm{kV}$ the generated effective potential amounts to $U_{\text{eff}} = -18\,581.38\,\mathrm{V}$.

For additional shaping capabilities, especially in the entrance and the exit regions of the spectrometer, where unwanted Penning traps can form more easily, the wire electrode system is segmented into rings that can be supplied with individual potentials. By introducing a system to distribute different voltages to designated areas inside the spectrometer the overall potential can be homogenized or arranged for investigations of spectrometer properties. These consideration lead to the construction of the double layer wire electrode for the KATRIN experiment. Within the theses of [Val09], [Zac09] and [Zac14] a deeper insight of field calculations and simulations are given. In the next chapter the technical realization of the electrode is presented, which is used later to explain the problems that arose during the spectrometer baking. Furthermore solutions to correct the presented problems will be proposed.

3.1.2 Construction of the wire electrode system

To gain a high flexibility in optimization of the potentials and to ensure the adiabatic transport of electrons, 46 independent voltages can be applied to the electrode system. Along the spectrometer axis the wire electrode is divided into ring like structures, where each ring is equipped with several modules, see figure 3.3. These modules have been manufactured outside the spectrometer vessel and are then guided to their designated position by a railing system [Pra11]. The complete wire electrode consist of 220 modules with double wire layers (ring 4 to 14) and 28 single layer modules (rings 2, 3, 15, 16). In table 3.2 a listing of all modules integrated into the main spectrometer is given.

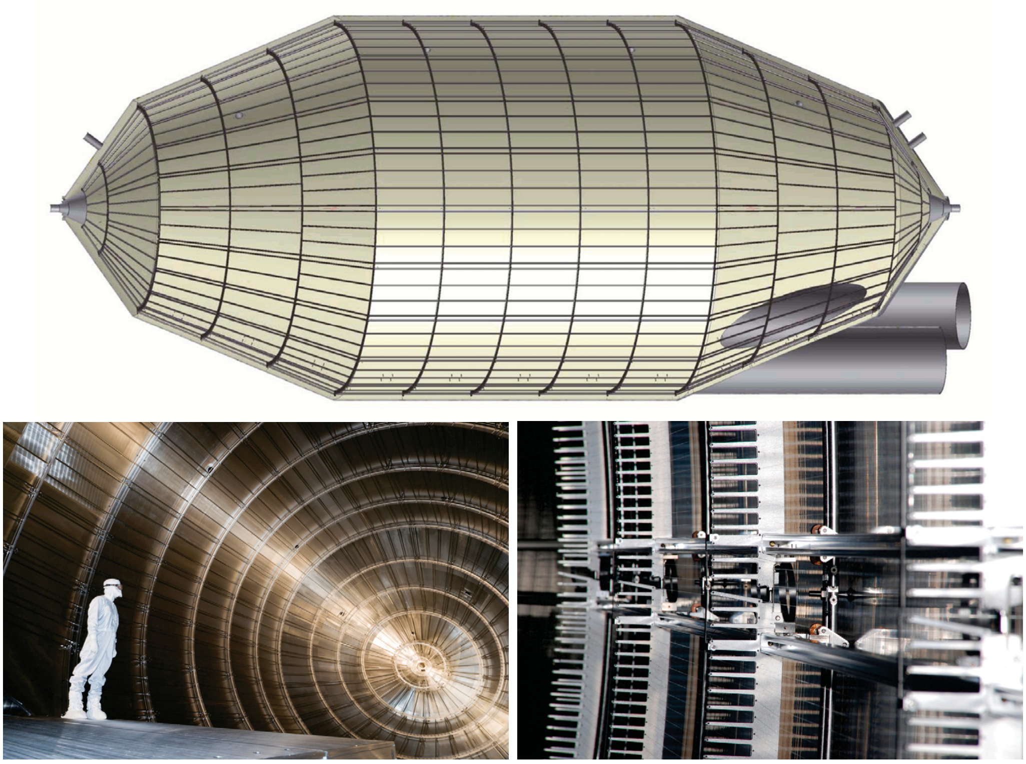

Figure 3.3: Inner electrode of the KATRIN main spectrometer. The upper CAD drawing shows the main spectrometer vessel with the internal electrode. It is structured in rings along the axis, which is due to the mechanical implementation of electrode modules. In the photographs below, a view inside the spectrometer is given. The lower left-hand picture shows parts of the electrode rings and on the right side the interconnection points between individual electrode modules can be seen.

Figure 3.4: Double layer wire electrode module before installation. The left picture shows the combs and c-profiles representing the support structure of an electrode module. In-between, the wire layers are stretched from comb to comb. The other picture denotes a detailed view of a module edge, equipped with the high voltage distribution connectors.

Table 3.2: Modular configuration of the inner wire electrode [Zac14]

ring	number of modules	number of layers	wires per module and layer	wire diameter (inner/outer)
07 - 11	20	2	60	0.2 mm / 0.3 mm
06 and 12	20	2	52	0.2 mm / 0.3 mm
05 and 13	20	2	42	0.2 mm / 0.3 mm
04 and 14	20	2	34	0.2 mm / 0.3 mm
03 and 15	10	1	40	0.2 mm
02 and 16	4	1	50	0.2 mm

The double layer wire modules consist of two comb like frames, which are separated through stainless steel c-profiles. The base of combs houses the wires for the outer layer of wires and at the tips the inner wire layer is installed. Profiles and combs are insulated against the wire layers by ceramics. All wires of a layer are interconnected since they carry the same potential and the outer wires are connected additionally to the support structure (see figure 3.4). For the single wire layer modules a similar design was chosen. Here again the wires are positioned at the tips of a comb and insulated against it, so they can be set to a certain potential. A second independent voltage can be applied to the frame.

The high voltage distribution consists of the modules themselves and of additional distribution lines connecting the module rings to the outside world.

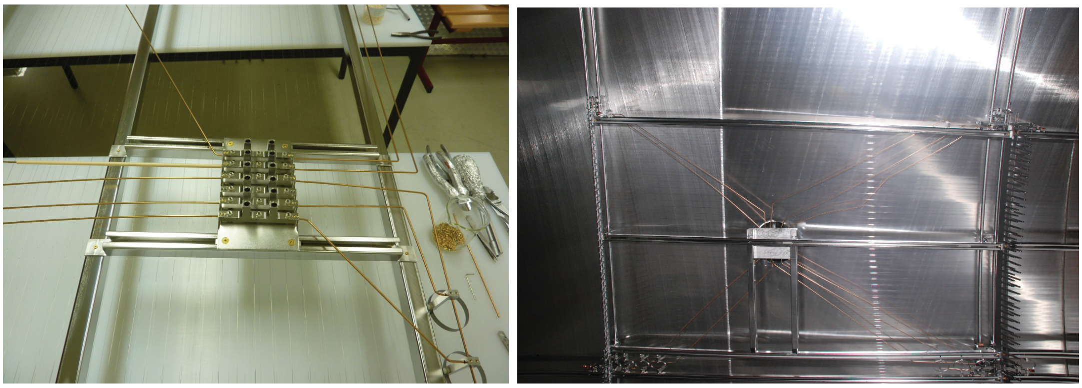

Figure 3.5: High voltage distribution modules. Underneath the vacuum ports on top of the main spectrometer the high voltage distribution for the inner wire electrode is realized. The stainless steel connectors in the module center obtain the voltage from feedthroughs and route it to copper beryllium rods, which establish connections to distant modules.

A system of different springs and spacers connects the neighboring modules within a ring and additional springs along the axis are linking different rings. Special modules beneath the vacuum ports on top of the spectrometer host high voltage connectors, which are coupled to feedthroughs at the ports. The high voltage distribution on top of the module is realized through stainless steel sockets, which extend to more distant modules via copper beryllium rods, see figure 3.5.

All implemented materials have to withstand high thermal and mechanical load, since the spectrometer is specified to be bakeable to 350 °C. This is necessary to remove contaminations, which are situated on the surfaces of the vessel hull to achieve better vacuum conditions. During the bakeout the spectrometer and its inner components elongate up to 20 cm along its axis. In spite of this, the electrode system and therefore the wires need to stay in place with a maximal uncertainty of 0.2 mm between the wire layers [Pra11].

In dedicated test measurements, prior to the finalization of the design, outgassing rates were estimated and thermal and mechanical stability was approved. Quality checks for every used material and designed part are described in detail in [Hil11] [Pra11]. With a specially developed measurement set-up a quantitative quality insurance for each wire electrode module has been enabled. A detailed documentation makes every step in the assembly process comprehensible.

3.2 Spectrometer baking and electrical short circuits

Prior to the first measurement campaign (SDS I) with the KATRIN main spectrometer and the Focal Plane detector (FPD) a bakeout was performed. This was the first time for the spectrometer section to be ramped to a temperature of 300 °C with a later cool down to room temperature. The elongation of the vessel and therefore the mechanical and thermal stress has not caused structural failures in the wire electrode system. However, it has been found that the baking process has led to several short circuits in the HV distribution of the inner wire electrode [SGW13]. These electrical short circuits occurred between several rings and outer and inner wire layers of the electrode, see figure 3.6.

Since measurements indicated that the wires of all modules are intact, the reason for the short circuits has to originate within the high voltage distribution [HOZW13]. Test measurements performed on the copper beryllium (CuBe) rods used in the HV distribution have shown that at temperatures above 200 °C, depending on the initial shaping, deformations occurred (see figure 3.7). The loss of stiffness during bakeout causes the longer CuBe lines to bend down onto the wire layers of the electrodes and therefore cause short circuits. In a report, the implications for the KATRIN experiment for measurement operations and therefore the neutrino mass measurement are covered [BCG+13]. It has been found that the transmission properties of the spectrometer are not impaired. Given that the dominant background in the main spectrometer does not come from surface electrons (thesis [Har15]) also the reduction in shielding efficiency, when the two layer system is effectively acting as a one layer electrode, can be tolerated. Nevertheless, to approach background in upcoming measurements an investigation of the wire electrode short circuits was performed and repair plans have been developed and partially performed [D+14].

3.3 Electrode repair

A repair strategy for the electrical short circuits of the inner wire electrode has to cope with several difficulties. Since the electrode covers the complete inner surface of the main spectrometer the access is restricted. The vessel can only be entered reasonably through the vacuum ports (diameter = 25 cm) on top of the spectrometer. Directly beneath the ports, with a distance of ~15 cm, the outer wire plane is situated. During a repair only UHV clean tools and materials could be used and had to be fixed to minimize the risk of falling into the spectrometer.

To develop a repair strategy a detailed investigation of the structural deformation of the CuBe rods has been performed. Therefore, a special manufactured zoomable swing prism borescope by Olympus (see figure 3.8) has been introduced through the opened ports. With a light source built into the tip of the borescope and an additional one guided next to it ,a sufficient illumination of the vicinity was given. A support to position the optical instrument and light source on the HV-ports made of acrylic glass and aluminium profiles provide safety against contamination of the spectrometer and uncontrolled movement of the borescope (see figure 3.9). With a DSLR camera equipped to the optical end of the instrument detailed photographs of the situation near the wire

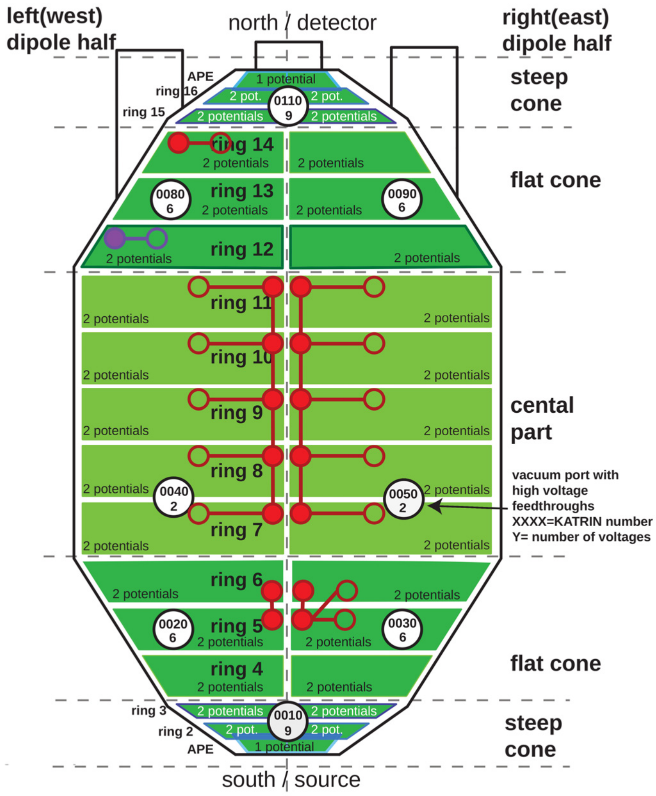

Figure 3.6: Overview of electrical short circuits after first spectrometer baking. In the sketch the electrode arrangement is shown for each ring and both dipole halves. The dots and circles denote electrical short circuits between outer and inner wire layer and bars show short circuits between rings. Additionally the red color describes permanent while purple shows temporary issues.

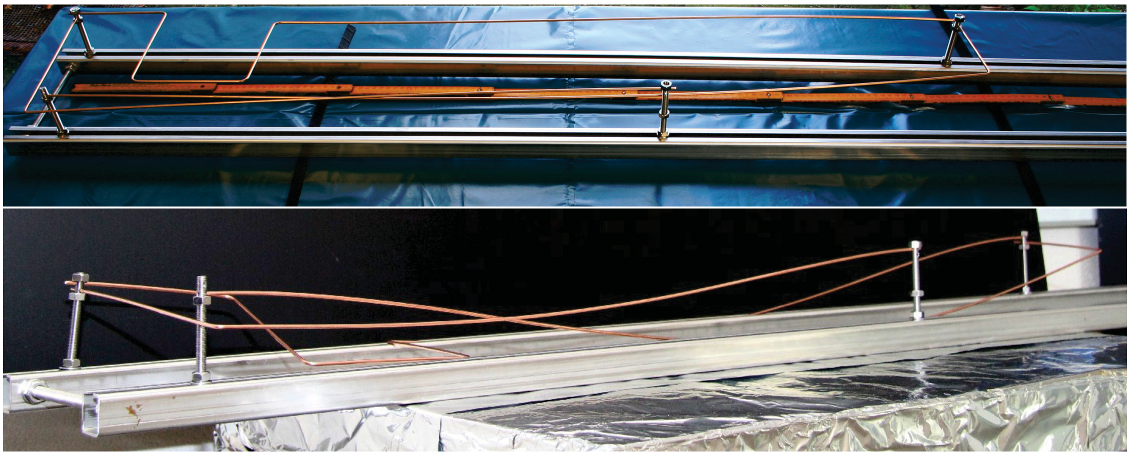

Figure 3.7: Copper beryllium rods before and after bakeout tests. The upper picture shows a test set-up with CuBe rods wiht length and shapes as they occure for the high voltage distribution inside the main spectrometer. After tempering several hours at temperatures of 300 °C the rods lost their rigidity during the process which causes a severe structural loss. Such measurements gave indication of the origin of the electrical short circuits at the wire electrode.

modules could be obtained. That way every copper beryllium rod could be traced and surveyed for short circuits.

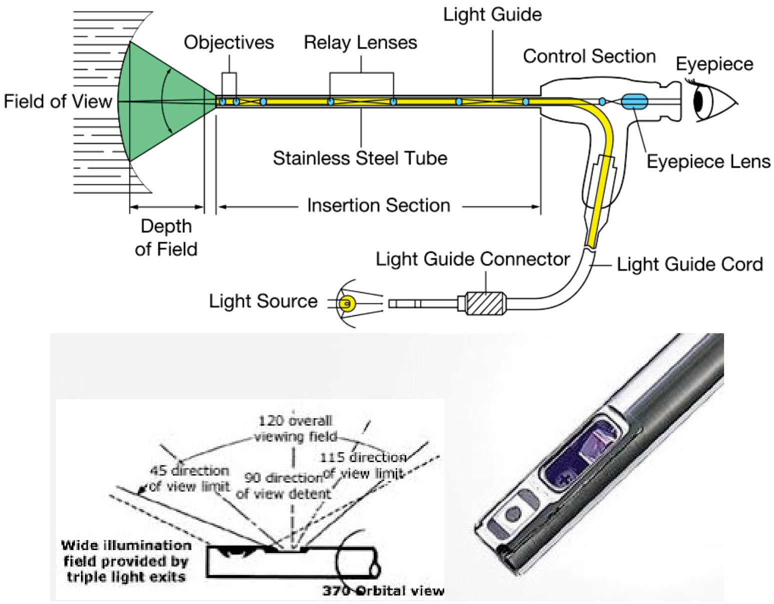

Figure 3.8: Sketch of borescope optics. The zoom swing prism [Oly15] provides an optical system which offers a true color and sharpness adjustable picture of near and far field. An inbuilt light guide allows to illuminate the surroundings with a external light source.

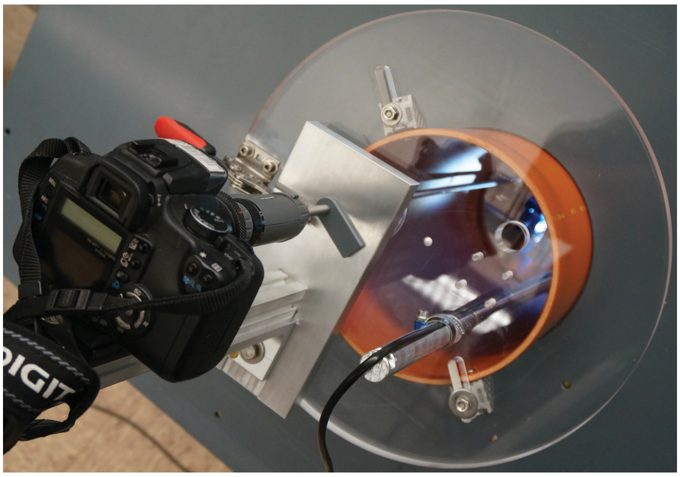

Figure 3.9: Set-up for investigation of the wire electrode. The borescope and additional light source is mounted on an acrylic glass lid. This layout provides free line of sight to the tip of borescope and prevents parts form falling into the spectrometer. With the camera attached to the borescope, detailed photos of the inside of the vessel can be taken.

Within the central part, rings 7 to 11 (see fig. 3.6) carry only two voltages per dipole half, one for the inner and one for the outer wire layer. The inner potential is connected by a copper beryllium rod, which is shaped in curves to reduce mechanical stress while baking. The loss of rigidity has led to a sagging in this structure and the CuBe touches the outer wire layer which can be seen in figure 3.10.

At the cones of the main spectrometer each high voltage distribution platform passes twelve voltages via CuBe rods. In figure 3.11 close-up photographs show several short circuits caused by copper beryllium. The sagging due to loss in stiffness during baking is clearly visible. The rods bent downwards touching the wire layers or the support frame of modules.

With the information gained from the optical inspection a repair was considered possible at least for some of the short circuits. To develop strategies two mock-ups, one for the central part (port 40/50) and another one for the flat cone (port 20/30 and 80/90), have been constructed in Münster with spare modules. These mock-ups were equipped with an artificial spectrometer vessel wall and a realistic model of a vacuum port, see figure 3.12. The copper beryllium rods used in the mock-up are fitted to imitate their deformed counterparts inside the main spectrometer. That way an accurate representation of the short circuit issue was accessible in a test set-up. The mock-up showed all issues, which had to be taken into account for a repair action. The given space constraints limited the possibilities for additional support structures,

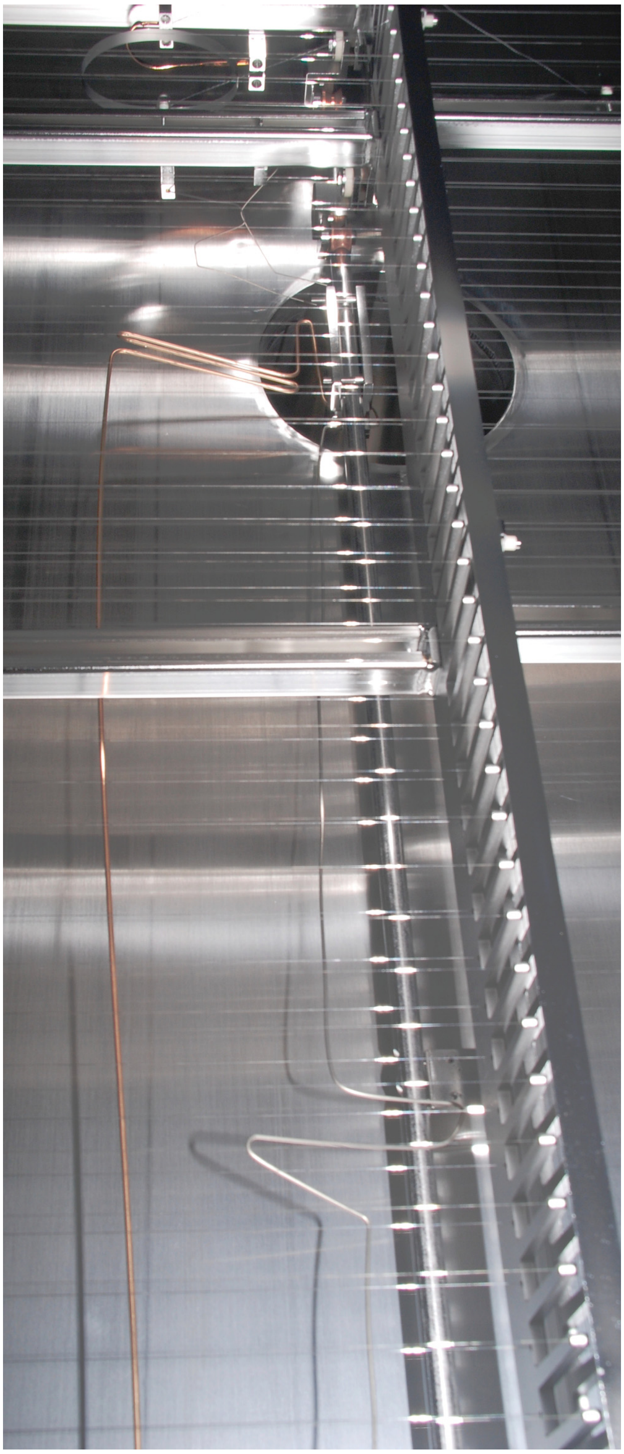

Figure 3.10: Picture of the high voltage distribution beneath port 40. High voltage connections in the spectrometer central part, ring 7 to 11, are carried out from a distribution platform via one CuBe rod for each dipole half. The curved shape of the copper beryllium got deformed during baking and subsequently touched the outer wire layer.

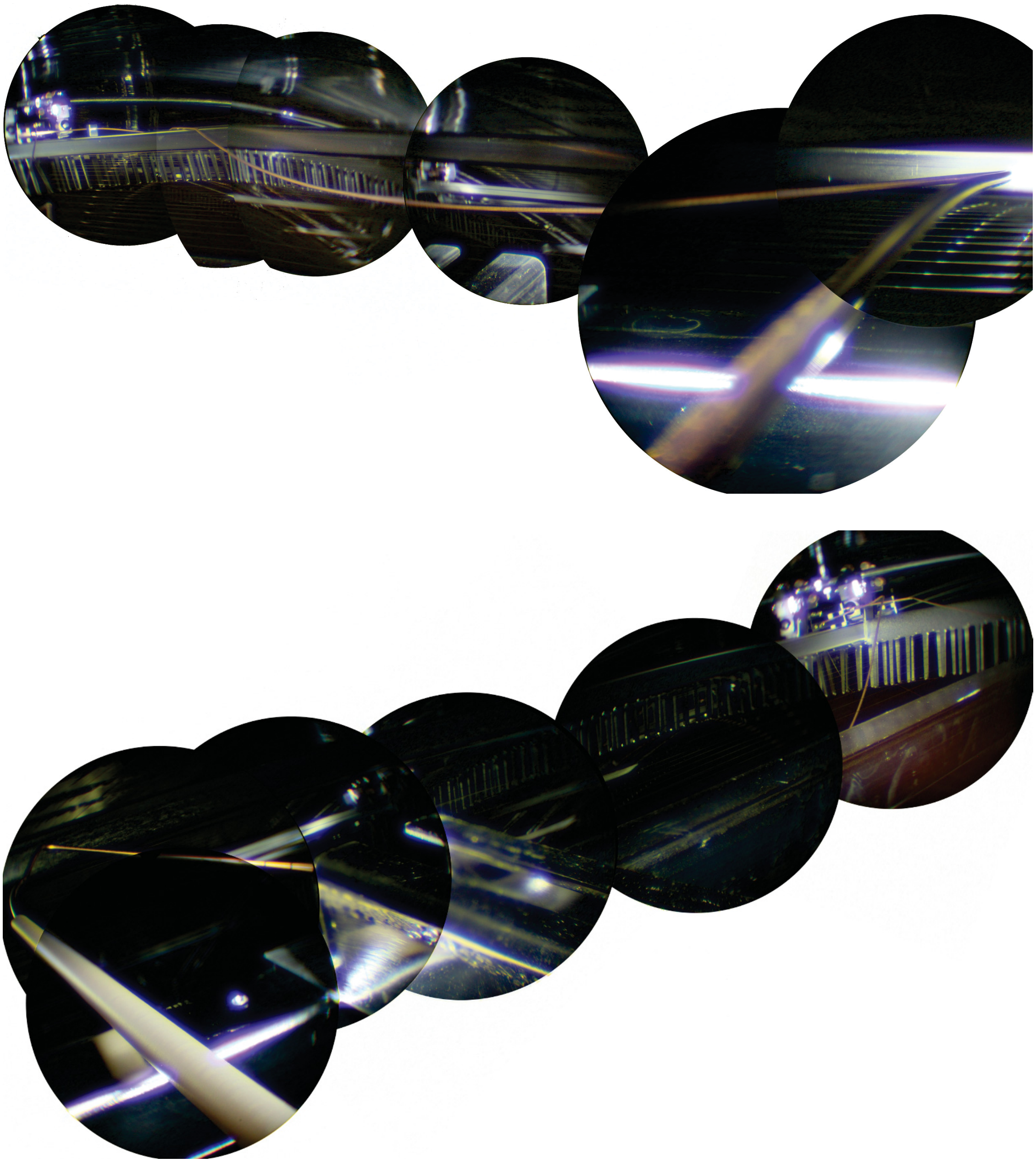

Figure 3.11: Electric short circuits underneath port 20 and 30. At these ports ten copper beryllium rods are used to route the high voltage to the various wire layers. The rods span distances up to 1.5 m without any further support structure. The sagging caused by thermal stress led to contacts between wire layer and CuBe.

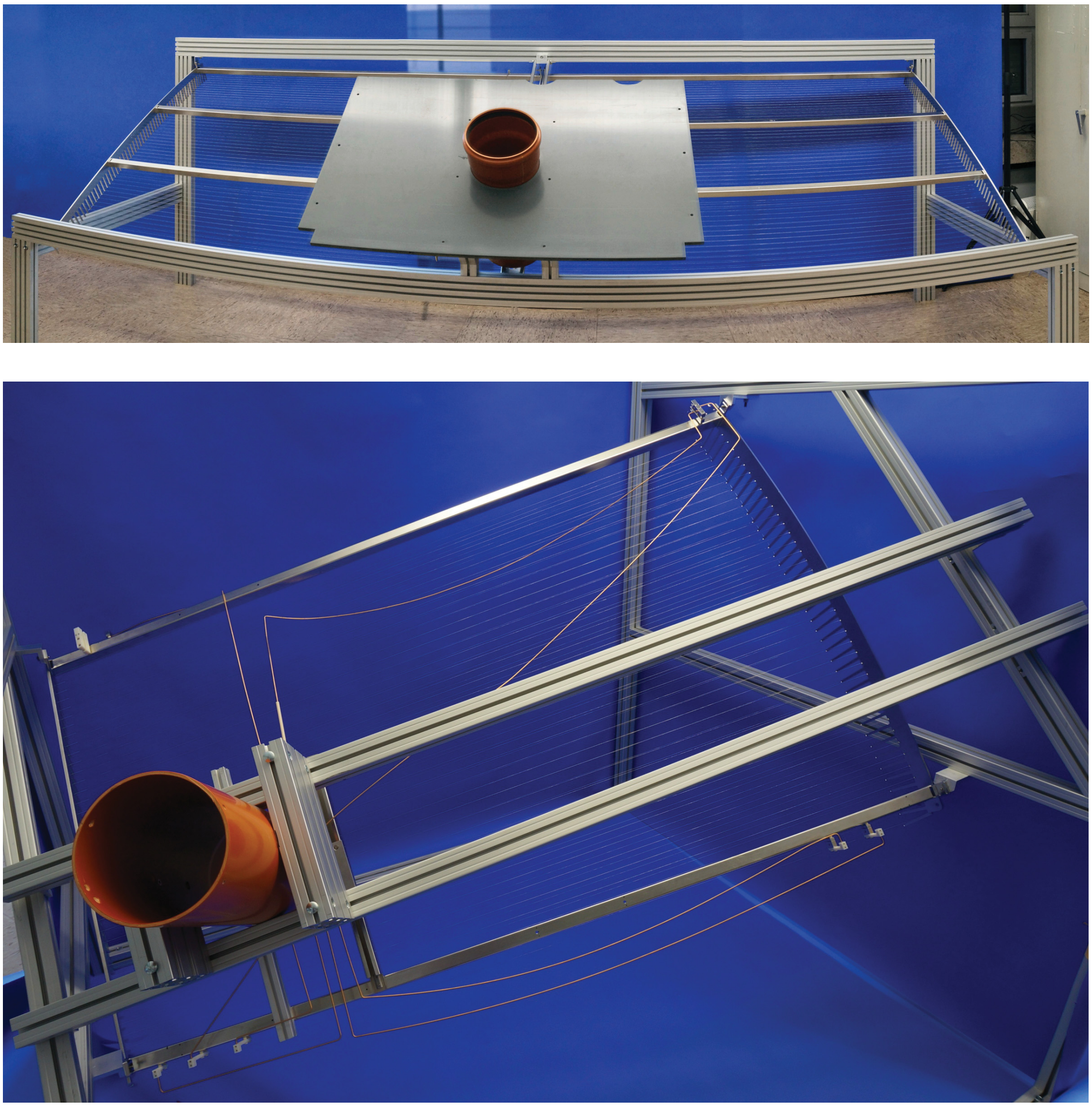

Figure 3.12: Mock-up for repair strategy development. To investigate repair solutions for the electrical short circuits, two test structures were assembled to mimic the situation inside the KATRIN main spectrometer. Spare modules of the central and flat cone part equipped with an artificial vessel wall and vacuum port make tests of realistic repair actions possible. Copper beryllium rods shaped to imitate the original short circuits reveal issues for new introduced holding structures.

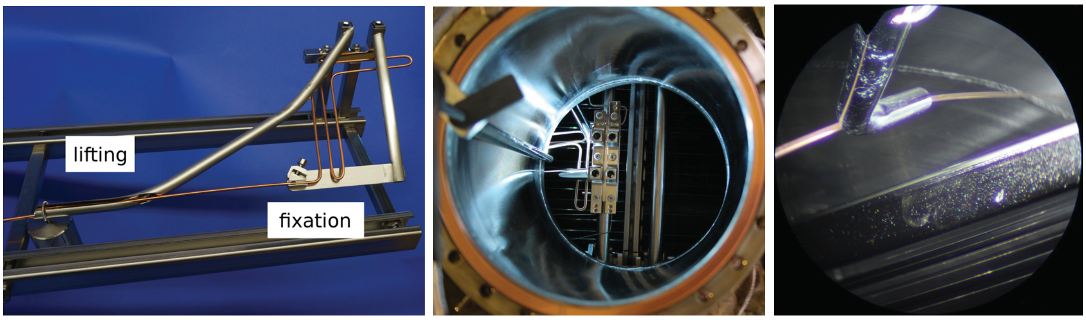

Figure 3.13: Wire electrode repair in central part. From left to right the pictures show the prototype parts for the repair, which was tested under ultra high vacuum conditions and temperatures up to 350 °C, a top view from the port shows the support parts mounted onto the high voltage distribution platform and a look through the borescope towards the uplifted CuBe rod after the repair action inside the spectrometer.

which can be introduced into the spectrometer. Parts are not allowed to penetrate through the wire layers during installation, because of the high risk of damaging the sensitive wires. Therefore curved components had to be developed, which can be inserted through the vacuum parts without protruding the wire planes and are suitable to permanently support the sagged CuBe lines. These holding structures had then to be fixed to the high voltage distribution platforms.

For the central part wire electrode only one CuBe rod has to be supported to remove the short circuit. Two stainless steel pieces were designed to lift up the rod and fix it to the new position to prevent issues by a later outbaking. Both parts are situated on the high voltage distribution terminal carrying the same voltage as the rod. The lifting piece, called spoon, consists of a preshaped tube with an upwards opening at the end, which encloses the copper beryllium. The fixation is realized by a screwable clamp, which is tightened after the installation inside the spectrometer, visible in figure 3.13.

For the cone sections of the main spectrometer the repair strategy was similar to the central part. Stainless steel spoons were designed and installed to support the copper beryllium in order to remove and prevent short circuits from reoccurring during further bakeout cycles. This was feasible for rods which do not extend to the corners of the distribution module. A special case occurred at port 30, where the long CuBe line was deformed so much during baking, that it is protruding through the wire planes (however without damaging the wires). A repair method using foldable support structures was developed, but considered too risky to be actually installed.

After the repair actions took place the vented spectrometer underwent electrical tests, which confirmed that all treated short circuits were successfully removed. With the evacuation of the main spectrometer vessel for the following measurement phase the electrical short circuit in the eastern central part reappeared, see figure 3.14. Another investigation with the described optical tools has been non conclusive because no visible connection between electrical parts could be observed and the venting released the short circuit again. One possible presumption is, that two springs interconnecting neighboring rings for inner and outer wire layer potential snap into a position where they touch each other due to the contraction of the vacuum vessel while evacuating. Since these springs are too far away from the vacuum ports and there is no direct line of sight to them this statement cannot be confirmed. Additionally, to survey the evacuated spectrometer a different (UHV compatible) investigation method would be necessary.

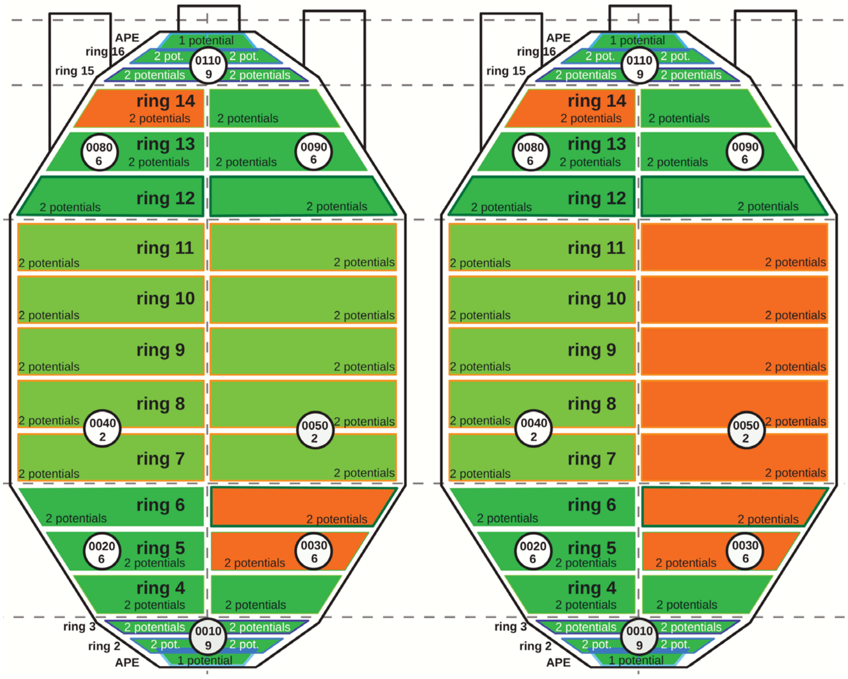

Figure 3.14: KATRIN main spectrometer vented (left) and evacuated (right). The left sketch displays the remaining electrical short circuits (orange) after the repair actions. The central part short circuits in both dipole halves and the interconnecting short between ring 5 and 6 have been successful repaired and showed no connection in the vented spectrometer vessel. On right hand side the spectrometer is evacuated and a short circuit reappeared within the eastern dipole of the electrode between inner and outer wire layer.

3.4 Effective potentials

Since the efficiency of background reduction of the fully functional double layer wire electrode could not be observed over longer periods due to electrical short circuits, a method to investigate the remaining double layer functionality has been developed. The underlying idea is to use the parts of the wire electrode which are fully operational, i.e. the western dipole half, in a double layer mode and the eastern half short circuited, see depiction 3.15. The potential of the eastern dipole half has to be set on such a value that the effective potential inside the spectrometer matches the effective potential of the double layer on the western side.

As stated in section 3.1.1 the effective potential of a double layer wire electrode for an axial symmetric vessel can be calculated with formula 3.8. The effective potential for a short circuited wire electrode is given through condition

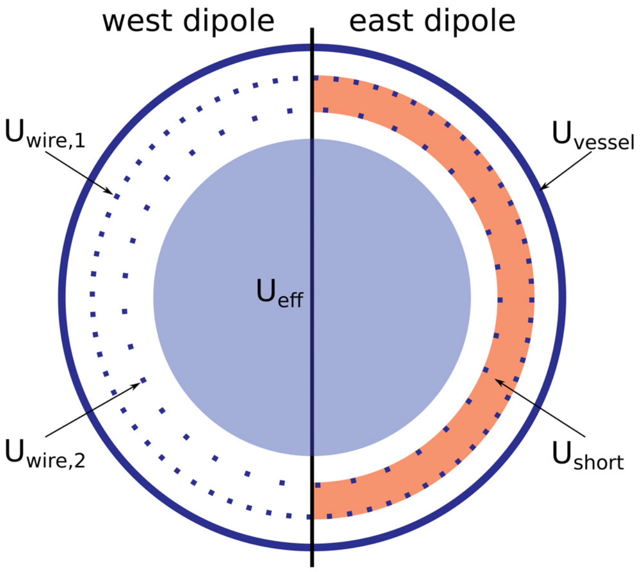

Figure 3.15: Configuration for effective potential measurements. The sketch shows an intersection of the KATRIN spectrometer with the inner wire electrode. For measurements the western dipole is used in double layer mode with two different potentials for each wire layer. The eastern half is short circuited and set to a potential U_{short} in a way that both dipole halves have matching effective potentials.

Table 3.3: Initial settings for the effective potential measurements with the main spectrometer. Vessel and short circuit potentials are fixed. The survey voltage is analytically calculated and then altered in the measurement

U_{vessel} / V	U_{short} / V	U_{survey} / V
-18500	-18600	-18609

$U_{\text{wire,1}} = U_{\text{wire,2}} = U_{\text{short}}$, yielding:

$$qU_{\text{eff,short}} = qU_{\text{short}} + \frac{qU_{\text{short}} - qU_{\text{short}}}{S_2} + \frac{qU_{\text{vessel}} - qU_{\text{short}}}{S_1 \cdot S_2} \tag{3.9}$$

$$= qU_{\text{short}} + \frac{qU_{\text{vessel}} - qU_{\text{short}}}{S_1 \cdot S_2} \,. \tag{3.10}$$

With the assumption, that in the far field the effective potential is not influenced by the boundary condition at the edges of the dipole halves equations 3.8 and 3.10 can be identified:

$$U_{\text{short}} + \frac{U_{\text{vessel}} - U_{\text{short}}}{S_1 \cdot S_2} = U_{\text{wire,2}} + \frac{U_{\text{wire,1}} - U_{\text{wire,2}}}{S_2} + \frac{U_{\text{vessel}} - U_{\text{wire,1}}}{S_1 \cdot S_2} \tag{3.11}$$

For later measurements it was chosen to fix U_{short} to a certain value and predefine:

$$U_{\text{vessel}} - U_{\text{wire,1}} = \frac{1}{2} \cdot (U_{\text{vessel}} - U_{\text{wire,2}}) \,. \tag{3.12}$$

This way, only one parameter, $U_{\text{wire,2}} = U_{\text{survey}}$, remains and is then expressed by:

$$U_{\text{survey}} = \frac{U_{\text{short}} \cdot (2 - 2S_1S_2) + U_{\text{vessel}} \cdot (S_1 - 1)}{1 + S_1 - 2S_1S_2} \,. \tag{3.13}$$

Based on equation 3.13, measurements with the potentials for U_{short} and U_{vessel} have been performed [DHRW14] [DRHK14]. The general mode of operation for the spectrometer is adapted from [Har14]. Herein, the aircoil system (LFCS) is used in a 5 G mode and the steep and flat cone inner electrodes are set to a common offset w. r. t. the vessel potential. In table 3.3 the potential settings for vessel and central part wire electrode can be found. During the measurement the survey potential was changed to more positive and more negative values around the analytically calculated optimal potential. At the optimal effective potential the background rate is expected to decrease due to the improved shielding by the functioning double layer wire electrode. For the other voltages the dipole character becomes dominant because of increasing $E \times B$ drifts of electrons.

Table 3.4: Near vicinity of optimal calculated effective potential for setting with −18 500 V vessel potential.

U_{survey} / V	run number	background rate / mcps
−18 608.0	21195	611 ± 13
−18 608.5	21201, 21247	604 ± 9
−18 609.0	21196, 21210, 21211	614 ± 8
−18 609.5	21202, 21206, 21207, 21245, 21246	563 ± 6
−18 610.0	21189, 21190, 21212, 21213	605 ± 8
−18 610.5	21203, 21214, 21215	608 ± 8
−18 611.0	21197, 21216, 21217	614 ± 8

For the measurement, the survey potential has been varied in 1 V steps from −18 600 V to −18 620 V with a refined 0.5 V stepping directly around the optimum. For an independent background estimation runs #21099-21104 of the SDS II measurement campaign were chosen. These utilize the same potential settings for the cone sections and the 5 G LFCS tuning. Herein, a background rate of 621 ± 6 mpcs has been found. In the effective potential measurement it can be seen that in the vicinity of the analytical calculated potential settings the background count rate decreases quickly down to 563 ± 6 mpcs (figure: 3.16). The rate drop is confirmed in five independent runs (21202, 21206, 21207, 21245, 21246). The direct neighboring runs were measured each up to four times to validate surrounding rates, see table 3.4. For even higher deviations from the optimal effective potential, the rate increases towards lower potentials and decreases at higher potentials. The diverse character in count rates could be reasoned by the varied drift fields occurring between double and single layer dipole half. This effects have not been investigated further in this thesis, since effects arising from special dipole settings of the spectrometer are discussed in [Hil17].

Looking at the background rate distribution of the FPD, see figure 3.17, the varying dipole characteristics through the survey can be seen. For the optimal effective potential settings the background level throughout the detector is evenly distributed, revealing no distinct features, which indicates a match between the dipole halves. With a western dipole at reduced potential w. r. t. the eastern half, the region of highest background activity is shifted towards the two dipole halves. The increased background levels can be seen from ring 3 to 12. In the opposite case the pattern shifts to the upper east and the highest background level is found only in the five outermost detector rings. A detailed investigation of the characteristics and implications caused by dipole

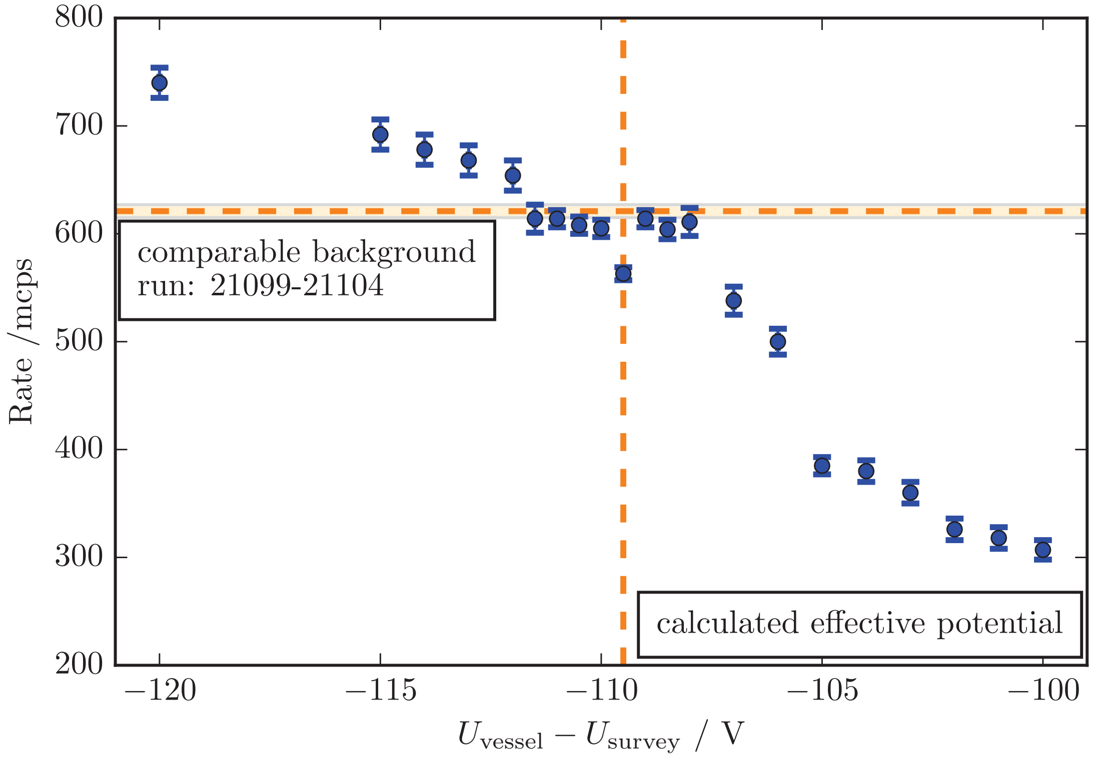

Figure 3.16: Altering U_survey with vessel potential fixed to −18 500 V. The dashed orange horizontal line denotes the average background, 621 ± 6 mpcs, determined in reference measurements (runs #21099-21104). At the calculated optimal potential, a clear rate decrease is visible compared to potentials in the direct vicinity. For potentials deviating further, increasing $E \times B$ drifts of background electrons and lead to fluxes that are no longer mapped onto the FPD, right hand side. Alternatively for the left side the background screening becomes less effective (western wire electrode).

drift fields and measurement modes for active background reduction is given in [Hil17].

Subdividing the detector into its eastern and western dipole halves, shown in figure 3.18 (a) and (b), allows an independent investigation of each side. To prevent overlap between the datasets pixel 7, 13, 31, 37, 55, 61, 79, 85, 103, 109, 127 and 133 are excluded since they cross the dipole boundaries. The rates for each ring segment have been weighted by their fraction of the full circle. Figure 3.18 displays the background rates measured in the FPDs rings separately for the eastern and western electrode halves. The background of the innermost volume of the spectrometer (ring 0 - 7) is comparable. For rings above 8 the difference becomes prominent, here the rate for the fully functional double layer inner electrode is decreased.

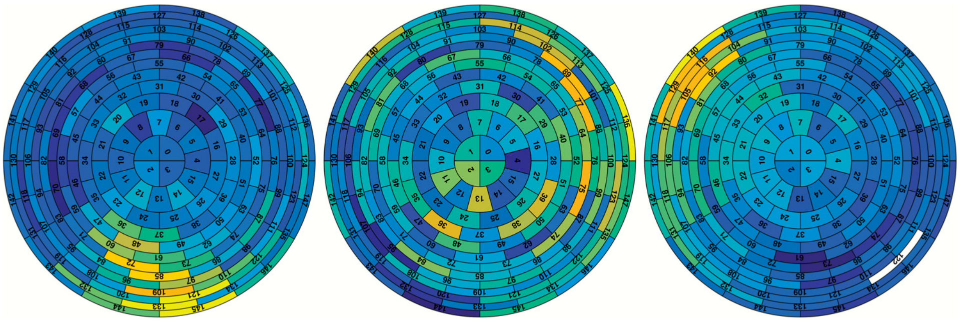

Figure 3.17: Dipole formation for potentials deviating from the optimal effective potential. For potential settings with more positive or negative voltage U_{survey} the dipole character becomes prominent. From left to right the FPD rate histogram shows a negative potential in the western dipole half, the optimal settings and an increased negative potential in eastern half. The shift of higher rate on the FPD disc is typical for increased drift fields [Hil17].

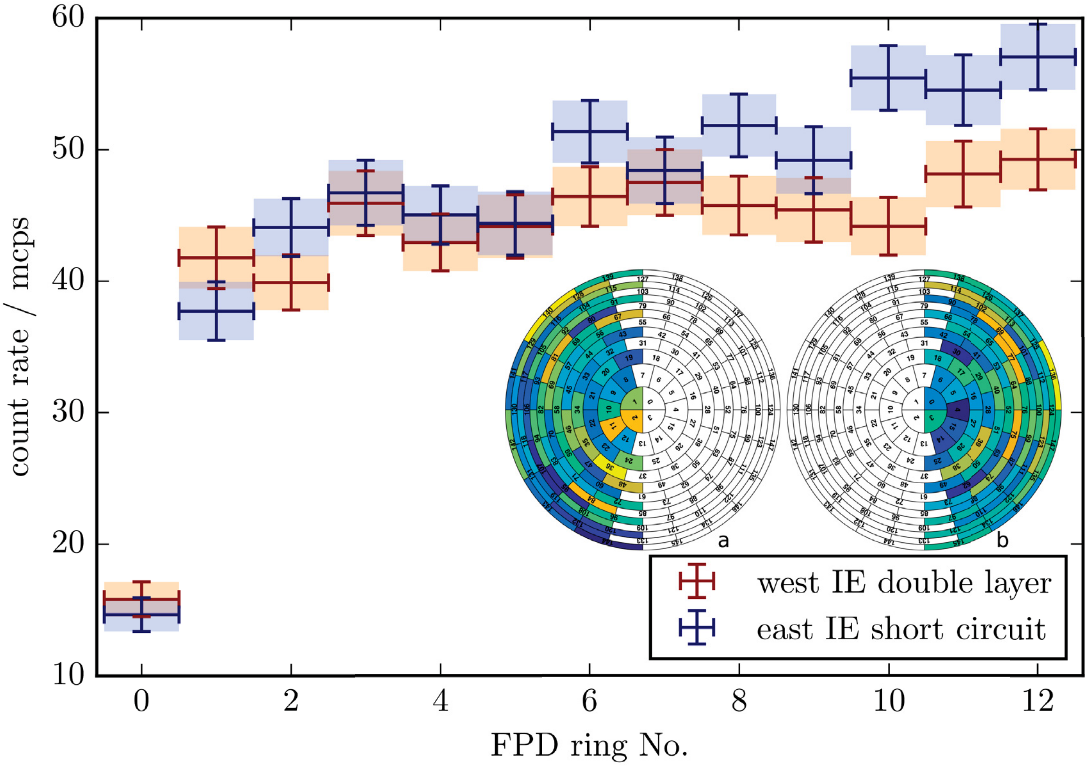

Figure 3.18: Detailed background distribution for eastern (a) and western (b) dipole half. A ring-wise consideration of background events at the FPD shows that for the inner volume of the spectrometer (up to ring 7) the count rate is less affected. For the rings 8 to 12 the background rate is noticeable decreased with a double layer compared to the short circuited part.

3.5 Measurements with temperature gradients

As mentioned in section 3.3, after the wire electrode repair an electrical short circuit between inner and outer wire layer reappeared in the eastern dipole half of the KATRIN main spectrometer. However, during the ramping of the temperature for the vacuum bakeout this short circuit vanished for a certain time, which led to a measurement proposal making use of a temperature gradient to investigate the full screening potential of the central spectrometer part with a functional double layer electrode.

As described in [DKR+15] the main spectrometer has been cooled down at the end of February 2015 with an LFCS setting of 3.8 G and electrode set to potentials denoted in table 3.5. With different set values for inner and outer wire layers in rings 7-11, a removal of the short circuit would be observed directly. Unfortunately this didn't happen directly in the cool-down period, but only later, when the main spectrometer was set to warm up again. With the positive temperature gradient the electrical short circuit vanished indeed.

Table 3.5: Initial potential settings to observe a release of the short circuit between inner and outer wire layers

Ring	U_{inner} / V	U_{outer} / V
2,16	-18420	-18400
3,15	-18560	-18500
4, 5, 6	-18577.5	-18577.5
12, 13, 14	-18577.5	-18577.5
7-11	-18600	-18500

To measure as many complete runs as possible the potential settings of wire electrode and vessel as well as LFCS mode have been set by a script, which changed the setting every 15 min to a new set-up and started a new run, so that numerous datasets could be obtained.
For the wire electrode two different settings, tables 3.6 and 3.7, have been used. The first one is adapted from [Zac14] with a smoothed potential transition between steep and flat cone. The latter is used for direct comparison with measurements done in [Erh16]. Here the steep cone electrode potentials are only slightly more negative then the vessel potential. For a direct comparison between double layer and short circuited electrode operation, inner and outer

layer have been short circuited artificially for some runs in each measurement setting. These runs are denoted with an asterisk (*) in table 3.8.

Table 3.6: Potential setting A - adapted from [Zac14]

Ring	U_inner / V	U_outer / V
2,16	-18420	-18400
3,15	-18560	-18500
4,14	-18577.5	-18577.5
5,6	-18577.5	-18577.5
7-11	-18600	-18500
12	-18577.5	-18577.5
13	-18577.5	-18577.5

Table 3.7: Potential setting B

Ring	U_inner / V	U_outer / V
2,16	-18503	-18503
3,15	-18503	-18503
4,14	-18577.5	-18577.5
5,6	-18577.5	-18577.5
7-11	-18600	-18500
12	-18577.5	-18577.5
13	-18577.5	-18577.5

Furthermore three different LFCS modes have been tested, which include standard $B = 5\,\text{G}$, a setting with double magnetic field minimum at $B = 3.8\,\text{G}$ (d) and with single minimum at $B = 3.8\,\text{G}$ (s). In figure 3.19 the shape of the outermost magnetic fieldline, which connects to the edege of the focal plane detector, is illustrated for the various magnetic field settings [Erh16]. The indicated $B = 9\,\text{G}$ operation mode has not been included into the double layer test since the other ones are more likely to be used in tritium runs for the neutrino mass measurements.

With the described measurement plan, data for each setting could be taken, for time periods between 1 h and 1.5 h, until the short circuit reappeared and further double layer investigations have been set to an end. A summary of the successfully finished runs and their corresponding spectrometer potentials are given in table 3.8.

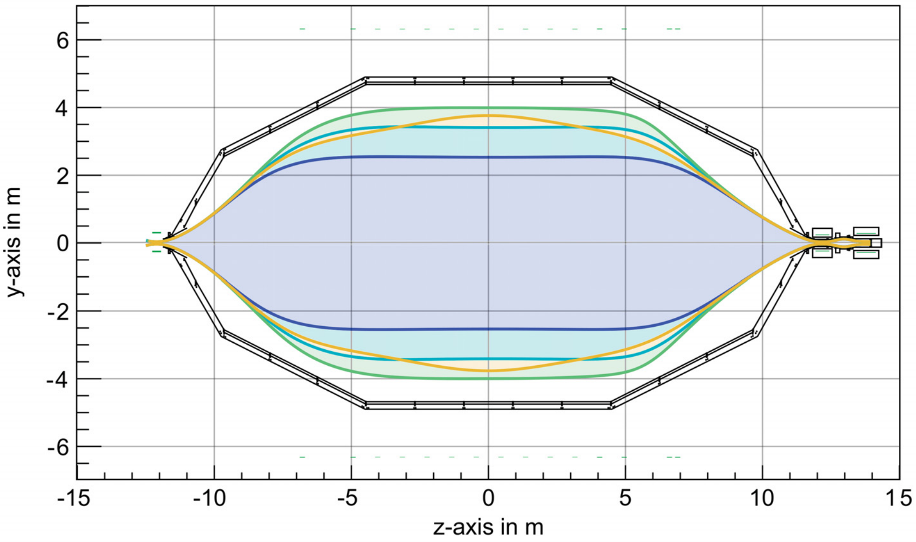

Figure 3.19: Magnetic field settings used during the SDS II measurements. Shown are the most relevant magnetic field setting during the measurement phase. Green: double minimum 3.8 G (d); orange: single minimum 3.8 G (s); light blue: 5 G; dark blue: 9 G as described in [Erh16].

Table 3.8: Run summary with double layer electrode potential during spectrometer warm up.

Potential setting	LFCS	runs
A	3.8d	23347, 23348, 23363, 23364, 23379, 23380
A*	3.8d	23349, 23350, 23365, 23366, 23381, 23382
A	3.8s	23351, 23352, 23367, 23368
A*	3.8s	23353, 23354, 23369, 23370, 23385, 23386
B	3.8d	23355, 23356, 23371, 23372
B*	3.8d	23357, 23358, 23373, 23374, 23389, 23390
B	5	23359, 23360, 23375, 23376
B*	5	23361, 23362, 23377, 23378

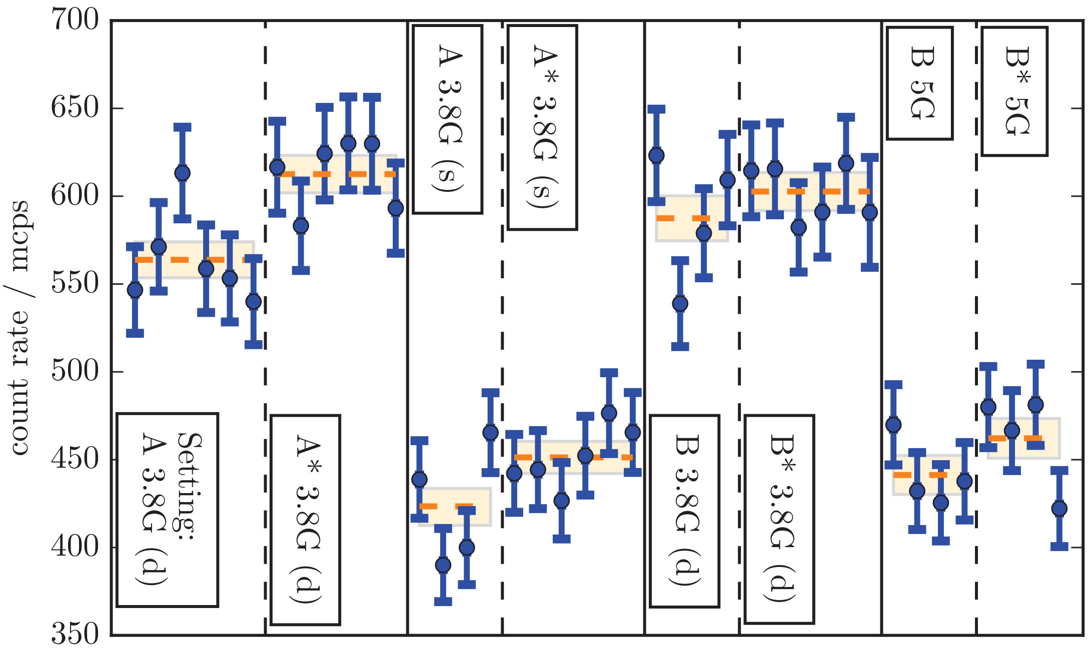

Figure 3.20: Background count rates for different measurement settings with and without a functional double layer IE. Indicated are the four different measurement set-ups (A/B) and their corresponding short circuited ones (A*/B*). The blue data points correspond to single runs whereas the orange bands describe the mean value and uncertainty during a single field and potential configuration. In black vertical lines the transition from one to another setting is marked.

Plot 3.20 shows the background rates for each setting. In blue the rates for the individual runs with their corresponding uncertainties are given, whereas the orange bands show the mean rates and uncertainties for all runs of a given setting. The continuous vertical line denotes a switch to a completely different operation mode, whereas the dashed lines mark the transition from a working double layer mode to the corresponding short circuited configuration. Between setting A and A* with double minimum $B = 3.8\,\mathrm{G}$ magnetic field the rate increases most prominently. A change from $564 \pm 10\,\mathrm{mcps}$ to $613 \pm 11\,\mathrm{mcps}$ corresponds an effect of ~9 % for a functional double layer wire electrode within the central part and separated potentials at the steep cones. Using the $B = 3.8\,\mathrm{G}$ setting with single minimum decreases the overall background level due to the decreased volume inside the spectrometer seen by the FPD. Here the difference in background rates decreases to ~7 %. Comparing the last two settings the effect of the double layer is further decreased and the uncertainties between double layer and short circuited settings overlap.

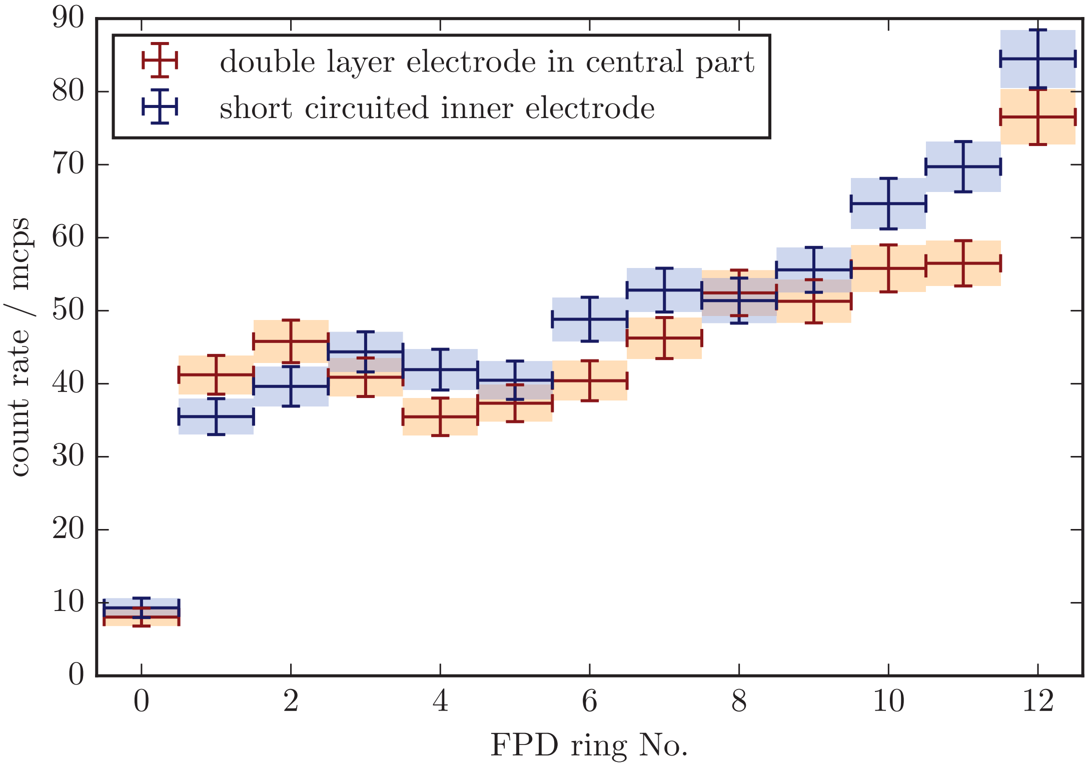

Figure 3.21: Ring-wise background count rates. Displayed are the count rates of the FPD rings for setting A (orange) and A* (blue) with a magnetic field setting of 3.8 G (d). For the innermost rings the background rates are comparable while they deviation increases above ring nine.

To gain a further understanding of the background distribution inside the spectrometer a ring-wise background determination is useful. Concerning the A and A* setting at 3.8 G(d) this is shown in figure 3.21. The short circuited measurement mode, denoted in blue, undershoots the double layer configuration for the three innermost pixel rings. Above that the rate increases above the double layer electrode and becomes most pronounced for the three outermost rings.

Since the overall rate drops to lower levels for higher magnetic fields or settings, which shape the outermost field lines to cover less of the spectrometer volume, the background distribution is observed to be a volume depended effect [Har15]. Nevertheless the double layer measurements indicate that the background rate decreases for higher radii more distinctly with a fully functional inner electrode compared to a short circuited one.

Chapter 4

Alternative field configurations and electron spectroscopy

Since the background of the main spectrometer is higher than expected, compared to the design considerations, sophisticated investigations have been performed to study its origin. Measurements of radioactive contaminations embedded in the concrete of the spectrometer building [RK$^+$18] and the vessel of the main spectrometer or properties like pressure and temperature dependencies [Har15] of the background provided contributions, but could not explain the whole background. Further contributions by secondary electron emission from the wall induced by muons from cosmic rays add only a fraction [ABB$^+$18a]. Moreover radon induced background, which originates mainly from the getter pumps, could not explain the composition off all background events [Har15]. The experimental observations indicate a volume depended background, originating not from a spatially confined source, but rather the complete inner volume of the spectrometer. These measurements altered the effective volume in front of the FPD by using different magnetic field settings, which minimized the flux tube expansion [Har15] [Erh16].

With all countermeasures (e.g. inner wire electrode and active cooled baffles) in place, the remaining background does not match the design value of 10 mcps [A$^+$05]. To investigate methods reducing the background, alternative field settings for the main spectrometer have been studied. Therefore, the magnetic field minimum and the maximum of the electric potential have been shifted towards the entrance or exit of the spectrometer. Thus the analyzing plane, where lower energy electrons are reflected, is shifted. These potential and field variations alter the active volume between analyzing plane and focal plane detector and allow to study the background behavior as a function of volume. Additionally, electron spectroscopy can be performed to examine the energy composition of the remaining background. The electric potential in the analyzing plane can be increased such, that only background electrons with certain kinetic energies can overcome the blocking potential. In Kassiopeia simulations, electrons with different kinetic energies can be started inside the active volume of the spectrometer and can be examined for their transmission properties. In a fit the most probable energy distribution can be derived from the measured background electrons and simulations at different blocking potentials.

The following sections detail the measurement methods used for the background investigations with a shifted analyzing plane. Furthermore, the spectroscopy measurement and simulations will be explained in detail.

4.1 Alternative field settings for measurements

The segmentation of the inner wire electrode (see section 3.1) and the individually adjustable coil currents of the LFCS allow a fine shaping of the electric potential and magnetic field inside the main spectrometer [EBB+18]. Since the central rings of the wire electrode are electrically connected, a shift of the electric potential can only be realized using the flat and steep cone rings. At these positions an increased potential is introduced to create an additional blocking potential either on the detector or the source side. Table 4.1 represents the settings used in the SDS II measurement campaign. Here electrode rings 5 and 6, respectively rings 12 and 13, are set to a more negative potential compared to the central rings, thus introducing an additional effective potential barrier of 10 V to 15 V with a significant radial dependence (see figure 4.1). The potential simulations were done with the Kassiopeia software framework [FGT+17].

The magnetic field minimum is shifted likewise by modified current settings for the LFCS coils (see figure 4.2) towards either source or detector side flat cone. The magnetic field simulations are based on an optimization algorithm introduced in [Erh16].

Because the electric potential can only be reasonable altered in rings 5 and 6 or ring 12 and 13, the magnetic field minimum is computed to come as close as possible to that position. For the detector side flat cone this is shown in figure 4.3. Better agreement between electric potential maximum and magnetic field minimum is difficult to achieve, since the spectrometer is not designed to operate with such field settings. The current set-up of the LFCS

Table 4.1: Inner electrode settings used to create an increased potential barrier at the flat cone on the detector/source side of the main spectrometer. All potentials are given in V.

Setting	U_{Vessel}	ΔU_{Ring2}	$\Delta U_{\text{Ring3,4}}$	$\Delta U_{\text{Ring5,6}}$	$\Delta U_{\text{Ring7-11}}$	$\Delta U_{\text{Ring12,13}}$	ΔU_{Ring14}	$\Delta U_{\text{Ring15,16}}$	Comments
Source	-18500	-90	-100	-120	-100	-100	-100	-90	ΔU_{Ring3} accidentally set to -100 (instead -90)
Detector	-18500	-90	-100	-100	-100	-120	-100	-90	

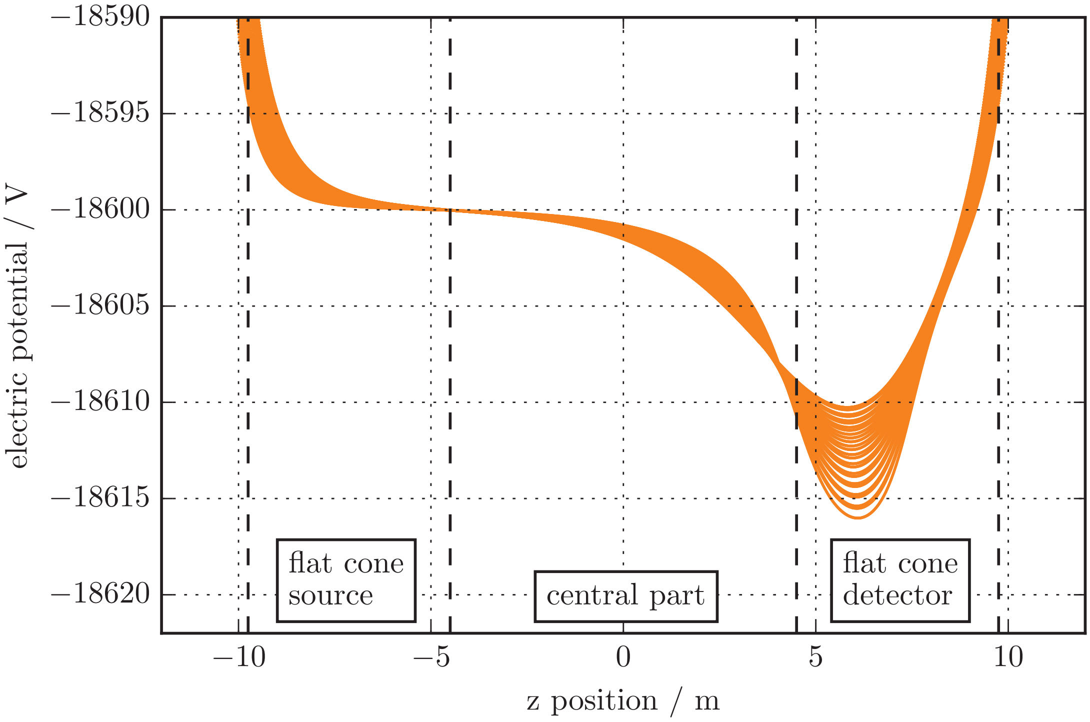

Figure 4.1: Additional blocking potential at the detector side flat cone. With the special electric potential settings for the inner wire electrode system (table 4.1) an increased blocking potential for electrons can be introduced. In this case, the potentials in the flat cone rings 12 and 13 are set to a 20 V more negative value.

Table 4.2: Optimized LFCS settings to implement the magnetic field minimum at either source or detector side of the main spectrometer. All currents for the LFCS are stated in A.

Setting	AC 1	AC 2	AC 3	AC 4	AC 5	AC 6	AC 7
Source	9.0	51.7	33.4	40.6	75.6	93.3	73.7
Detector	47.5	62.1	78.5	94.8	55.4	71.6	98.5

Setting	AC 8	AC 9	AC 10	AC 11	AC 12	AC 13	AC 14
Source	92.9	66.2	0.8	31.2	40.1	88.3	-17.2
Detector	94.4	99.0	52.8	43.6	-27.8	52.1	37.8

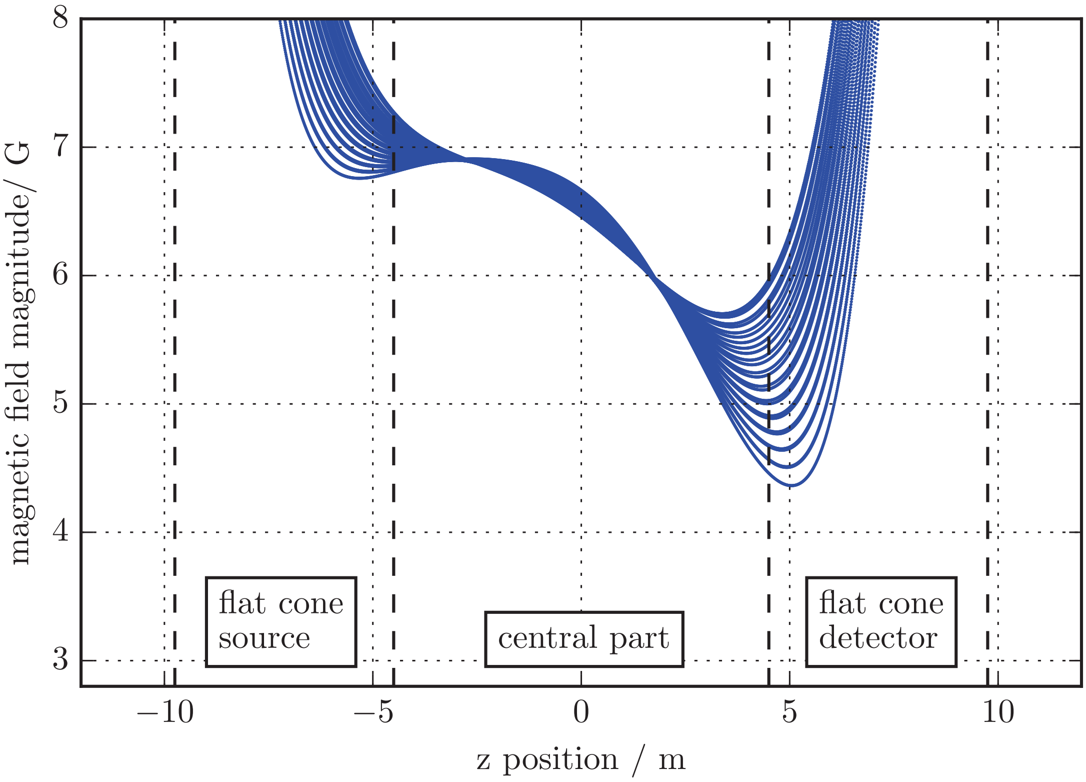

Figure 4.2: By varying the LFCS currents the magnetic field shape can be manipulated, which is shown in this figure, for the currents given in table 4.2.

prohibits further shifts of the magnetic field towards the flat cones of the spectrometer vessel. The spread of ~0.4 mT of the magnetic field at the electric potential extremes is acceptable, considering the overall field strength ranges from 0.4 mT to 0.8 mT, which is comparable to the anticipated field settings for KATRIN tritium operation.

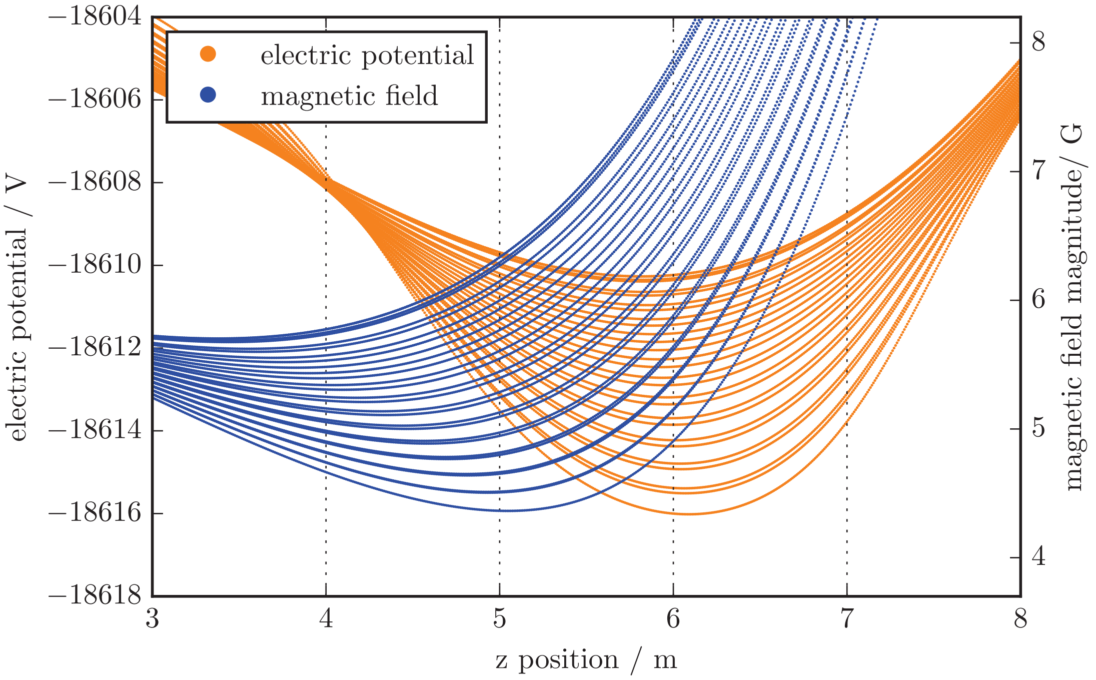

Figure 4.3: Detailed view of magnetic field strength and electric potential at the position of the shifted analyzing plane. The extrema of magnetic field and electric potential concur in the same region of the flat cone of the main spectrometer. Since the LFCS system and the inner wire electrode are not designed for such a measurement mode, deviations from a perfect overlap are unavoidable. Nevertheless, the magnetic field gradient at the electric potential maximum is low enough to consider this measurement setting.

With the maximal electric potential and minimal magnetic field shifted to the flat cone inside the main spectrometer, the position of electron energy filtering is also shifted. This plane of energy filtering is called analyzing plane. Using the electric and magnetic field settings to move the analyzing plane to different positions inside the main spectrometer, one can investigate volume dependencies of the spectrometer background. Low energy electrons, which are created inside the main spectrometer volume before or behind the analyzing plane, leave the vessel towards the corresponding side. This low energetic background is expected to change and therefore alter the count rate on the FPD, according to the flux tube volume seen by the FPD. A shifted analyzing plane, positioned at the source side of the spectrometer should increase the background count rate, whereas an analyzing plane near the spectrometer exit should lead to a rate decrease.

During the SDS II measurement campaign, background measurements with shifted analyzing planes have been performed. In run #22184 and #22185 an analyzing plane at the source side flat cone lead to a background rate of 709 ± 10 mcps. With an analyzing plane at the detector runs #22188 to #22190 decreased the background level to 165 ± 4 mcps [DEH$^+$15]. For comparison with a standard analyzing plane setting, a 5 G setting was chosen. The minimal magnetic field strength represents a mean value of the spread in magnetic field strength for the shifted analyzing planes. For the runs #21999-#22005 the background rate resulted in 477 ± 5 mcps. In figure 4.4 the rates are plotted against the flux tube volume between the two analyzing plane settings and the detector surface. The measured count rates show a linear relation between rate and volume with a proportionality of:

$$f(x) = 1.72 \pm 0{,}03\,\mathrm{mcps/m^3} \cdot x + 79.97 \pm 4.88\,\mathrm{mcps} \tag{4.1}$$

The measurements confirmed that the background rate is volume depended and decreases drastically for potential and field settings shifted towards the spectrometer exit. For tritium β-measurements a shifted analyzing plane at the detector side flat cone could be considered. Detailed simulations and measurements are needed to investigate the pros and cons of such settings. Section 4.4 shows measurements regarding the transmission properties of the main spectrometer with the detector-side analyzing plane set-up.

The following section 4.2 describes background measurements of the main spectrometer with shifted analyzing plane and different blocking potentials.

4.2 Blocking potentials

The additional electric potential applied to the flat cone region can be used as a blocking potential. To obtain information about the energy distribution of the observed background electrons the background rate for blocking potentials of varied magnitude is investigated. For this purpose one would like to use a spectrometer setting with increased energy resolution, yet a background level similar to the nominal operation. The spectrometer resolution is given by equation 2.2.2, that can be written as

$$\Delta E_{\mathrm{spectrometer}} = qU_{\mathrm{ret}} \cdot \frac{B_{\mathrm{ana}}}{B_{\mathrm{max}}} \,. \tag{4.2}$$

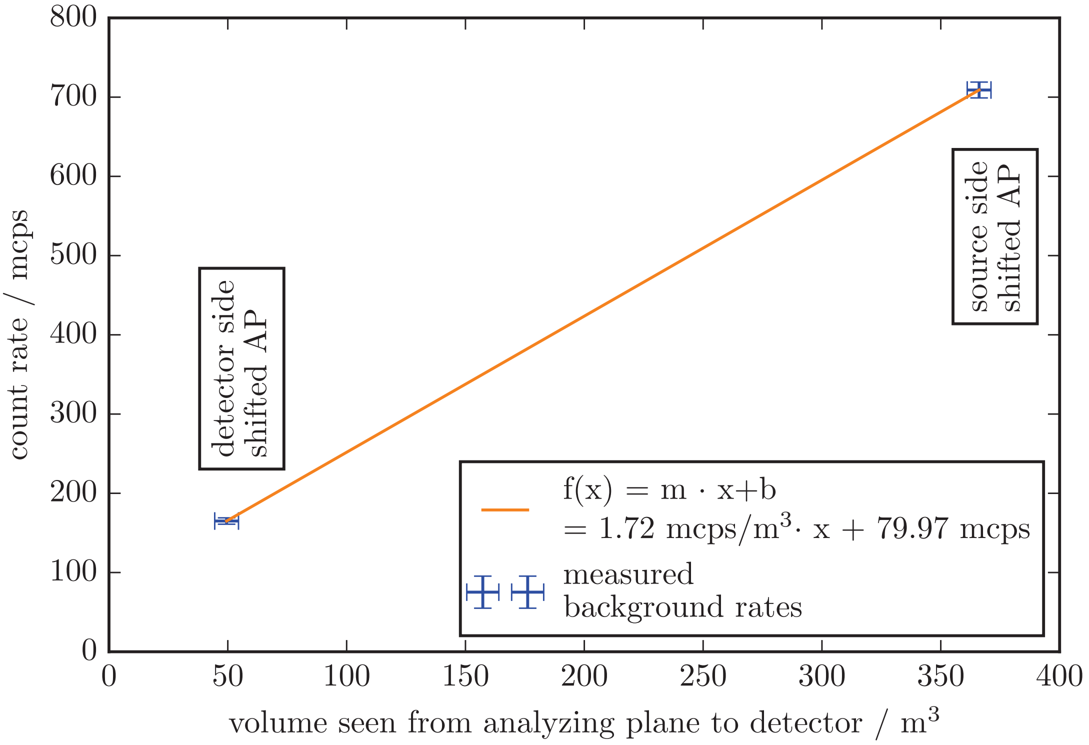

Figure 4.4: Volume dependency between count rate and flux tube volume. The plot shows the measured background count rates for the shifted analyzing plane settings at source and detector side. The denoted volume is defined by the flux tube volume between analyzing plane and detector surface. The errors shown for the volume are motivated by the inhomogeneities in the analyzing plane. A precise calculation needs to take possible misalignments and field inhomogeneities into account.

Table 4.3: Observed background rate for different retarding potentials [DRTO15].

retarding potential / V	Run No.	BG Rate / mcps
-20	24978	64 ± 6
-50	24977	93 ± 8
-250	24976	237 ± 12
-500	24975, 24979, 24988, 24989	320 ± 5
-700	24974	347 ± 14
-1000	24973, 24980, 24987, 24990	378 ± 6
-2000	24972, 24981, 24986	437 ± 7
-4000	24971, 24982, 24985	483 ± 7
-6000	24970, 24983	551 ± 9
-10000	24969, 24984	550 ± 10

Table 4.4: Optimized LFCS settings for a 6 T pinch magnetic field and detector side analyzing plane.

AC 1	AC 2	AC 3	AC 4	AC 5	AC 6	AC 7
98,00	97,94	98,00	98,00	98,00	98,00	98,00
AC 8	AC 9	AC 10	AC 11	AC 12	AC 13	AC 14
98,00	98,00	98,00	98,00	98,00	-96,11	67,00

Since the background electrons originate from the spectrometer volume, their starting energy depends on the local electric potential. Experimentally it has been observed that the background rate rises with the applied retarding voltage and saturates at a given point. This measurement is shown in figure 4.5 [DRTO15].

After the measurements in section 4.1 have been executed, the magnet at the exit of the spectrometer (pinch magnet) has been ramped up to 6 T. Therefore a recalculation of the optimized LFCS settings was mandatory. In table 4.4 the new aircoil currents can be found for the detector side shifted analyzing plane. The magnetic field minimum at the electric potential extreme is of the order of 0.5 mT. With this conditions, the spectrometer resolution improves according to equation 4.2, to:

$$\Delta E_{\text{spectrometer}} = e \cdot -6\,\text{kV} \cdot \frac{0.5\,\text{mT}}{6\,\text{T}} = 0.5\,\text{eV}\,. \tag{4.3}$$

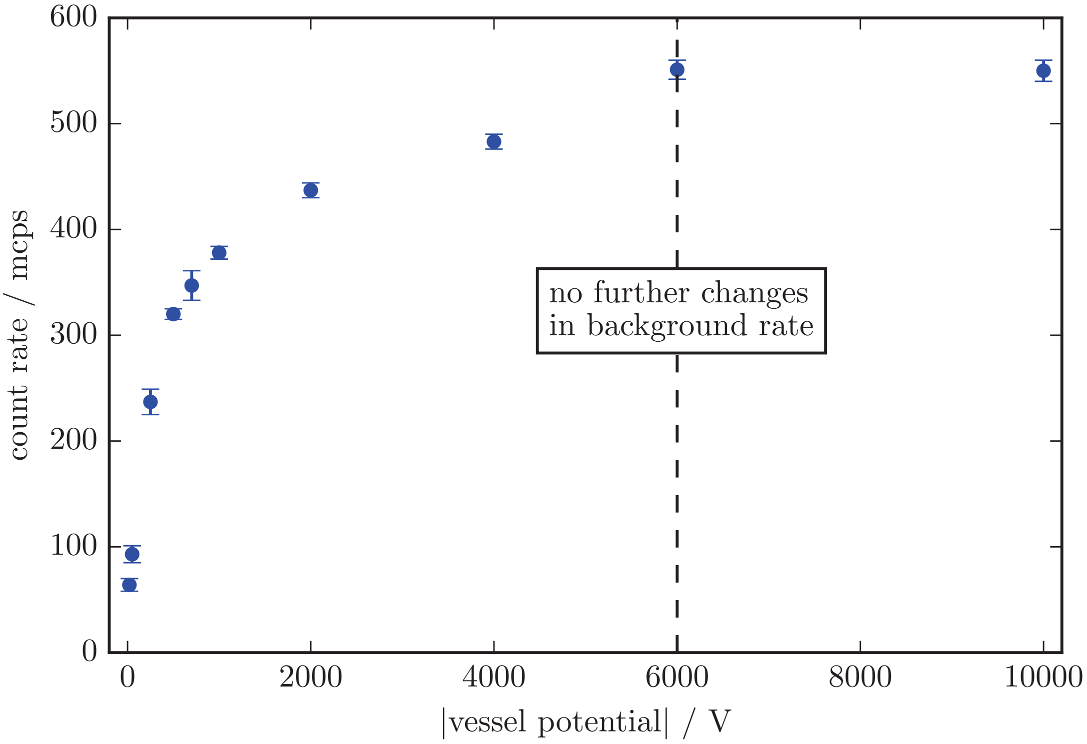

Figure 4.5: Background count rate dependence at different vessel potentials. The survey shows that the background rate saturates at a potential of $|U_{\text{vessel}}| = 6\,\text{kV}$.

Beginning with these spectrometer and LFCS settings, additional blocking potentials U_{blocking} are introduced at ring 12 and 13. For the background measurements these are increased stepwise from $U_{\text{blocking}} = 0\,\text{V}$ to $U_{\text{blocking}} = 20\,\text{V}$. The upper plots in figure 4.6 illustrate the simulated potential penetration for different blocking potentials and for different radii within the magnetic flux tube. For the outermost magnetic field lines (brighter colors in the upper figures 4.6), the potential penetration is most prominent.

As a consequence of the blocking potential, the point of electron energy filtering, where the electric potential has its maximum, shifts towards the detector side flat cone. For a vanishing blocking potential, the analyzing plane is nearly uniform and centered in the spectrometer vessel (see lower figure 4.6). Low blocking potentials lead to a strong deformation of the analyzing plane, where the electric field maximum for the inner radii is still near the spectrometer center, while the outermost analyzing point is already positioned at the flat cone. Higher blocking potentials locate the analyzing plane completely in the flat cone region and have a more homogeneous shape.

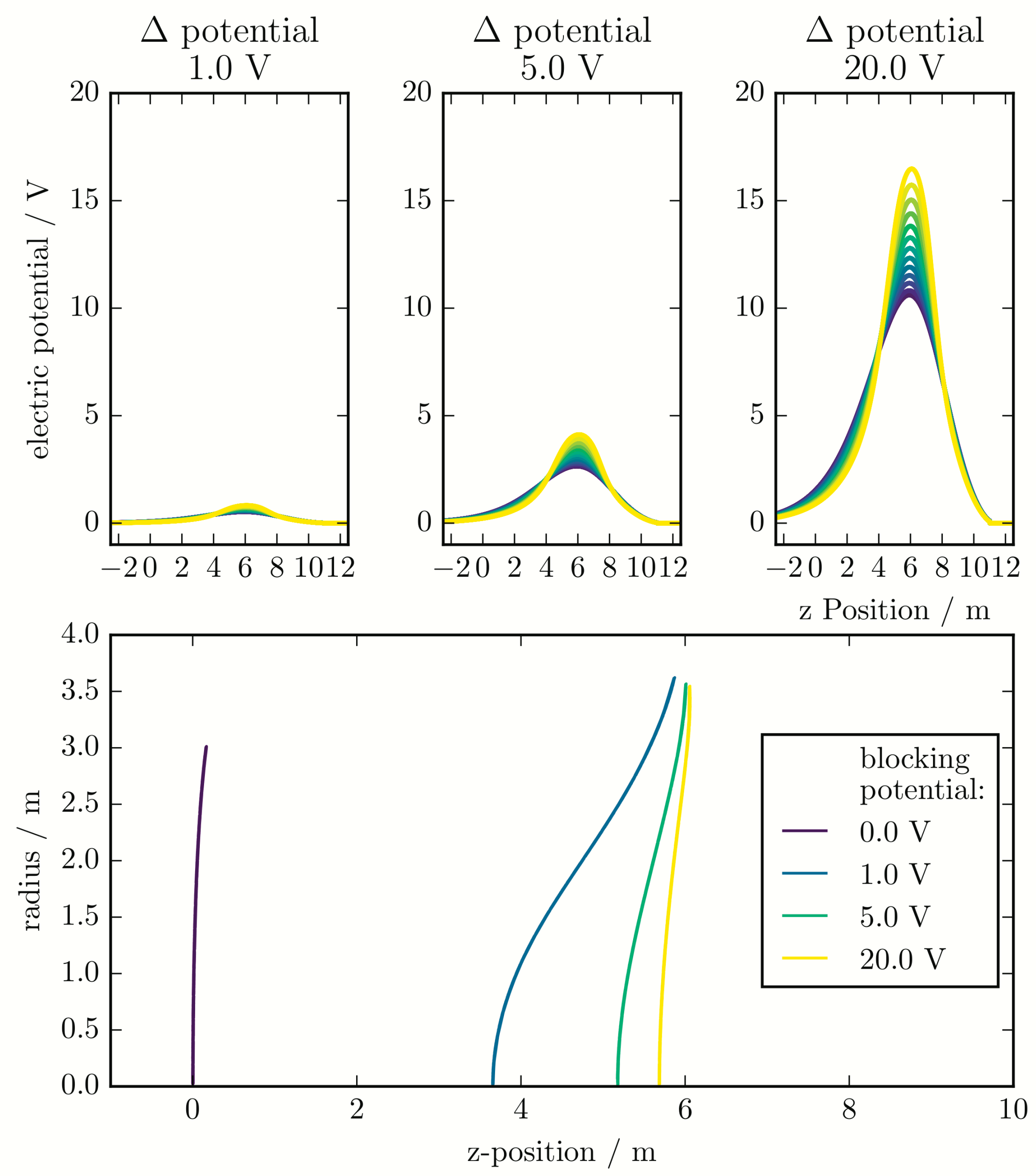

Figure 4.6: Potential penetration for different blocking potentials and curvature of the analyzing plane. **Upper row:** From left to right the potential applied to the wire electrode rings 12 and 13 is increased. The resulting potential penetration is plotted for different radii of the magnetic field lines tracing to the outer edges of the FPD rings. Brighter colors indicate magnetic field lines with greater radius. **Lower plot:** For low blocking voltages the shape of the analyzing plane is deformed, but returns to a straight plane at $U_{\text{blocking}} = 20\,\text{V}$.

Table 4.5: Run numbers of the measurements with different blocking potentials.

$\Delta U_{\text{blocking}}$ / V	Measurement runs
0	24992, 25002, 25012, 25039, 25050, 25162
0,2	24997, 25003
0,3	25014, 25023, 25024, 25041, 25051, 25163
0,4	24996, 25004, 25025, 25042, 25052, 25164
0,7	24998, 25005, 25026, 25043, 25053, 25165
1,0	24995, 25006, 25017, 25027, 25044, 25054, 25166
1,5	24993, 25007, 25018, 25028, 25045, 25055, 25167
2,0	24999, 25008, 25019, 25029, 25046, 25056, 25168
2,5	24994, 25009, 25020, 25030, 25047, 25169
3,5	25000, 25010, 25021, 25031, 25048, 25170
5,0	25001, 25011, 25022, 25038, 25049, 25171, 25176
7.0	25015, 25172
10.0	25013, 25173
14.0	25016, 25174
20.0	25037, 25175

The measurement runs with different blocking potentials are denoted in table 4.5. Figure 4.7 shows a depiction of the background rate for the surveyed potential barriers [DEF$^+$15]. Blocking potentials up to 0.4 V show only a slight slope towards lower background rates. This region is below the spectrometer resolution (see equation 4.2). Additionally the measurement has been performed without active HV post regulation. This causes an HV ripple on the vessel potential with a peak-to-peak value of $\sim 1.4\,\mathrm{V}$ [Kra16]. These distortions cause fluctuations in the low electron energy regions, complicating statements on this region. Above 0.4 V the rate decreases by ca. 100 mcps before it reaches a constant level at a blocking potential of 7.0 V. In this area, the potential barrier becomes more prominent with each setting and less low energy electrons pass the analyzing plane. For blocking potentials above 7.0 V no more electrons from the source side can surpass the analyzing plane. The remaining background stems from electrons originating on the detector side of the analyzing plane and provides a constant rate of ~90 mcps.

The measurements indicate that mainly low energy background electrons are created in the spectrometer volume. Proceeding from this finding, section 4.3 presents a method to obtain the energy spectrum of the background.

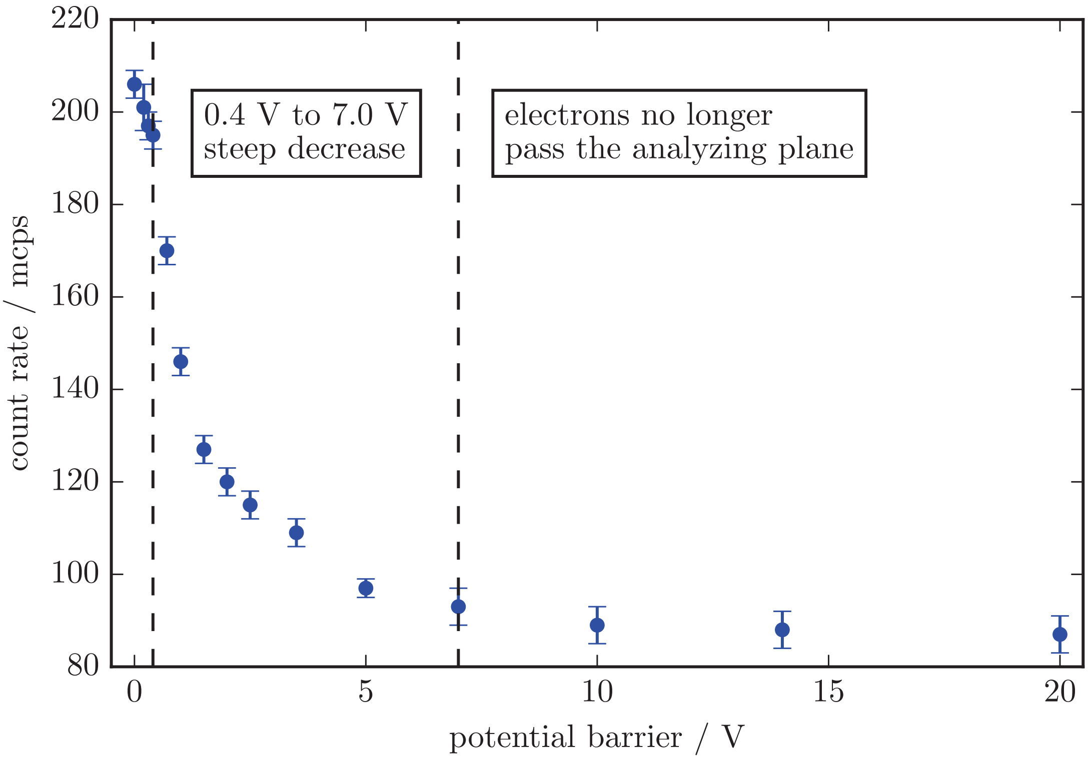

Figure 4.7: The background count rate at the FPD is measured for different blocking potentials.

4.3 Electron energy composition of the background

In this section a method to extract the kinetic energy composition of background electrons from measurements with different blocking potentials is discussed. For this purpose spectra of background electrons with fixed kinetic energies are simulated and fitted to the measurement, to recreate the experimentally observed background distribution.

At first the Kassiopeia simulation framework [FGT$^+$17] is used to calculate the electric potentials and magnetic fields belonging to a shifted analyzing plane with an optimized LFCS setting (table 4.4) and several blocking potential settings (table 4.5). These potentials and fields are then stored for later use in the simulation of background distributions. To accelerate the field calculations with Kassiopeia, the underlying spectrometer geometry is simplified to an axial symmetric representation.

For every blocking potential setting, 100 000 electrons are then created uniformly inside the spectrometer vessel. At the position of electron generation, the electrons have a set of initial starting parameters. These are spatial position (x_{start}, y_{start}, z_{start}), the electric potential U_{start} and magnetic field strength B_{start} at that position.

Due to the magnetic guidance, only electrons inside the flux tube, imaged on the FPD, need to be considered. By calculating the magnetic field line, that is connected to the outermost radius of the detector, a cut for the interesting electrons starting inside the flux tube can be applied, see figure 4.8. Electrons outside the flux tube cannot reach the detector and are discarded, thus avoiding unnecessary calculation time.

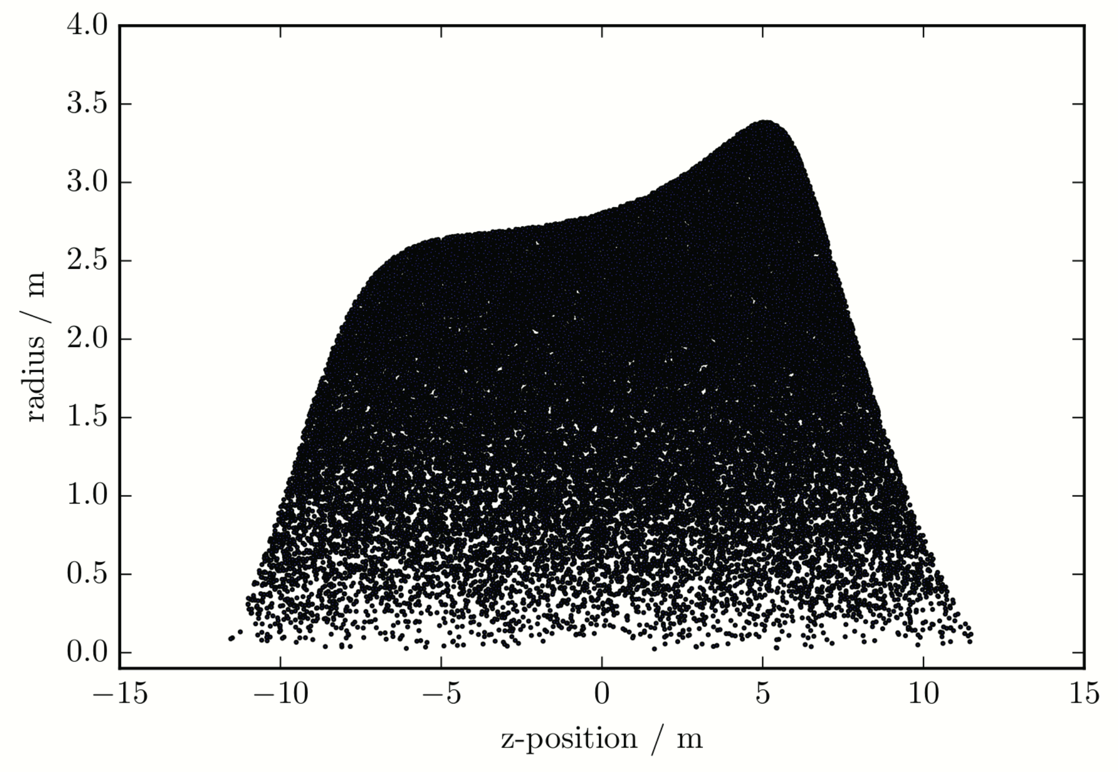

Figure 4.8: Starting positions of generated electrons. To achieve a meaningful statistic, 100 000 electrons are created uniformly inside the main spectrometer vessel. In order to reduce calculation efforts, all electrons which cannot reach the detector are excluded. This cut is defined by the magnetic field line, that traces back from the edge of the outermost detector ring to the spectrometer entrance.

In a second step, the Kassiopeia files for the different blocking potentials and generated electrons are handled by a python script. This script adds a fixed, but tunable, kinetic electron energy $E_{\mathrm{e,\,kin}}$ and a isotropically generated starting pitch angle $\theta_{\text{e, start}}$, between $0°$ and $90°$, to every previously simulated electron. This angular distribution is chosen, since only electrons moving towards the detector are considered as possible events. An additional and necessary modification to the flight direction will be presented during the discussion of the transmission conditions.

In order to reach the detector surface, the simulated electrons need to fulfill certain transmission conditions. Depending on the starting position, an electron has to overcome the potential barrier at the analyzing plane and may undergo magnetic reflection at the pinch magnet at the spectrometer exit. To define criteria for a successful transmission, equation 2.11, which states the transmission condition for electrons starting in the source, can be modified to adapt to the conditions at the analyzing plane and pinch for this simulation. Equation 4.4 describes the transmission condition for the pinch magnet:

$$E_{\text{e,kin,start}} \cdot \left(1 - \sin^2(\theta_{\text{start}}) \cdot \frac{B_{\text{pinch}}}{B_{\text{start}}}\right) + qU_{\text{start}} > 0\,. \tag{4.4}$$

Here $E_{\text{e,kin,start}}$ is the kinetic energy and θ_{start} denotes the pitch angle of the starting electron. $B_{\text{pinch}} = 6\,\mathrm{T}$ is the magnetic field strength of the pinch magnet and B_{start} the magnetic field strength at the point of electron generation. The modification of qU_{start} is necessary, because the electron starts at an elevated potential, which needs to be considered. A similar equation can be found for transmission through the analyzing plane:

$$E_{\text{e,kin,start}} \cdot \left(1 - \sin^2(\theta_{\text{start}}) \cdot \frac{B_{\text{analyze}}}{B_{\text{start}}}\right) + q\Delta U > 0\,. \tag{4.5}$$

As beforehand $E_{\text{e,kin,start}}$ represents the kinetic starting energy and θ_{start} the pitch angle of the electron. For the case of the analyzing plane, the magnetic field strength at the analyzing plane B_{analyze} needs to be known. B_{start} belongs to the initial parameters of the electrons and expresses the magnetic field strength at the point of electron generation. The potential difference $\Delta U = U_{\text{analyze}} - U_{\text{start}}$ describes the effective potential barrier as seen from the starting electron.

With these preconditions each simulated electron can be categorized into three different classes:

- An electron with a spatial position on the source side of the analyzing plane needs to fulfill the condition to pass the analyzing plane and the transmission condition at the pinch magnet to reach the detector.
- Is the electron generated on the detector side of the analyzing plane, the transmission condition is reduced to passing the pinch magnet at the spectrometer exit.

Table 4.6: Starting energies for simulated background electrons.

kinetic energy / eV												
0.1	0.4	0.7	1.0	1.5	2.0	2.5	3.0	3.5	4.0	5.0	6.0	7.0

- The third category is introduced, when allowing the electron, which is generated between analyzing plane and pinch magnet, to be guided towards the source side. This is implemented by considering an alternative start angle $\theta'_{\text{start}} = 180° - \theta_{\text{start}}$ of the electron. Is the electron then reflected at the analyzing plane (not fulfilling the transmission condition), but complies with the transmission conditions for the pinch, it can reach the detector surface.

From figure 4.7 it has been concluded that at blocking potentials higher than 7 V no background electrons from the source side of the analyzing plane appear to be transmitted. Therefore, for simulation and fit, we assume the energy distribution of the electrons to stay below 7 eV and simulate background contributions for the energies given in table 4.6. Since at the higher blocking potentials there is a remaining flux tube volume of ~50 m^3 in front of the detector an additional constant background is assumed.

For every electron the previous considerations are evaluated, based on its initial parameter set and this is repeated for every blocking potential and simulated kinetic electron energy. The resulting spectra of background rates as a function of blocking potential for a given start energy of the electrons are shown in figure 4.9.

The simulated background distributions allow a spectral fit to the measured count rates N_{data}. The energy spectrum of the real data is represented by a sum of the simulated count rates $N_{\text{sim}}(E_{\text{kin},i})$ and constant background N_{bg}, multiplied by appropriate weighting factors g_i and g_{bg}, respectively:

$$N_{\text{data}}(V) = \sum_i g_i(E_{\text{kin},i}) \cdot N_{\text{sim}}^{E_{\text{kin},i}}(V) + g_{\text{bg}} \cdot N_{\text{bg}} \,. \tag{4.6}$$

The factor g_i corresponds to the contribution of a certain electron energy to the measured data. To perform the fit, the python iminuit framework has been used.

Using all indicated energies (table 4.6) an energy spectrum as presented in figure 4.10 is obtained. For high blocking potentials, the large uncertainties of the weighting factors indicate an underdetermined system. Here the simulated spectra become less distinguishable and thus introduce increased uncertainties in the fit. The constant background has a magnitude of (35 ± 4) mcps and the overall fit has a reduced $\chi^2 = 2.54 \pm 1.41$. For energies between

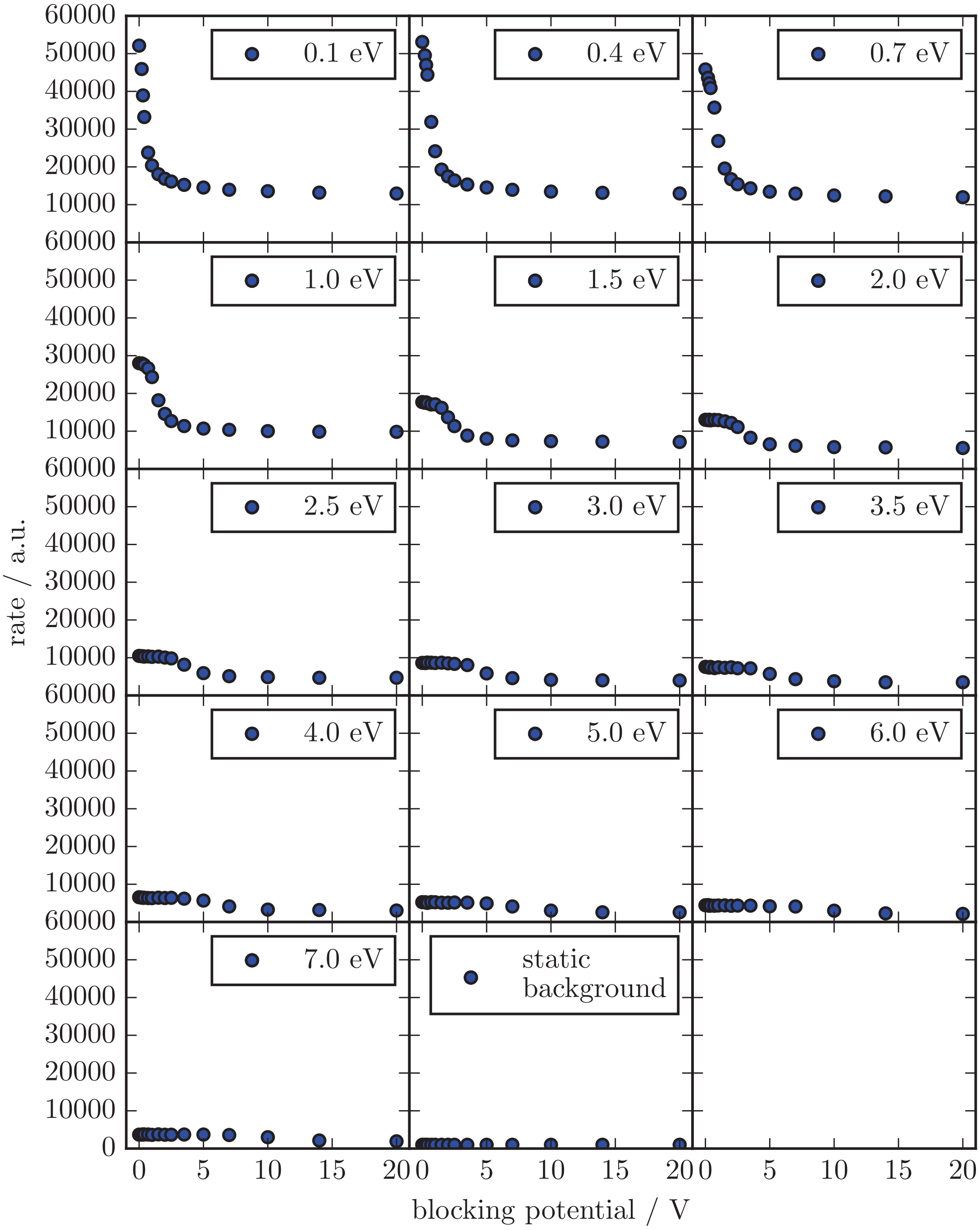

Figure 4.9: Simulated rates for certain electron energies and blocking potentials. The subplots show the rate evolution that would be seen by a detector for the electron energies given in table 4.6, including a static background. These spectra are weighted and summed during the fit, which calculates the most likely contributions of each spectrum to the measured count rate.

100 meV and 1 eV the fit shows a peak in amplitude (see figure 4.10, lower plot), which indicates that these electrons provide a significant contribution to the measured data . Between 2.5 eV and 3.5 eV the amplitude rise again, but the excess shows large uncertainties.

Decreasing the number of fit parameters by excluding 5 eV and 6 eV electrons, an improvement of the fit with an reduced $\chi^2 = 0.82 \pm 0.82$ is obtained. Figure 4.11 shows the resulting spectrum. The features beneath 1 eV and around 3.0 eV are preserved with comparable amplitudes. Likewise is the background stable at ca. (35 ± 4) mcps.

To investigate the characteristics of the amplitude peaks in the fit, two constraints have been introduced to parameters, which are highly anti-correlated. The amplitudes g_i of the spectra for 0.4 eV and 0.7 eV are constrained such, that $g_{0.4} = g_{0.7}/2$. Likewise have $g_{2.5}$ (for 2.5 eV) and $g_{3.0}$ (for 3.0 eV) been linked via $g_{2.5} = g_{3.0}/5$. These constraints have been chosen to preserve the relative height in amplitude from the unconstrained fit. The resulting fit is displayed in figure 4.12. Assuming this energy reconstruction, it leads to a contribution of electron energies from 400 meV to 700 meV of (38 ± 4) % and at 3.0 eV of ca. (40 ± 17) % to the complete spectrum.

In the context of the Rydberg hypothesis explaining the volume dependent background, the fitted energy spectrum is not fully expected. In the Rydberg hypothesis, excited hydrogen atoms, with high principle numbers n, propagate through the spectrometer and can be ionized by black body radiation from the vessel, forming a hydrogen ion and a low energy electron [Gal94] [Har15]. Highly excited Rydberg states with principle numbers $n_\mathrm{c} > 30$ [Har15] have flight paths long enough to be ionized in the flux tube volume. With rising principle numbers the energy needed to ionize the Rydberg atoms decreases. The resulting electron energy spectrum of ionized Rydberg atoms, caused by black body radiation at 293 K, rises towards lower electron energies and is discussed in [Tro18] [Glü15]. Therefore the vanishing contribution of 100 meV electrons, presented in the fit, is not expected.

The contribution of electrons with energies of ~3.0 eV are also not described by the hydrogen Rydberg model as the probability to obtain a 3 eV photon from the black body spectrum at the given temperature of the main spectrometer is negligible. This indicates a further background process. Alternative approaches, described in [Pol18], came up with a similar result. There electron spectroscopy is performed by electric trapping and with magnetic trapping. The electron energy distribution of the background favors electrons with kinetic energies in the order of $\mathcal{O}(100\,\mathrm{meV})$ complemented by energies up to 4.5 eV [Pol18]. The model deviates likewise from the hydrogen Rydberg hypothesis, but needs further investigation. A comprehensive statement re-

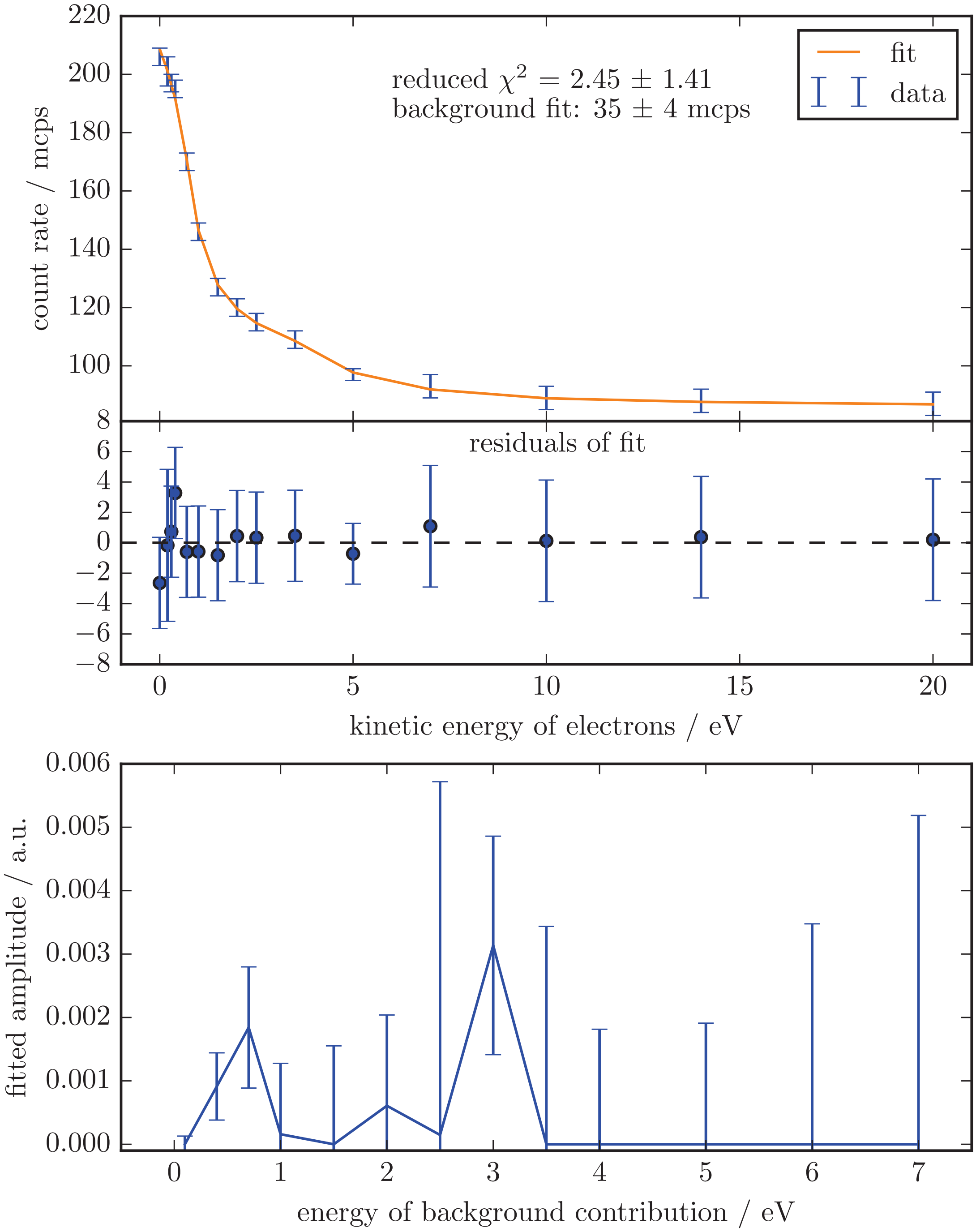

Figure 4.10: Top: Best fit to the measured data, considering all simulated energies (table 4.6) and a static background as free parameters. **Middle plot:** Residuals of the fit. In the region of highest energies the fit is underdetermined due to similar behaving energy spectra. **Lower plot:** The low energy region shows an amplitude excess favoring electrons of 400 meV and 700 meV. Around 3.0 eV is an indication for another energy contribution, although the uncertainties of the amplitudes are large.

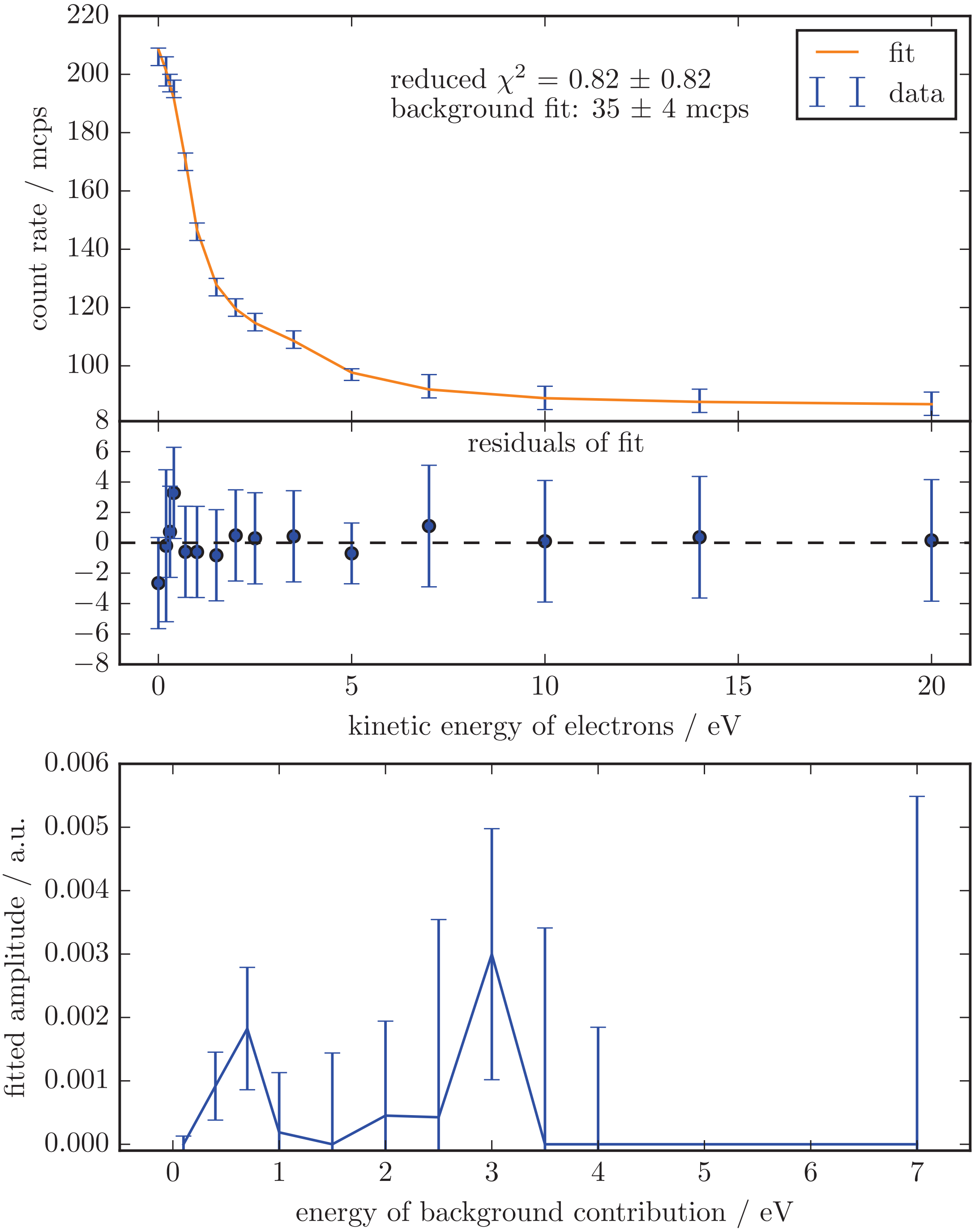

Figure 4.11: Fit with reduced number of contributing spectra. Due to the ambiguities in the high energy region, the fit is expected to improve by allowing less energies (5.0 eV and 6.0 eV removed). The resulting fit has an reduced $\chi^2 = 0.82 \pm 0.82$ and reproduces the data and all features in energy reconstruction as the previous fit.

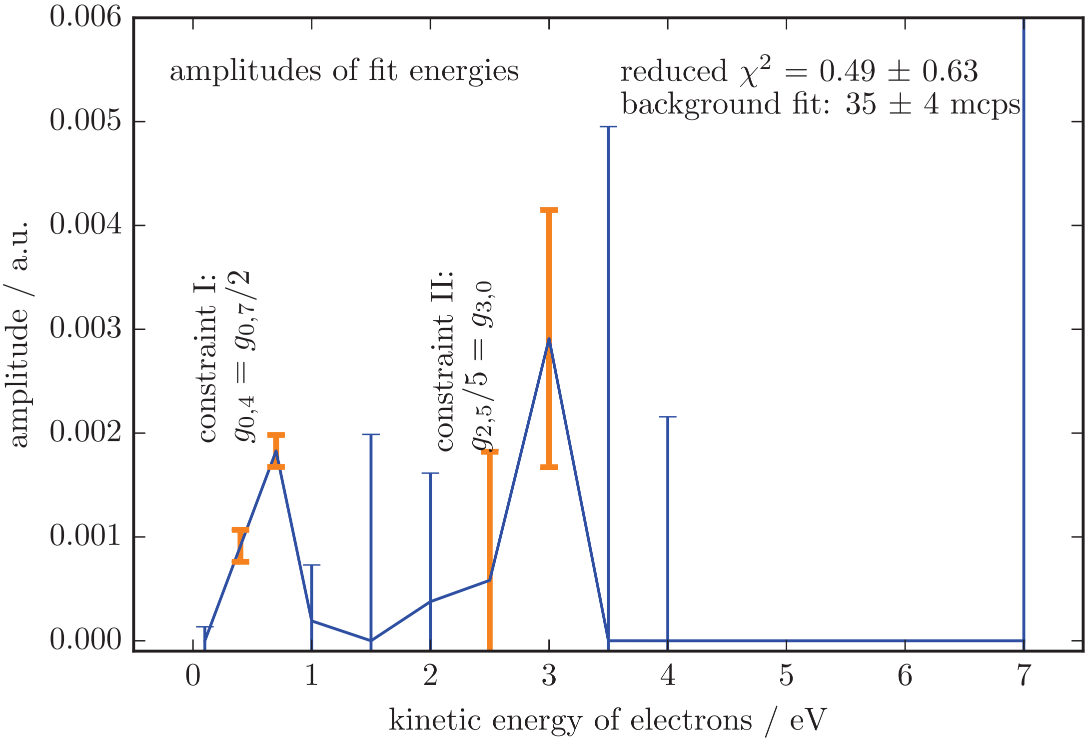

Figure 4.12: Constraining the amplitudes to investigate correlations. Introducing constraints to the fit, at the features at low and mid-range electron energy, enhances their correlation.

garding the overall nature of background processes in the main spectrometer is therefore not yet available.

The next section provides an outlook to the feasibility of tritium β-measurements with a shifted analyzing plane. Herein the transmission properties of this setting are investigated with an angular selective and monoenergetic electron source.

4.4 Feasibility for tritium measurement operation

The main spectrometer operated with a shifted analyzing plane, as described in section 4.1, could not only be used for electron energy spectroscopy, but can be considered as a possible tritium β-measurement mode. The introduced settings for LFCS and inner electrode for the detector side shifted analyzing plane lead to a strong decrease in the volume depending background. On the other hand the shifted analyzing plane exhibits larger inhomogeneities in the electric potential and magnetic field, that lead to a broadening of the transmission function, that needs to be investigated.

To examine the transmission properties of the spectrometer with shifted analyzing plane, analytic transmission functions have been calculated using Kassiopeia [FGT+17] and its module PeaBerry [Beh16] and have been compared to measurements. For such an calculation it has to be considered, that the distortion of field and potential along the detector radius cannot be neglected.

In the standard case, the transmission function is given by equation 2.13. It depends on a single retarding potential U_{ana} and magnetic field strength B_{ana} at the anaylzing plane. To incorporate the occurring inhomogeneities not a single transmission function is calculated for a given detector ring, but a normalized sum over ten functions, which are obtained by radially dividing every detector ring into ten evenly spaced subrings. The necessary parameters U_{ana} and B_{ana} are calculated with the Kassiopeia framework. With the ten parameter sets for a single FPD ring, the transmission function for this ring can be determined with PeaBerry.

The PeaBerry module has been written for the monoenergetic and angular selective electron source (e-gun) [Beh16] [Zac14], that has been used to investigate the transmission properties of the main spectrometer during the SDS II commissioning phase in 2015. Therefore the transmission functions calculated with PeaBerry depend on the backplate angle α_{p} of the e-gun. The backplate angle can be translated to a well-defined pitch angle ϑ_{PS2} inside the PS2 magnet. Their connection is expressed by the empirically found equation [Beh16]:

$$\vartheta_{\mathrm{PS2}} = 1° \cdot \arcsin\left(4.04 \cdot \frac{\alpha_{\mathrm{p}}}{1°}\right) + 3.7° \,. \tag{4.7}$$

In figure 4.13 the analytical transmission functions for different detector rings from bullseye to outer radii are plotted for an e-gun backplate angle of $\alpha_{\mathrm{p}} = 0$. Here the transmission probability is plotted against the potential difference

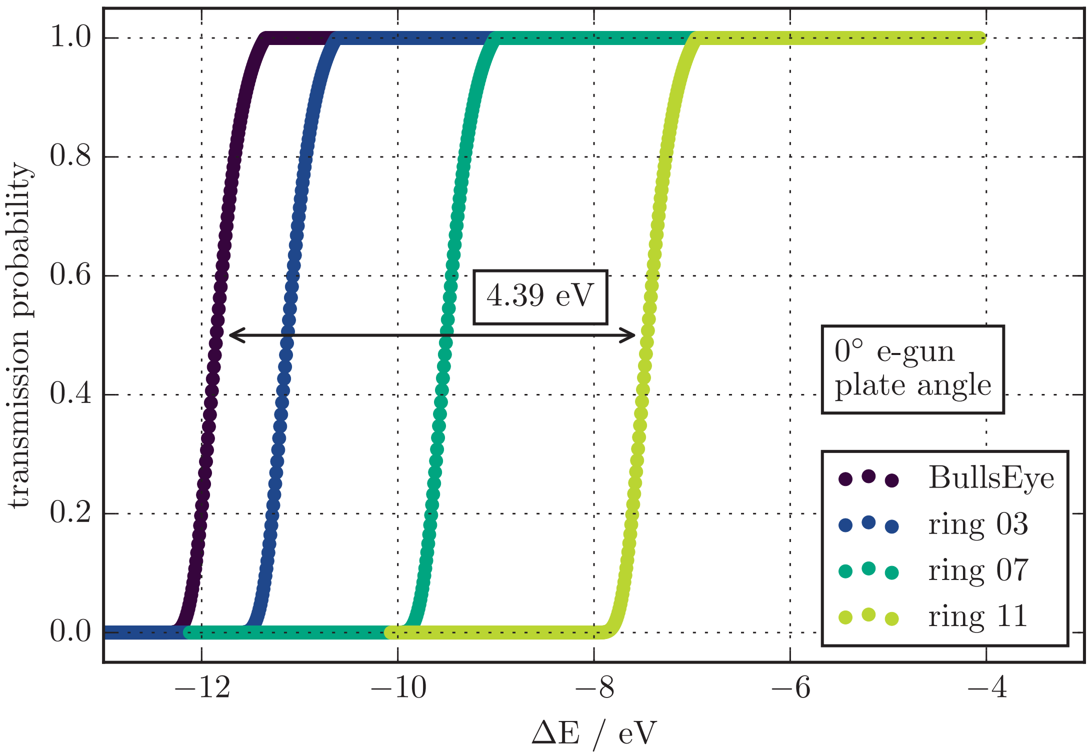

Figure 4.13: Calculated transmission function for different FPD pixels. The simulation is performed for electrons originating from the angular selective, monoenergetic electron source [Beh16]. The plot presents a simulated electron transmission probability of the spectrometer with a shifted analyzing plane at the detector side. Herein the electrons start with a backplate angle of 0° and along different magnetic field lines onto the denoted pixels.

between the spectrometer U_{spec}, to be more precise the potential of the inner wire electrode at the analyzing plane, and the electron source potential U_{start}:

$$E_{\text{surplus}} = q\Delta U = q(U_{\text{start}} - U_{\text{spec}})\,. \tag{4.8}$$

Due to the potential inhomogeneities, caused by the non standard field settings, the transmission functions are shifted by $U_{\text{ana}} - U_{\text{spec}}$, where U_{ana} corresponds to the analyzing plane potential calculated for the selected detector ring. From the figure it can be seen, that electrons starting on magnetic field lines with larger radii need more energy to surpass the analyzing plane. Hence the analyzing potential in the center of the spectrometer is smaller than near the wire electrode. This is caused by the potential penetration of the ground electrode at the exit of the spectrometer.

For the energy filtering only the longitudinal energy component $E_{||} = E \cdot \cos^2(\vartheta)$ of the electron is relevant and therefore the transmission probability

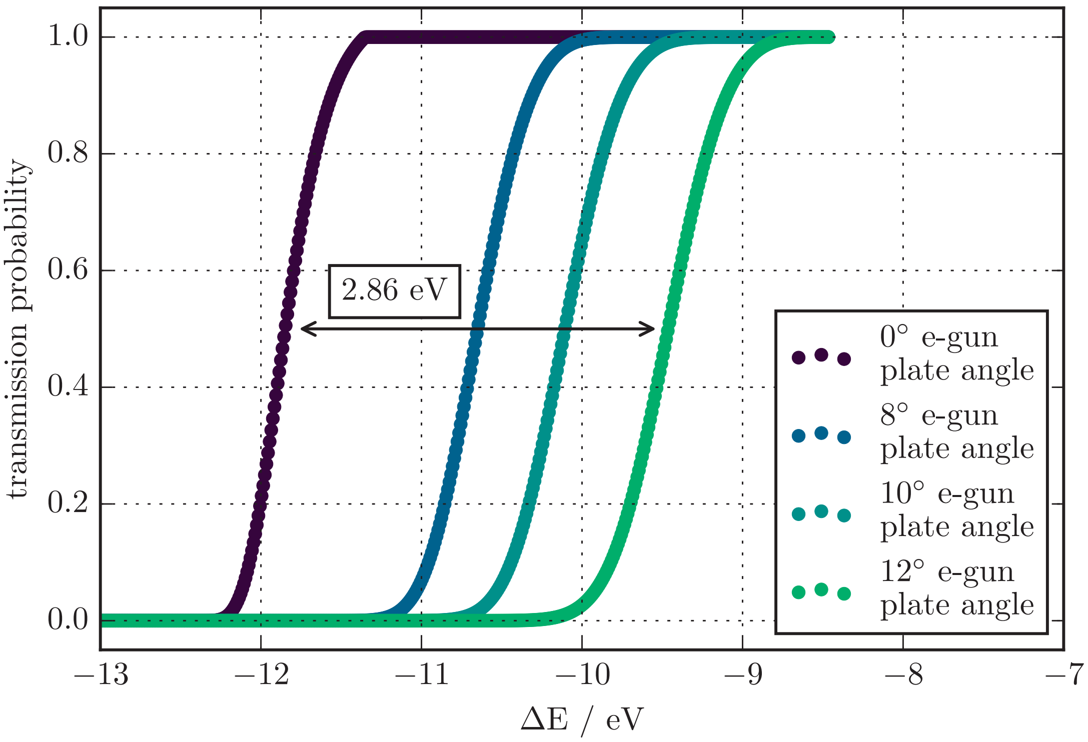

Figure 4.14: Analytically calculated transmission functions for varying e-gun backplate angles. The displayed transmission functions were calculated for the bullseye of the FPD detector. The shift of the transmissions functions due to increasing backplate angles is clearly visible.

depends on the pitch angle. Hence higher backplate angles cause a shift in the transmission function to higher energies (see figure 4.14).

The range from 0° to 12° for e-gun backplate angles is chosen to make use of the complete angular range up to the angle where magnetic reflection at the pinch magnet sets in. Calculating $\vartheta_{\text{cut-off}} = \arcsin(\sqrt{B_{\text{PS2}}/B_{\text{pinch}}}) = 60°$, for the spectrometer settings $B_{\text{PS2}} = 4.5\,\text{T}$ and $B_{\text{pinch}} = 6.0\,\text{T}$, and inserting $\vartheta_{\text{cut-off}}$ in equation 4.7 leads to a maximal backplate angle of 11.8°. The resulting shift of the transmission function measured with fixed angles of the e-gun corresponds to a broadening of the transmission function for an isotropically emitting source to 2.86 eV. This corresponds to a decline in spectrometer resolution by a factor of 3 compared to the design value.

During the SDS II measurement campaign it has been possible to characterize the shifted analyzing plane setting with the monoenergetic and angular selective electron source [Beh16] to verify the simulated results. The e-gun was positioned at the main spectrometer entrance at the source side, so electrons accelerated by the device could propagate through the spectrometer and hit

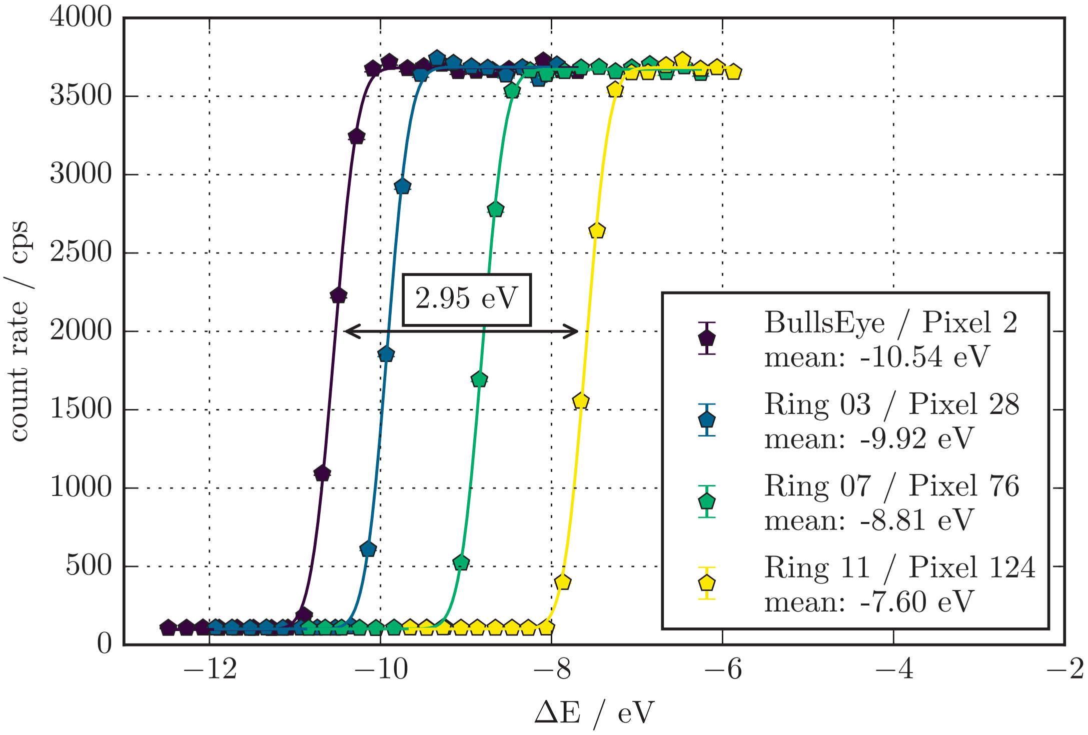

Figure 4.15: Measurement of the transmission function with the e-gun at zero pitch angle for different radii, corresponding to different pixel rings on the FPD.

the detector. In runs #23051-23505 and #23507 the analyzing plane situated at the detector side flat cone of the main spectrometer has been investigated. The transmission function has been examined only for four pixel rings at increasing radii, due to measurement time constraints. Hereby the pitch angle was set to zero, to solely investigate the radial dependence of the transmission function. Additionally the broadening of the transmission function, caused by electrons with increased pitch angle, was investigated for bullseye pixel #2.

Figure 4.15 shows the shift of the measured transmission function for the bullseye, ring 3, ring 7 and ring 11. Here the increase in energy needed for transmission towards the outer rings, follows the analytically calculated trend. But in contrast to the theoretical prediction (shift of 4.39 eV) the overall measured spread is only 2.95 eV. This indicates, that the assumed theoretical model needs further considerations to reproduce the measurement. Spatial inhomogeneities of the magnetic fields, e.g. introduced by misalignments in the LFCS coils , or distortions in the alignment of the spectrometer and detector are not fully implemented in the transmission function calculation.

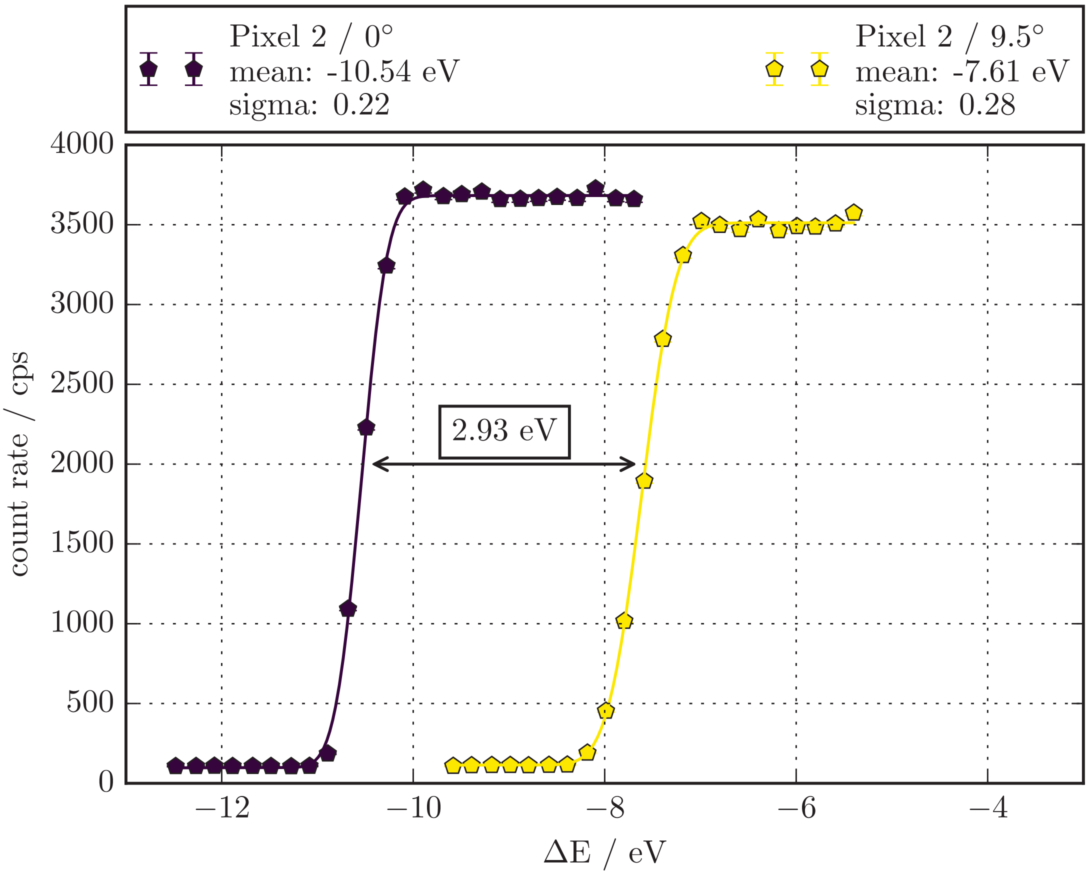

Figure 4.16: Electron transmission in e-gun measurements for different pitch angles. To understand the angular dependence of the electron transmission, the e-gun was prepared to point onto a central detector pixel. Afterwards the pitch angle has been increased until the count rate started to decrease due to magnetic reflection.

Since the e-gun is angular selective and not isotropically emitting, measurements for different electron pitch angles can be performed. This feature allows to investigate the broadening of the transmission function, which needs to be known precisely for a possible tritium β-measurement mode. Therefore the e-gun plate angle has been set to 0° (run #23501) along the horizontal axis of the main spectrometer. Afterwards the e-gun plate angle α_p has been increased until the onset of magnetic reflection becomes visible. Above a plate angle of 9.5° (run #23507) the rate started to decrease for further increased angles. Figure 4.16 displays the spread of transmission function up to the maximal angle which has negligible transmission losses and minimal distortions.

While the observed energetic shift of 2.93 eV is compatible with the calculated value for reflection of 2.86 eV, the onset of the reduced transmission is 2.3° below the theoretically expected angle of 11.8°. Again this points to shortcomings in the simulation of the shifted analyzing plane measurements with the available Kassiopeia model. Since the analytic model is not sensitive to effects like early or late retardation a more detailed simulation is needed. In [Erh16] it is stated, that even small variations, $\mathcal{O}(5\,\mu\mathrm{T})$, in the magnetic field strength showed a significant impact on transmission properties.

Since the spectrometer is optimized for settings with an analyzing plane located in the center of the spectrometer, operation modes with a shifted analyzing plane need additional sophisticated measurements and analysis to gain a full understanding of this topic. This includes full radial and azimuthal characterizations of the analyzing plane to describe its actual shape. Furthermore an investigation for early or late retardation [Val09] is necessary to understand the electron filtering with this operation mode.

The benefits of operating the spectrometer in such a mode are, on the other hand, a greatly reduced experimental background in the sensitive region around the endpoint of the tritium β-spectrum.

Chapter 5

Set-up and commissioning of the condensed Krypton source (CKrS)

Krypton sources provide the basis for a variety of investigations and calibration tools used in the KATRIN experiment. $^{83\mathrm{m}}$Kr acts as a natural standard due to its monoenergetic conversion electrons, originating from several atomic shells. These electrons possess well-defined energies, which can be used to calibrate the spectrometer voltage to the desired level of precision (less than $3\,\mathrm{ppm}$). Furthermore $^{83\mathrm{m}}$Kr emits electrons isotropically, thus allowing to study the broadening of the transmission functions of the spectrometer section due to the incident angular distribution. In addition to calibration and characterization, the krypton sources in the KATRIN infrastructure can be used to perform high precision spectroscopy to verify and enhance our knowledge of the atomic processes in this system.

At the KATRIN experiment three types of krypton sources will be used:

- implanted sources (^{83}Rb implanted in HOPG)
- gaseous $^{83\mathrm{m}}$Kr sources
- condendsed $^{83\mathrm{m}}$Kr sources.

The first kind is used at the monitor spectrometer, the former Mainz spectrometer. For this source ^{83}Rb gets implanted into a graphite crystal where the daughter isotope, the radioactive isomer $^{83\mathrm{m}}$Kr, will mostly decay in the graphite. Only the conversion electrons can leave the crystal structure. Due to the bound nuclei, the emitted electrons undergo scattering processes and therefore lose part of their energy, causing smeared out lines and line shifts. However a solid state source is localized in space and allows for a convenient handling, which makes it easy to integrate into a system like the monitor spectrometer.

A gaseous krypton source has the advantage of minimal scattering with a trade-off in handling. Such a source was used for test measurements with the WGTS during the Krypton measurement campaign in 2017. A defined amount of gaseous ^{83m}Kr, emanating from a ^{83}Rb generator, was injected into the WGTS beam tube to study electron transport and source characteristics. Nevertheless, the gaseous krypton source cannot be used on a regular basis, because it needs complete adjustments of the WGTS working parameters. Moreover the gas is distributed over the whole flux tube and emits electrons over the whole flux tube. This prohibits measurements of single detector pixels.

The alternative to the previous sources is the quench **C**ondensed **K**rypton **S**ource (CKrS). The initial CKrS concept was applied by Picard at the Mainz Neutrino Experiment [P$^+$92b] and renewed for the KATRIN experiment by B. Ostrick [Ost08]. The underlying concept of this source uses ^{83m}Kr adsorbed on a substrate, which is cooled to $\sim 25\,\mathrm{K}$ by a cryocooler. The gaseous Krypton is provided by an external ^{83}Rb generator connected through a valve and a thin capillary. Together with a suitable filter (Millipore [HAA$^+$11]), contamination of the KATRIN experiment by the long lived mother isotope is unlikely. To avoid condensing of residual gas, the substrate is situated in an ultra-high vacuum chamber surrounded by a cold shield, which acts as a cold trap. For the use at KATRIN the purity and precise control of thickness of the condensed Krypton film is mandatory, because the conversion electron line position and width is directly depending on these properties. Therefore high precision laser ellipsometry is used to monitor the film properties. In [Ost08] the reproducibility of film preparations and long-term stability measurements are demonstrated. Furthermore in [Bau13] a novel ellipsometry method has been developed, which suits the constraints present at the CKrS set-up in the beamline of the CPS at KATRIN.

In the following sections an introduction to conversion electrons and advantages of ^{83m}Kr as source material is given. Beyond that, a detailed overview of the crucial components of the condensed Krypton source and the implementation into KATRIN's infrastructure is shown. Finally the performance and first measurements during the Krypton campaign in July 2017 will be discussed.

5.1 Internal conversion

An excited nucleus can either deexcite by emission of a γ or, in a competing process, an orbital electron. The latter is called internal conversion and was described by O. von Baeyer, O. Hahn and L. Meitner [vBH10] [HM24] [Mei24]. In that case, the excited nucleus interacts electromagnetically with a shell electron that is subsequently emitted. These so-called conversion electrons are quasi-monoenergetic and obtain their kinetic energy E_{kin} depending on the atomic binding energy $E_{\text{b}}^{\text{vac}}$ and the gamma energy of the transition,

$$E_{\text{kin}} = E_{\gamma} - E_{\text{b}}^{\text{vac}} \text{ (nuclear recoil neglected).} \tag{5.1}$$

During the process it is possible that additional electrons of higher shells are excited and possibly emitted (shake-up and shake-off processes). These electrons obtain lower energies, but are also monoenergetic.

Since γ and electron emission compete, a conversion coefficient α_{IC} is defined by the ratio of both processes,

$$\alpha_{\text{IC}} = \frac{T_{\text{e}}}{T_{\gamma}}\,, \tag{5.2}$$

wherein T_{e} denotes the electron emission probability and T_{γ} the same for γ emission. This coefficient depends on the charge of the decaying nucleus, the orbital of the emitted electron, its energy, multipolarity and parity of the transition.

The corresponding electron line has a natural line width given by the uncertainty relation $\Gamma \cdot \tau = \hbar$ and can be described by:

$$\Gamma = \frac{\hbar}{\tau_{\text{e}}} + \frac{\hbar}{\tau_{\gamma}}\,. \tag{5.3}$$

Here Γ is the full width half maximum (FWHM) of the line and τ_{e} / τ_{γ} are lifetimes of the electron hole and the nuclear transition. The line shape can be expressed with a Lorentzian distribution:

$$L(E,E_0,\Gamma,A) = A \cdot \frac{{}^{\Gamma}\!/_{2}}{(E - E_0)^2 + ({}^{\Gamma}\!/_{2})^2} \tag{5.4}$$

A describes the amplitude of the distribution, E_0 the central energy (peak position), E the energy and Γ represents the FWHM [Zbo11].

5.2 $^{83\mathrm{m}}$Kr as conversion electron source

Concerning the KATRIN design for tritium β-spectrum measurements, a calibration source should match the key requirements of the experiment. In this case an electron source with the following characteristics is desirable:

- The energy of the emitted electrons should be near the tritium β-spectrum endpoint.
- A narrow natural line width for sharp transmission function measurements to investigate possible inhomogeneities in the retarding potential.
- The mother isotope should have a sufficient half-life to provide stable activity throughout a measurement campaign.

Sources using conversion electrons of $^{83\mathrm{m}}$Kr grant these properties [Z$^+$13].

The metastable $^{83\mathrm{m}}$Kr is generated through electron capture of ^{83}Rb (see figure 5.1). With a half-life $T_{1/2}$ of 82.6 d rubidium ensures sufficient longterm activity to endure several months. The branching ratio of the metastable state $I^\pi = \frac{1}{2}^-$ of the krypton isomer is 77.6 % and this state decays with a half-life of 1.83 h to an intermediate state with $I^\pi = \frac{1}{2}^+$. The process is highly converted, with a coefficient $\alpha_\mathrm{IC} = 2035$, and a transition energy, known by γ spectroscopy, of

$$E_{32} = 32\,151.7(5)\,\mathrm{eV} \;\; \text{[VD}^+\text{06]}\,. \tag{5.5}$$

After an additional half-life of 147 ns the ground state $I^\pi = \frac{9}{2}^+$ is reached (figure 5.1) by a second transition with a γ energy of

$$E_{9.4} = 9405.8(3)\,\mathrm{eV} \;\; \text{[Sle15]} \tag{5.6}$$

and a conversion coefficient of $\alpha_\mathrm{IC} = 17$ [R$^+$78a]. Internal conversion processes involving electrons of the K,L,M and N shells of $^{83\mathrm{m}}$Kr lead to a variety of monoenergetic electron lines. They obtain energies between 7 keV and 32 keV, which have been investigated in γ spectroscopy measurements. In [VGH$^+$76] and [WAH$^+$57] the intensities of occurring γ transitions are given. All lines of interest are listed in table 5.1.

In case of a gaseous source the conversion electron energy measured with a MAC-E filter can be written as [Zbo11]

$$E_\mathrm{kin}^\mathrm{gas}(i) = E_\gamma + E_{\mathrm{rec},\gamma} - E_\mathrm{rec,e}(i) - E_\mathrm{bin}^\mathrm{vac}(\mathrm{gas},i) - (\Phi_\mathrm{spec} - \Phi_\mathrm{source}) - C\,, \tag{5.7}$$

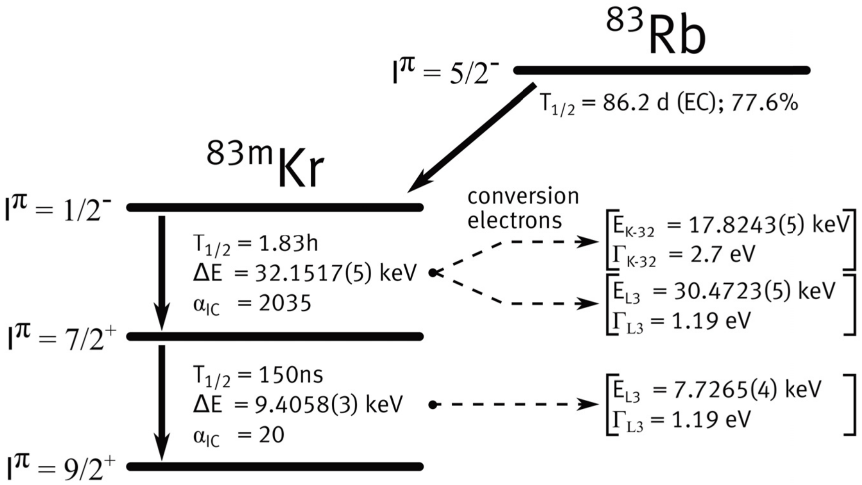

Figure 5.1: Decay scheme of ^{83}Rb and its daughter nucleus $^{83\mathrm{m}}$Kr. ^{83}Rb decays with a half-life of 86.2 d into the metastable $^{83\mathrm{m}}$Kr isomer. Through emission of gammas or monoenergetic conversion electrons $^{83\mathrm{m}}$Kr reaches the ground state via an intermediate step.

with:

E_γ : energy of the γ
$E_{\mathrm{rec},\gamma}$: recoil energy of the nucleus after γ emission
$E_{\mathrm{rec,e}}(i)$: recoil energy after electron emission from of shell i
$E^{\mathrm{vac}}_{\mathrm{bin}}(\mathrm{gas},i)$: electron binding energy, from shell i w. r. t. the vacuum level
Φ_{spec} : effective workfunction of the spectrometer
Φ_{source} : workfunction of the source
C : correction term for additional effects in a gaseous source

For a condensed source additional terms have to be included for a description. These are work function of the HOPG substrate, mirror charge effects with distance dependencies and surface terms which qualify the influence of residual gases on top of the substrate. A good estimation is given in [Ost08] and a new model for the CKrS within the KATRIN experiment will be provided in [Ful19].

In later measurements during the tritium β-spectroscopy the K_{32} conversion line is ideal. With a kinetic energy of 17.824 keV the electrons originating from the K-shell only differ by ca. 0.8 keV from the tritium endpoint energy.

Table 5.1: Summary of conversion electron lines of $^{83\mathrm{m}}$Kr, adapted from [Bau13]. The energies of M1 and E3 γ-transitions are stated in [VD$^+$06] [Sle13], the corresponding intensities per ^{83}Rb decay are based on [VGH$^+$76] [WAH$^+$57]. The denoted kinetic electron energies refer to gaseous krypton (equ. 5.7) for $\phi_{\mathrm{spec}} = \phi_{\mathrm{source}}$, with binding energies from [Zbo11]. Interpolated internal conversion coefficients [R$^+$78a] [R$^+$78b] allow determination of electron lines per ^{83}Rb decay. The experimental line widths are obtained from measurements with the former condensed $^{83\mathrm{m}}$Kr source at the Mainz MAC-E filter.
(**a**) no recommended values stated in [Cam01].
(**b**) natural line width fixed to 0 in the analysis [Bau13].
(**c**) the lines N_2 and N_3-32 were analyzed as a single line $N_{2/3}$-32 [Bau13].

Electron level and notation		**Atom rec. energy $E_{\mathrm{rec},\,e}(i)$**	**Kinetic energy $E^{\mathrm{gas}}_{\mathrm{kin}}(i)$**	**Intensity $I(i)$ [%] per ^{83}Rb decay**	**Lorentzian line width $\Gamma(i)$**			**Instr. resol. ΔE**
					recomm. [Cam01]	**exp. (cond. Kr) [P$^+$92a]**	**[Ost08]**	
γ transition M1			9 405.8(4)	5.86(134)				
$2s_{1/2}$	L_1	0.05	7 481.2(9)	70.32	3.75	5.30(4)	3.72(19)	0.4
$2p_{1/2}$	L_2	0.05	7 673.8(4)	7.91	1.25	1.84(5)	1.29(14)	0.4
$2p_{3/2}$	L_3	0.05	7 726.5(4)	5.07	1.19	1.40(2)	1.58(16)	0.4
$3s_{1/2}$	M_1	0.06	9 113.0(5)	11.60	3.5	4.27(5)	3.123(4)	0.5
$3p_{1/2}$	M_2	0.06	9 183.5(4)	1.30	1.6	1.99(32)	0.63(39)	0.5
$3p_{3/2}$	M_3	0.06	9 191.3(4)	0.98	1.1	1.66(8)	1.1(4)	0.5
$4s_{1/2}$	N_1	0.06	9 378.2(4)	1.43	0.4	0.19(4)	0.288(93)	0.5
$4p_{1/2}$	N_2	0.06	9 391.1(4)	0.12	0.03 [a]	–	0 [b]	0.5
$4p_{3/2}$	N_3	0.06	9 391.7(4)	0.09	0.03 [a]	–	0 [b]	0.5
γ transition E3			32 151.7(5)	0.035 8(45)				
$1s_{1/2}$	K	0.12	17 824.3(5)	17.07	2.71	2.83(12)	2.70(6)	0.9
$2s_{1/2}$	L_1	0.20	30 226.9(9)	1.13	3.75	–	–	1.6
$2p_{1/2}$	L_2	0.20	30 419.6(5)	17.61	1.25	1.84(5)	1.165(69)	1.6
$2p_{3/2}$	L_3	0.21	30 472.3(5)	27.42	1.19	1.40(2)	1.108(13)	1.6
$3s_{1/2}$	M_1	0.21	31 858.8(6)	0.19	3.5	–	–	1.6
$3p_{1/2}$	M_2	0.21	31 929.3(5)	2.99	1.6	1.99(32)	1.230(61)	1.6
$3p_{3/2}$	M_3	0.21	31 937.0(5)	4.65	1.1	1.66(8)	1.322(18)	1.6
$3d_{1/2}$	M_4	0.21	32 056.5(5)	4.69	0.07	–	–	1.7
$3d_{3/2}$	M_5	0.21	32 057.7(5)	6.59	0.072	–	–	1.7
$4s_{1/2}$	N_1	0.21	32 124.0(5)	0.02	0.4	0.19(4)	0.4	1.7
$4p_{1/2}$	N_2	0.21	32 136.8(5)	0.27	0.03 [a]	0.59(4) [c]	0.608(13) [c]	1.7
$4p_{3/2}$	N_3	0.21	32 137.5(5)	0.41	0.03 [a]			1.7

5.3 Film monitoring by ellipsometry

As previously mentioned, a crucial parameter for reproducible electron line positions and widths is a thin, which means sub-monolayer, and ultra pure film of condensed $^{83\mathrm{m}}$Kr on top of either a pre-plated stable Kr film or directly on the HOPG substrate. To monitor the film growth with sufficient precision, laser ellipsometry is used. This is a commonly known technique in surface science and semiconductor industries. The measuring principle is the determination of changes in polarization of an incident light beam, reflected on a multilayer surface system. Therefore the laser beam has to be well prepared in terms of initial polarization. While there are several variants of ellipsometry methods, this work focuses only on null-ellipsometry. Herein the measured intensity of the reflected beam is minimized by adjusting optical elements in the light path and the remaining intensity is measured by a detector system, i.e. a photodiode. A circular polarized laser beam passes a linear **P**olarizer, followed by a quarter-wave-plate, the **C**ompensator, gets reflected on an optical **S**ystem and shines through an additional linear polarizer, which is called the **A**nalyzer. In figure 5.2 a sketch of the fundamental **PCSA** arrangement is shown. In the ordinary set-up polarizer and analyzer are mounted rotatable, while the compensator is set to a fixed angle. Due to spatial constraints in KATRIN's infrastructure an ellipsometry variant has been developed which uses a fixed analyzer and rotatable compensator [Bau13].

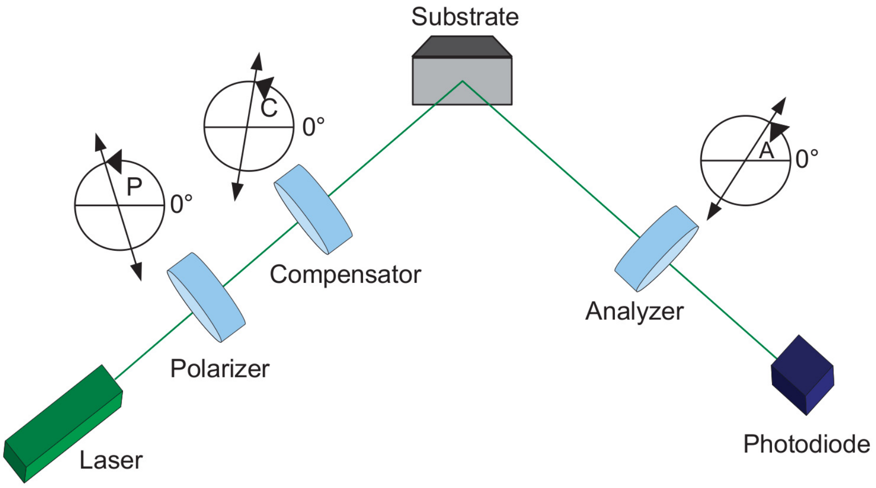

Figure 5.2: Schematic overview of an ellipsometry set-up. The initial prepared light beam passes through rotatable polarizer and compensator. At the substrate the beam is reflected and changes the polarization w. r. t. the multilayer surface properties. Subsequently, the reflected beam passes a rotatable analyzer and the remaining light intensity is measured with a photodiode.

5.3.1 PCSA ellipsometry

For a better understanding of the null-ellipsometry method used at the CKrS, the mathematical background will be discussed. Deeper insights of ellipsometry principles are given in [AB87] and especially for the newly developed variant in [BGS$^+$13].

A suitable way to describe an electromagnetic wave, which impinges on an optical system, is to split the electric field into a component parallel (p) and perpendicular (s) to the plane of incidence. For a wave propagating in z-direction through an isotropic medium, this can be written as:

$$\vec{E}(z,t) = E_s\hat{e}_s \cdot e^{i(\omega t - k_w z + \varphi_s)} + E_p\hat{e}_p \cdot e^{i(\omega t - k_w z + \varphi_p)} \,. \tag{5.8}$$

Here E_s and E_p denote the amplitudes of the wave, $\hat{e}_s$ and $\hat{e}_p$ the basis vectors and φ_s, respectively φ_p the phases. In case of two possible linear polarizations they will be labelled as s and p polarized. Looking at the CKrS, the system under study can be considered as a three layer system, consisting of the surrounding vacuum, the condensed krypton film and the underlying HOPG substrate. It is necessary to define Fresnel coefficients for every interface:

$$r_{ij,x} = \frac{N_j \cos\Phi_i - N_i \cos\Phi_j}{N_j \cos\Phi_i + N_i \cos\Phi_j} \,, \tag{5.9}$$

$$t_{ij,x} = \frac{2N_i \cos\Phi_i}{N_j \cos\Phi_i + N_i \cos\Phi_j} \,. \tag{5.10}$$

The indices i,j represent the different layers of the multi-layer system, as shown in figure 5.3, and x denotes the field components. N expresses the complex refraction index of the optical components and Φ depicts the angle between incident beam and surface normal.

Since the refraction index of vacuum is $N_0 = 1$ and the one of krypton is a real value, $N_1 = n_1 - ik_1 = n_1$, equations 5.9 and 5.10 can be simplified. Applying Snell‘s law,

$$N_i \sin\Phi_i = N_j \sin\Phi_j \,, \tag{5.11}$$

and noting the impossibility of measuring the angles Φ_1 and Φ_2, it can be written as:

$$\cos\Phi_1 = \sqrt{1 - \left(\frac{\sin\Phi_0}{n_1}\right)^2} \tag{5.12}$$

$$\cos\Phi_2 = \sqrt{1 - \left(\frac{\sin\Phi_0}{n_2}\right)^2} \,. \tag{5.13}$$

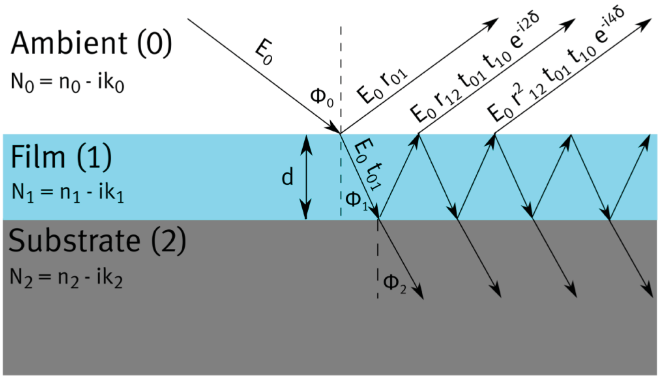

Figure 5.3: Refraction of an incident light beam on three layer system. The initial beam impinges on the condensed film and undergoes parts-wise reflection and transmission. The transmitted light undergoes further reflection and transmission at the interface between film and substrate.

This allows to express the phase change δ between the interfaces of condensed film and substrate, which includes the Krypton film thickness d and the wavelength λ of the used laser:

$$\delta = \frac{2\pi d}{\lambda}\sqrt{n_1^2 - \sin^2\Phi_0}\,. \tag{5.14}$$

To obtain the amplitude of the reflected wave of both polarisation states, all partial waves need to be added up. Considering further, that the Fresnel coefficients for reflection in opposite direction changes the sign and the transmitted partial wave is directly depending on the reflected one, an expression for the reflection amplitudes of p and s polarized light can be found (x represents the corresponding polarization state):

$$R_x = \frac{r_{01,x} + r_{12,x}e^{-2i\delta}}{1 + r_{01,x}r_{12,x}e^{-2i\delta}}\,. \tag{5.15}$$

The overall transmitted amplitude of the reflected beam can be expressed by an elliptic equation, which is given in [AB87]. This includes the elliptic angles Ψ and Δ, which are representations of the measurable angles of polarizer and compensator,

$$\rho_S = \frac{|R_p|}{|R_s|} = \tan\Psi e^{i\Delta}\,, \tag{5.16}$$

$$\tan\Psi = \frac{R_p}{R_s}\,, \tag{5.17}$$

$$\Delta = \Delta_p - \Delta_s\,. \tag{5.18}$$

$|R_p|$ and $|R_s|$ describe the absolute value and Δ_p and Δ_s are the complex phases of the reflection amplitudes.

In the general case of PCSA-ellipsometry the intensity I, which can be measured for example with a photo diode, is given by [AB87]:

$$\begin{aligned} I \propto &|R_p \cos(A) \left[\cos(C)\cos(P-C) + i\sin(C)\sin(P-C)\right]| \\ &+ R_s \sin(A) \left[\sin(C)\cos(P-C) + i\cos(C)\sin(P-C)\right]|^2 . \end{aligned} \tag{5.19}$$

P, C and A represent the angles of their optical components, Polarizer, Compensator and Analyzer.

5.3.2 Null-ellipsometry with fixed analyzer

As noted in the beginning, the CKrS relies on null-ellipsometry and therefore vanishing intensity at the photo diode in measurements. This leads to simplifications in previous formulas allowing to express the optical multilayer system through:

$$\rho_s = \frac{R_p}{R_s} = -\tan(A)\frac{\tan(C) - i\tan(P-C)}{1 + i\tan(C)\tan(P-C)} . \tag{5.20}$$

In this set-up, the polarizer and compensator are mounted on rotatable holders allowing their angles to be set to minimize the measured intensity. Due to spacial and environmental constraints the analyzer has to be integrated with a fixed angle. The small space inside of the KATRIN beam tube and the necessity of moving the substrate region to cover the complete flux tube and the cryogenic regime forbid a remotely operated motor inside the vacuum vessel. To cope with these challenges, [BGS$^+$13] and [Spi11] shows that the intended ellipsometry variant is feasible.

5.3.3 Ellipsometry set-up with mirrors

In figure 5.4 the laser beam is shown as it passes the optical components. The laser light is prepared by an additional linear polarizer and quarter-wave plate to ensure well-defined circularly polarized light before it enters the ellipsometry set-up. Three dielectric mirrors are used in the path of light to point it onto the substrate-film-system. These need to be polarization conserving, such that the measurements are not distorted. [Pet15] describes the behavior of suitable dielectric mirrors that have been tested in the described ellipsometry set-up.

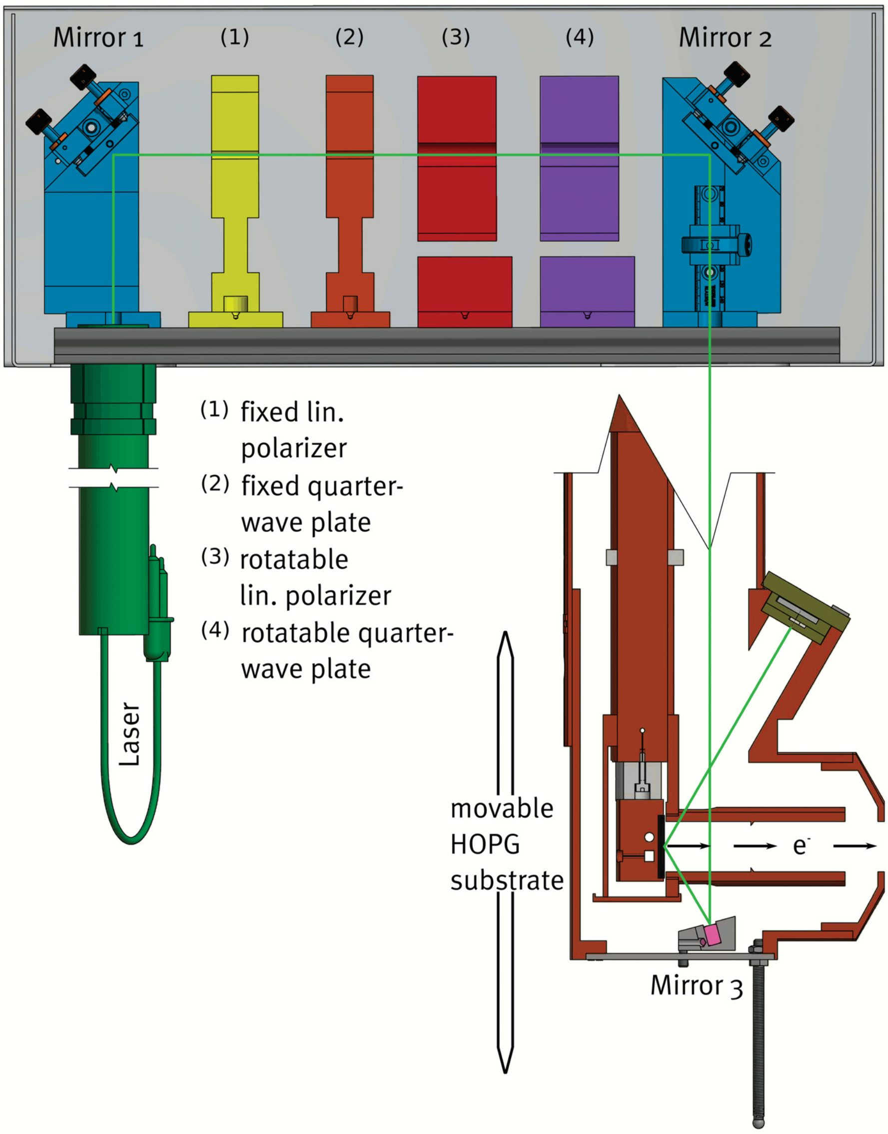

Figure 5.4: Ellipsometry set-up in the CKrS. The light, originating from a laser, $\lambda = 543\,\mathrm{nm}$, $P = 0.5\,\mathrm{mW}$ (green), is guided via a dielectric mirror (blue) through the polarization defining optical components. These are a fixed linear polarizer (1) and quarter wave plate (2) to generate circular polarized light. Afterwards the rotatable polarizer (3) and compensator (4) of the ellipsometry set-up are mounted. A second mirror (blue) reflects the laser beam into the CKrS vacuum vessel, down to the substrate region. Here a third mirror (pink) directs the light onto the HOPG substrate and film system (black) where it gets reflected and changes its polarization due to reflections within the frozen gas layer. The reflected light shines through the analyzer (beige) before it is detected and the intensity measured with a photodiode (grey).

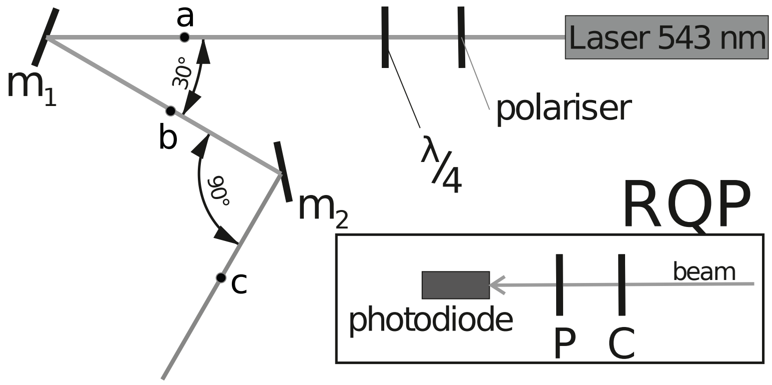

Figure 5.5: Polarization conservation measurements. This set-up allows to measure the state of polarization of a previously prepared laser beam. Points a, b and c denote the measurement positions with RQP. The photodiode signal is read out with a LabView controlled 12 bit ADC. The mirrors ($\mathrm{m}_{1,2}$) represent the ones built into the CKrS.

For this measurements the light of the laser ($\lambda = 543\,\mathrm{nm}$, $P = 0.5\,\mathrm{mW}$, Thorlabs Model no. HGP005-1) is circularly polarized by a polarizer[1] and compensator[2]. After that the beam polarization is quantified with a Rotating Quarterwave Stokes Polarimeter (RQP). This measurement is then repeated after the 15° mirror[3] and the 45° mirror[4] is introduced into the light path (the angles denote reflection angle for which the mirrors are optimized). It could be shown that the procured mirrors indeed preserve polarization and are therefore suitable for use inside the CKrS [Pet15].

The complete system was tested at room temperature [Hös16] in Münster, performing a scan over the full angular ranges of polarizer and compensator (see figure 5.6, left) and the full functionality could be demonstrated. During the 2017 krypton campaign the room temperature HOPG scan has been repeated [Fed19] and the earlier results have been successfully reproduced. The measured intensity profile is consistent with [Bau13] and with simulations based on equation 5.19 (see figure 5.6, right).

Prior to the Krypton measurement campaign in 2017 an ellipsometry measurement with stable krypton gas has been performed. Here the gas has been gradually condensed onto the substrate thus increasing the film thickness. As expected from [BGS$^+$13] the changing polarizer and compensator

---

[1] PGT 2.05 Bernhard Halle Nachfolger GmbH - optische Werkstaetten

[2] CVI Melles Griot QWPM-543-04-4-R10

[3] Laseroptik, custom made, batch no. 01041Wi1

[4] Laseroptik, conventional, model no. L-00217

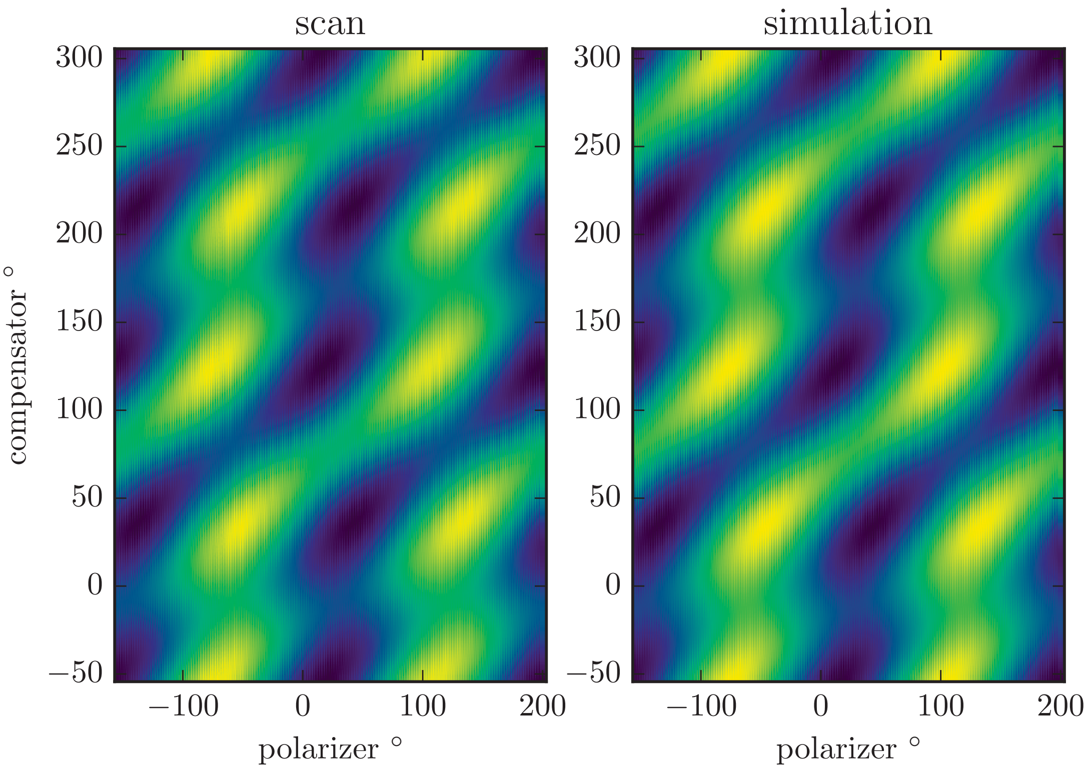

Figure 5.6: Experimental scan and simulation of the light intensity distribution reflected from a dry HOPG substrate. Both plots show a light intensity profile for polarizer and compensator angles varying over 2π. On the left the intensity is measured with the complete CKrS ellipsometry system at room temperature and the HOPG without krypton film. The right-hand side plot displays a simulated profile (equation 5.19) for a HOPG substrate under the same conditions Both are consistent and do not show unpredicted features in the intensity distribution.

coordinates, belonging to the intensity minimum traced in the measurement, follow an elliptic pattern, shown in figure 5.7. Detailed ellipsometry measurements taken during the Krypton campaign will be discussed in the thesis of M. Fedkevych [Fed19].

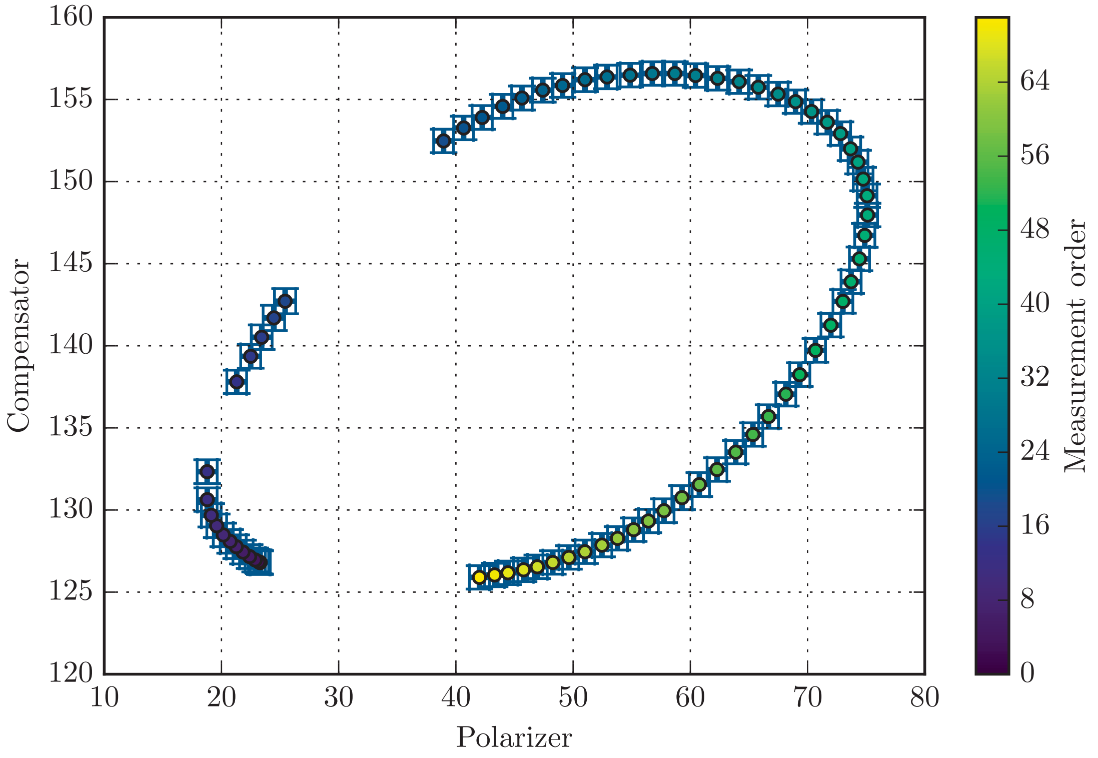

Figure 5.7: Ellipsometry measurement with stable krypton. Gradually condensed krypton on the HOPG substrate changes the polarization of the reflected laser beam. Thus the angles of polarizer P and compensator C have continuously to be adjusted to follow the chosen intensity minimum with the increasing layer thickness. For a pure film, the angle pairs follow a periodic elliptic pattern, which enables a determination of the optical film parameters [Bau13].

5.4 Technical realization of the CKrS

The condensed krypton source of the KATRIN experiment provides sub-monolayer $^{83\mathrm{m}}$Kr films, which are spatially confined to a cooled HOPG substrate. Monitoring of the film properties, thickness and purity, is performed by laser ellipsometry, explained in the previous chapters. The technical requirements of KATRIN lead to a compact, but complex design of the source. The CKrS represents a calibration tool for investigations of spectrometer transmission properties and the high voltage stability.

Measurements with the source will take place during intermissions of the tritium β-spectroscopy. Hence the source must be moveable, to enter and leave the beam tube. At the installation site, port 2 of the CPS, this corresponds to a distance of ~1.3 m from parking position outside of the CPS to

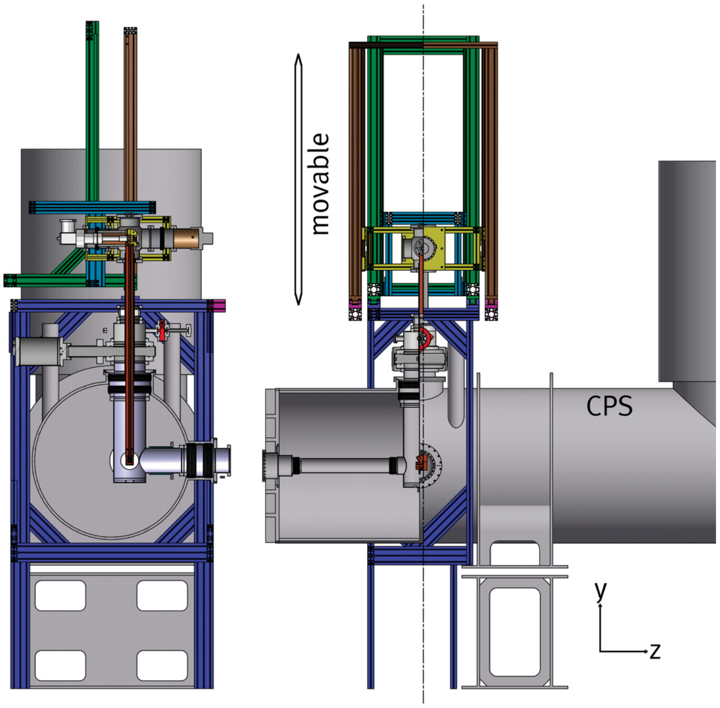

Figure 5.8: Technical drawing of the CKrS. The various components are color-coded for better differentiation. Blue support beams mount the main frame to ground and the platform inside the Tritium laboratory. In brown and green the tiltable stage is shown, which allows horizontal movement. For vertical movements the light blue and yellow carriage is used. There are two carriages to allow decoupling of the vacuum pumps and cryocooler from the optics and the coldfinger with HOPG substrate.
The left drawing shows the CKrS cross section along the beam tube, the right side represents a view from the side.

the flux tube center. The highly oriented pyrolytic graphite (HOPG) substrate with the condensed $^{83\mathrm{m}}$Kr film, covers an area of $2\,\mathrm{cm} \times 2\,\mathrm{cm}$. This active area is horizontally and vertically moveable through the flux tube, which allows spatially resolved characterization of the transmission properties of the spectrometers. In vertical direction, the positioning is performed by linear motion along guiding rails. For horizontal movement the complete upper part of the CKrS is tilted around a pivot point. This technique allows a full coverage of the flux tube through the spatially limited access port. In figure 5.8 a CAD drawing shows the CKrS scaffold.

The upper scaffold houses two carriages, which carry the upper vacuum chamber of the CKrS and the subsystems necessary for the operation. The first carriage supports the gas system, providing controllable flows of stable and radioactive krypton gas and the laser ellipsometry set-up for film monitoring.

The second carriage supports a cryocooler and a turbo molecular pump, which are decoupled from the vacuum chamber by bellows to reduce vibrational stress to the system. Both carriages and the vacuum chamber are electrically insulated to enable to apply an offset voltage. This allows to overcome the energy gap between the monoenergetic conversion electrons of $^{83\mathrm{m}}$Kr of $\sim 17.8\,\mathrm{keV}$ and the ca. $18.6\,\mathrm{keV}$ filter energy used for tritium β-measurements.

The $^{83\mathrm{m}}$Kr gas is obtained from a ^{83}Rb emanator, integrated in the gas system. Stable krypton gas is supplied from a non-magnetic $0.5\,\mathrm{l}$ gas bottle also mounted on the gas system. To freeze on stable Kr, a defined amount of gas is accumulated in a pressure monitored buffer volume. Through a tunable precision valve, the gas flow is fed into a heatable capillary inside the vacuum chamber. At the end of the capillary, a nozzle directs the gas onto the HOPG substrate.

In order to condense the gaseous krypton onto the HOPG, a cryocooler is coupled to the substrate. This cryocooler is able to cool down the substrate to $25\,\mathrm{K}$, which is sufficient to freeze on krypton atoms. To keep contaminations caused by residual gas, that also condenses on the substrate, at an acceptable level, the whole system needs to be kept under ultra-high vacuum. The desired pressure is on the order of $10^{-10}\,\mathrm{mbar}$ and is achieved by a cascaded pumping with a prevacuum pump and a TMP.

To perform reproducible measurements with the source, the frozen krypton film has to be renewed periodically. Cleaning the substrate is done via thermal heating of the HOPG substrate by Zener diodes and a $2\,\mathrm{W}$ ablation laser. For this purpose the source is retracted from the CPS into the so-called ablation chamber. Here the substrate faces a window, giving a free pathway for the ablation laser, to shine onto the HOPG. To cover the complete surface at once, the laser beam is widened by a diffuser, which allows depositing enough energy to evaporate $^{83\mathrm{m}}$Kr films as well as frozen residual gas.

The CKrS is controlled by LabView programs, managing the positioning, gas flow and readout of vital parameters. These parameters are temperatures of the cooled parts, like substrate, coldshields and gas capillary and the intensity of the ellipsometry signal on the photodiode. The LabView programs are executed on two National Instruments PXI machines, one for mechanical movement and one for parameter readout and control of the gas system. The latter can be set to higher potential inside a high voltage cabinet.

In picture 5.9 and 5.10 the actual construction can be seen. The wall in the background separates the Tritium Laboratory Karlsruhe (TLK) and the KATRIN spectrometer hall. Beneath the floor plating the CPS beam tube is placed, covered by the CKrS scaffold. The carriages and hence the substrate

Figure 5.9: CKrS set-up integrated in KATRIN beamline. The complete CKrS is situated on a platform, on top of the CPS. The left-hand side shows the high voltage cabinet, which houses the read-out electronics for ellipsometry, temperature monitoring and control of the gas system. On the right side, the upper CKrS scaffold is shown with the lowered carriages.

is lowered into the flux tube showing the CKrS in operation. Later on, a high voltage safety fence has been placed in front of the set up to reduce risks for operating personnel.

The following section 5.5 provides a detailed look on all major components of the CKrS, covering all important features needed for operation.

5.5 Subsystems

For a better description of the complete CKrS it can be divided into major components, which are (1) vacuum pumps, (2) cryogenic systems, (3) gas supply (4), substrate section (5) ellipsometry and ablation laser, (6) high voltage and (7) mechanical movement. The various subsystems and finally the complete CKrS set-up have been built and tested beforehand at the Institut für Kernphysik in Münster.

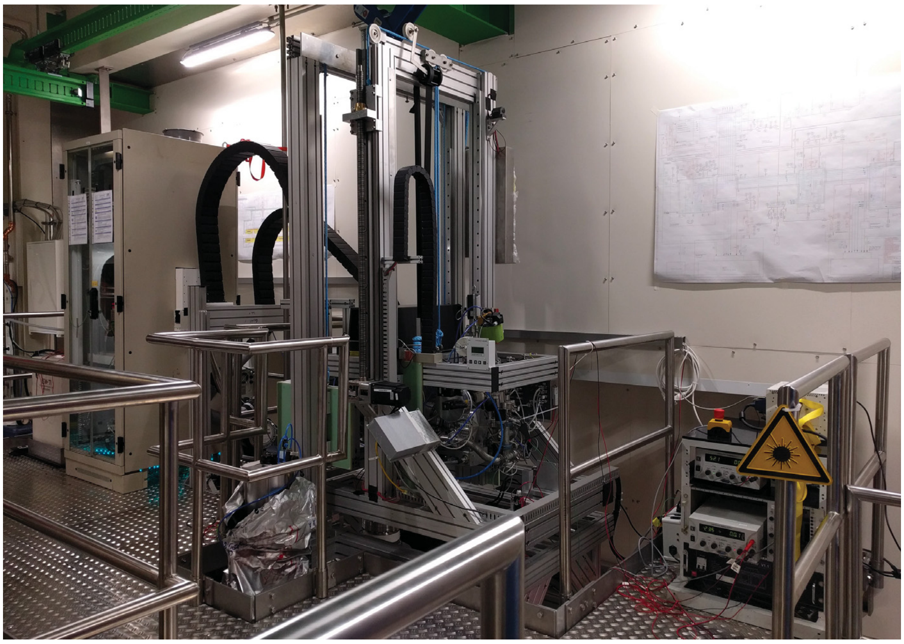

Figure 5.10: CKrS inside the tritium laboratory. The picture shows a detailed view onto the motor control system (right side) used for horizontal and vertical movement. On the lowered carriage the gas system can be seen

5.5.1 Vacuum system

To be integrated in the KATRIN experiment, the condensed krypton source needs to match the vacuum conditions of the beamline of approx $10^{-10}\,\mathrm{mbar}$. Thus the low temperature components of the CKrS (coldfinger, HOPG substrate, etc.) are contained within a vacuum chamber connected to the CPS by a bellow. Moreover ultra high vacuum is required to reduce freezing of residual gases to the substrate.

Evacuating this chamber is achieved by a turbo molecular pump, Leybold MAG W 400, together with an Adixen ACP 15 roots prevacuum pump by Pfeiffer Vacuum. Additionally a SAES getter pump, SORB-AC Cartride pump Mk 5, is integrated into the system, which further improves the vacuum conditions. The pressure is monitored by two gauges, an Oerlikon ITR 90, placed next to the TMP on top of the CKrS and a Pfeiffer, MPT-200, cold cathode vacuum gauge connected to the ablation chamber directly above the flange towards the CPS inlet valve. The Pfeiffer MPT-200 gauge is read out by the Siemens PCS7 control system, which can initiate an emergency extraction in case of failures in the vacuum system.

Within the schematic 5.11 the set-up of the main vacuum containment is displayed. It shows the connection of the pumps to the CKrS cryo- and

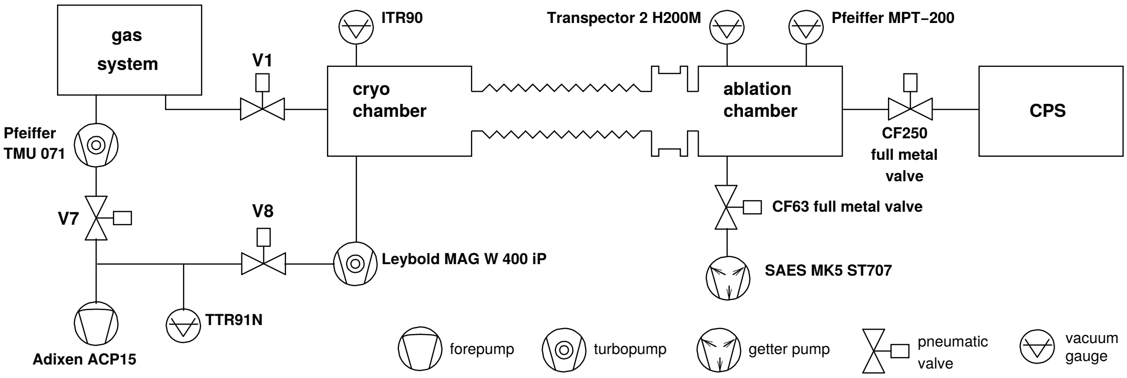

Figure 5.11: Schematic view of the vacuum containment. The TMP is mounted with bellows to the vacuum chamber, while the prevacuum pump is connected through another bellow. The getter pump is mounted onto the ablation chamber above the CPS.

ablation chamber and the gas system. By closing the CF250 full metal valve, the vacuum system of the CKrS can be separated from the CPS.

5.5.2 Cooling system

A cryocooler is needed to cool down the substrate so that krypton gas can condensate onto it. This can be achieved at temperatures below 30 K [Ost08]. For cooling a two staged Gifford McMahon-type cold head by Sumitomo Heavy Industries Ltd., model RDK 408D, is used, which provides a cooling power of 34 W at 40 K for the outer stage and 1 W at 4 K for the inner one. The cold head is coupled horizontally to the CKrS vacuum chamber via a 200 mm bellow at the movable carriage. The cooling stages are internally connected to the vertically mounted outer coldshield and the inner coldfinger using copper braids to decouple vibrations by the cold head operation. This is needed to not disturb the ellipsometry signal, while ensuring sufficient thermal conductivity. The coldshield and coldfinger reaches 1.5 m downwards to the substrate region. Here the HOPG substrate is mounted on a separate copper block (section 5.5.4), that is attached to the coldfinger with a stainless steel part reducing its thermal conductivity. Thus the substrate can be heated in order to remove frozen films without harming the cold head.

Monitoring of all temperatures within the CKrS is achieved with eight sensors made by Lakeshore, type Cernox CX 1050. These Cernox sensors are thin film resistance temperature sensors with a measurement range between 0.1 K to 420 K and a precision of $\pm 10\,\mathrm{mK}$ in the region of the cooled HOPG around 25 K [Cry17]. Two sensors are placed along the capillary on different positions

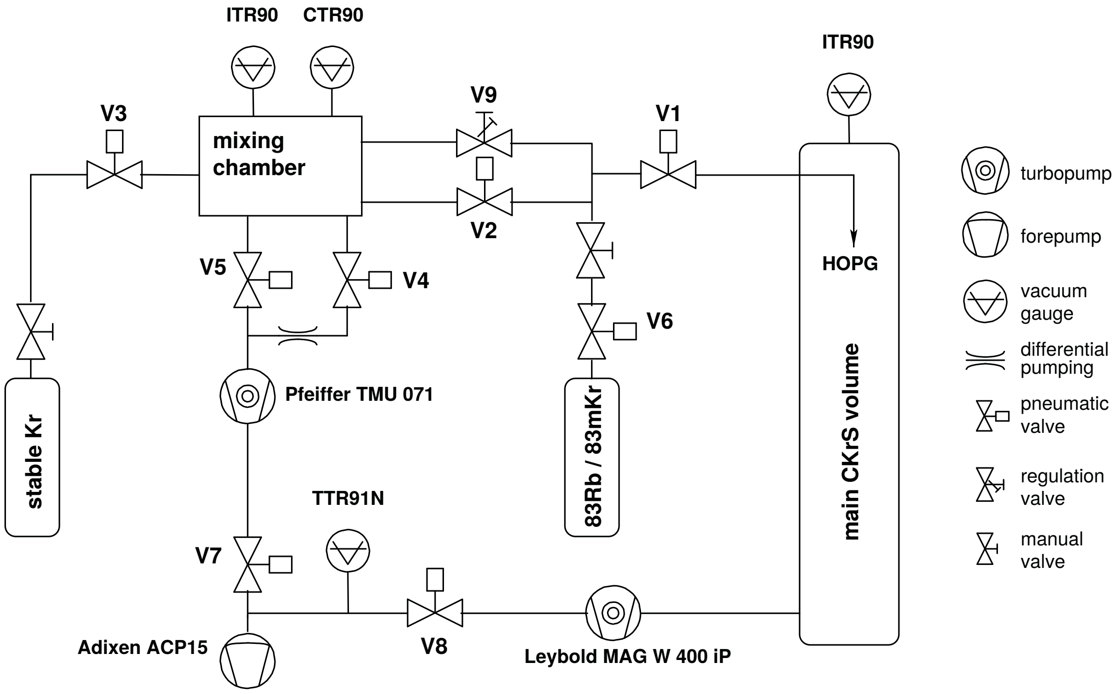

Figure 5.12: Flow diagram of gas system. The illustration shows an overview of the valves necessary to operate the CKrS gas system. Gas can be introduced into the system through a gas bottle (stable krypton) or from a ^{83}Rb generator, providing metastable $^{83\text{m}}$Kr gas. The mixing chamber allows to adjust the amount of stable krypton by controlling the pressure inside. To pump out residual gases or to evacuate the gas system, a cascaded TMP and prevacuum pump are connected.

and one on the nozzle directly at the gas outlet. Each coldshield and the dielectric mirror on the bottom of the outer coldshield are equipped with sensors. To guarantee a failsafe monitoring of the HOPG, the substrate is provided with two temperature sensors, mounted on the copper holder of the substrate.

5.5.3 Gas system

To provide the CKrS with stable or radioactive krypton isotopes, a sophisticated gas supply system is needed. Figure 5.12 displays the flow diagram for the gaseous krypton. It contains a ^{83}Rb generator, which serves as source for the gaseous $^{83\text{m}}$Kr. Furthermore a bottle with stable krypton gas is attached to the mixing chamber to prepare small amounts of gas via remote controlled valves.

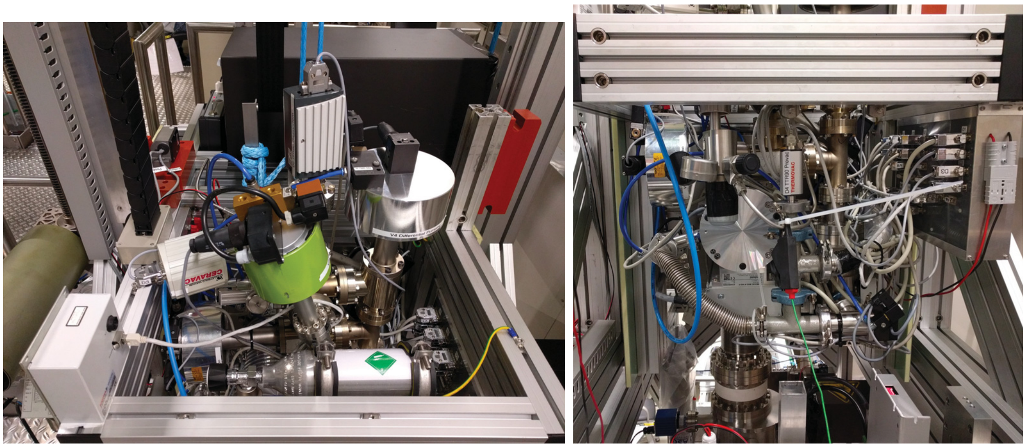

Figure 5.13: Gas system integrated into CKrS. Due to space constraints the gas system needed to be lightweight and compact. At its position it is still possible to maintain all valves, remote controls and the Kr gas bottle. The Rubidium generator (not visible in picture) had to be placed on the opposite side of the CKrS vacuum chamber.

In order to characterize the ellipsometry system, a defined inlet of gas into the CKrS is necessary. Therefore a precision valve (V9), Pfeiffer UDV 146 Ganzmetall-Regelventil, is installed between mixing chamber and inlet. To guarantee that only krypton gas enters the system, the gas system can be evacuated by a turbomolecular pump, model Pfeiffer TMU 071 P DN 63 CF. The mixing chamber is connected to the TMP through two valves, V4 and V5. V5 is directly connected to the TMP, whereas V4 has a differential pumping section to reduce gas load on the turbo pump. These gas loads occur while flushing the mixing chamber with stable krypton in preparation of a measurement to calibrate the ellipsometry system with stable Kr gas. In this case, stable krypton with a pressure of ca. 10 mbar, measured with a Leybold Ionivac ITR 90 and CERAVAC CTR 90, is repeatedly flushed into the mixing chamber through V3 and afterwards pumped out. Additionally the TMP revolution speed is set to 50% of its nominal value, to reduce stress on the internal rotors. Once the system is prepared for operation with stable gas, V1 at the CKrS inlet gets opened and an ellipsometry measurement can be started with the expert PC, which monitors the amount of krypton in the mixing chamber. During the measurement the precision valve V9 is opened for a defined time, causing the gaseous krypton to propagate to the substrate where the gas condenses.

To measure with $^{83\mathrm{m}}$Kr the piping between CKrS inlet and the volume of the rubidium source needs to be evacuated through V2. Afterwards valves V2 and V9 get closed and V6 and V1 are opened, so that radioactive krypton gas can only diffuse towards the substrate.

5.5.4 Substrate section

An important part of the condensed krypton source is the substrate region. Here the gaseous krypton is frozen onto the cold HOPG substrate. Moreover, the analyzer and photodiode of the ellipsometry system are integrated in the coldshield. Zener diodes for heating the substrate are placed behind the HOPG and most of the temperature sensors to monitor the properties are placed in this region.

The substrate is a highly oriented pyrolytic graphite (HOPG) crystal, which is a regular stacked crystal with a hexagonal oriented graphite plane lattice (figure 5.14). Within the plane, the spacing between the carbon atoms is 1.42 Å and in perpendicular direction 3.35 Å. Among the planes only the Van der Waals force binds the crystal and therefore single layers can simply be stripped off. For cleaning purposes, prior to the installation, this was done with adhesive tape. Since the HOPG is not monolithic, the surface normal of the single crystals have non-zero angles w. r. t. the axis perpendicular to the plane. This property is classified as mosaic spread, defined as the Full Width at Half Maximum of the rocking curve[5]. HOPG substrates with angles of $0.4° \pm 0.1°$ are of highest quality.

This layer structure of the HOPG causes a varying thermal conductivity along the plane and along the perpendicular axis, which depends on the substrate temperature [I+83] [Tay66]. For substrate temperatures above 100 K this leads to a constant heat conduction in plane with a negligible fraction passing into the material. Therefore initially heating the substrate with Zener diodes and then ablating the surface with a high power laser, as described in section 5.5.5, is very efficient.

At the CKrS a $20\,\mathrm{mm} \times 20\,\mathrm{mm}$ substrate by Optigraph, model AGraphZ (ZyA /flat/mosaic spread $0.4° \pm 0.1°$) is glued with electrically conductive epoxy, Polytec EC 101, onto the substrate holder (see figure 5.15). This allows to electrically elevate the potential of the HOPG.

The substrate holder is a copper part designed to attach the HOPG and to ensure the alignment w. r. t. the overall CKrS set-up. The holder has a quadratic bore hole for two temperature sensors and a round recess for two Zener diodes. Heating can be performed with two separate controllable 5 W Zener diodes by Surmetic, model 15N3, each connected to a Tenma 72-2535 power supply. Operation up to 25 V and 500 mA is possible and reproducible without causing damage to the diodes, which achieves substrate temperatures of 120 K, when the coldhead is running.

---

[5] Rocking curve are the result of measurements used to determine the broadening of the diffraction peaks, caused by misorientation of crystallites.

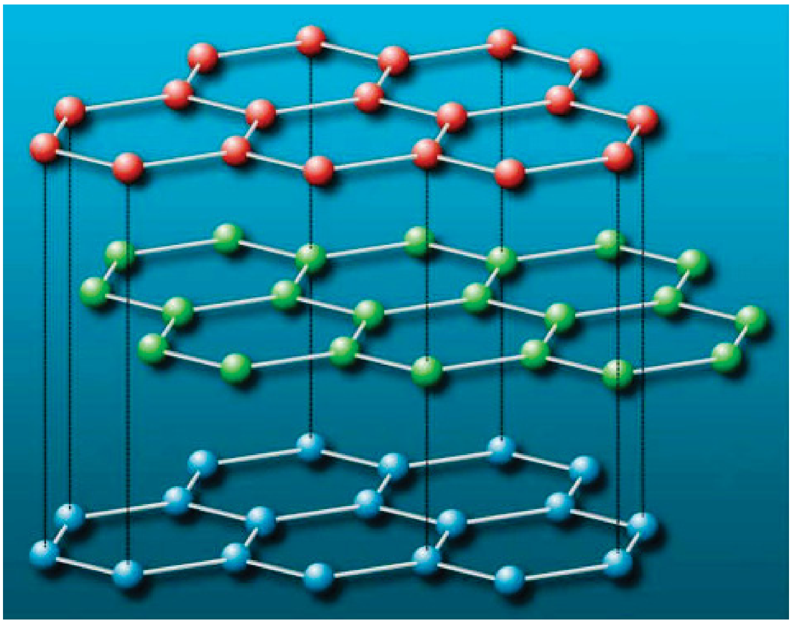

Figure 5.14: HOPG crystal structure scheme. Within a plain, the carbon atoms form a regular hexagonal patter, whereas between layers the binding is due to Van der Waals force. Neighboring atoms are at a distance of 1.42 Å in the honeycomb and 3.35 Å from plain to plain [Ost08].

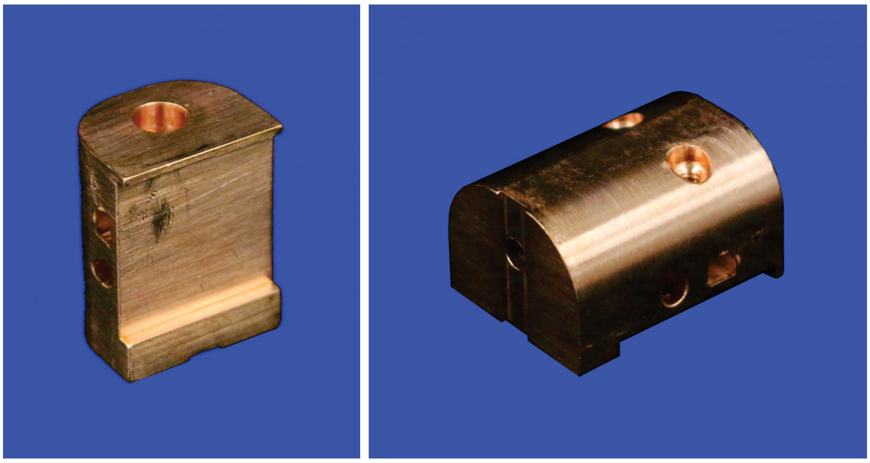

Figure 5.15: Substrate holder without HOPG. The substrate holder is designed to allow a proper attachment of the HOPG substrate. It has a recess to fit with the cold finger only in an aligned position. The boreholes are designed to host two temperature sensors and two Zener diodes for heating.

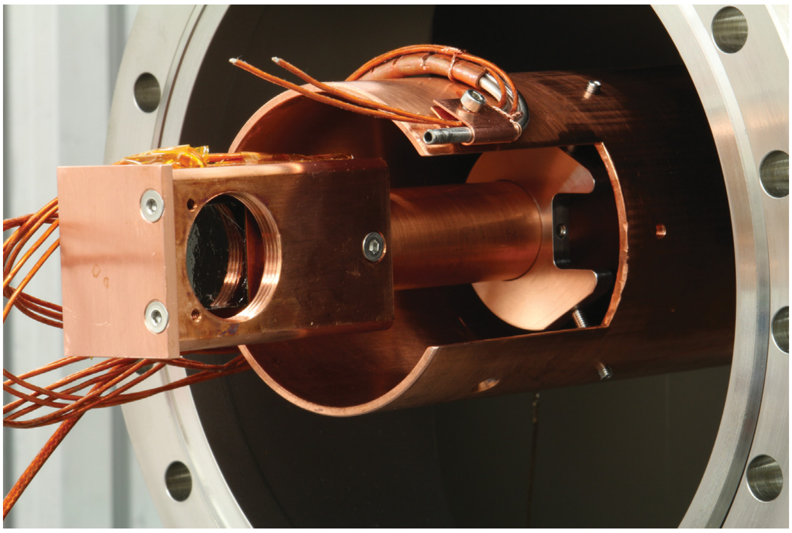

Figure 5.16: Substrate with mounted inner coldshield. The HOPG is surrounded with a copper coldshield, which is used as a cold trap for residual gases. Furthermore the opening of the inner coldshield contains a thread to mount the aperture.

The holder is attached to a stainless steel spacer and further to a copper bar, called coldfinger, that reaches up to the inner stage of the cryocooler. The stainless steel piece reduces thermal stress to the cryocooler (section 5.5.2) during the cleaning process. To avoid residual gases freezing onto the HOPG it is surrounded by a cold trap, called inner coldshield, see figure 5.16. This inner coldshield is mounted to the coldfinger, above the stainless steel spacer. Therefore the temperature of the inner coldshield, measured by a Cernox type sensor, reaches below the substrate temperature during operation. A circular opening of the inner coldshield, in front of the substrate, functions as the mounting point for an aperture, defining the HOPG area visible to the spectrometers.

The outer coldshield is coupled to the second stage of the cryocooler and houses the inner coldshield as well as parts of the ellipsometry set-up. In figure 5.17 a frontal and side view is given. Below the inner coldshield a stainless steel mirror holder is situated, which provides space for a dielectric mirror. The holder can be adjusted using setscrews, such that the mirror can be aligned to reflect the ellipsometry laser beam centrally onto the HOPG (details see section 5.5.5).

Above the substrate on the outer coldshield, the analyzer and photodiode are placed inside a PEEK casing. To prevent misalignment, the PEEK is designed such that the correct orientation is predefined. The left side of figure 5.17

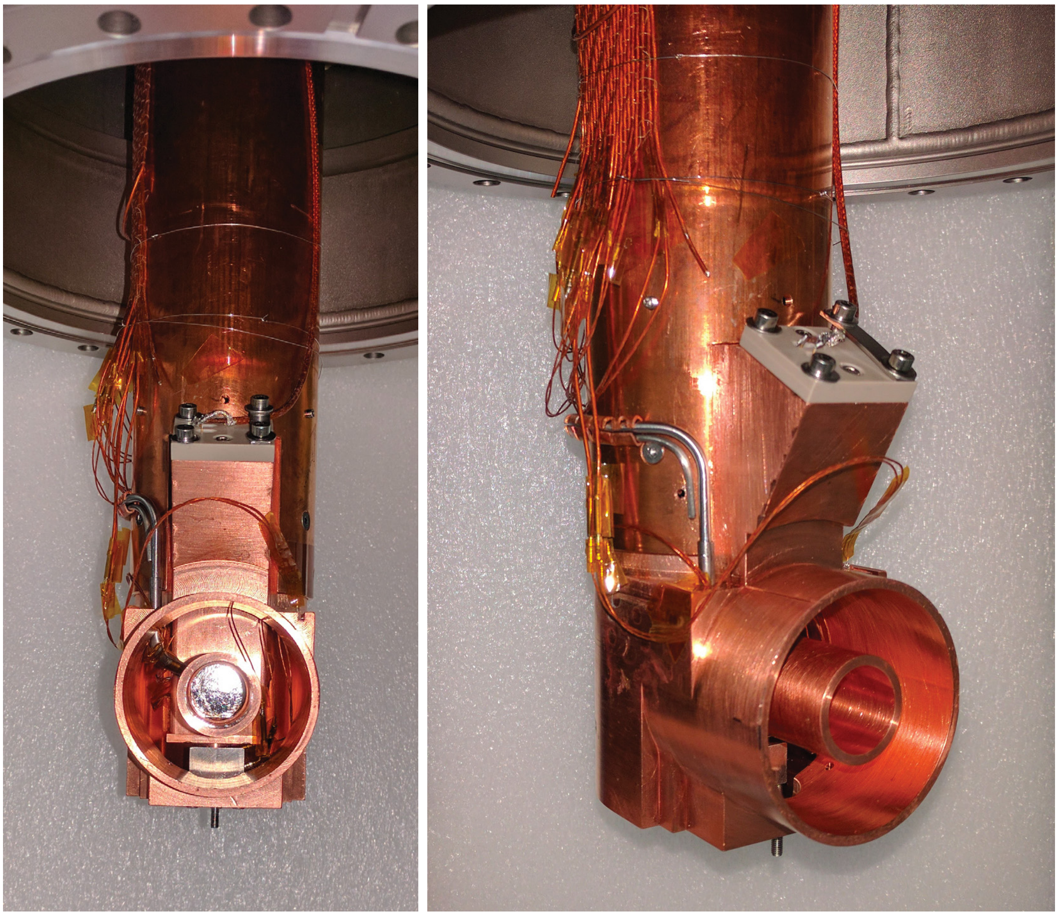

Figure 5.17: Assembly of the CKrS substrate region. The pictures show the substrate region of the CKrS with inner and outer coldshield covering the HOPG. The PEEK houses the analyzer and polarizer of the ellipsometry set-up. All temperature sensors are connect to the wire harness on the left side of the outer coldshield. The gray piping is the capillary for the transport of gaseous krypton.

shows the heatable capillary for the krypton gas supply and the cabling for all sensors and heaters.

The operational substrate region is closed by a copper lid with a 2 cm (diameter) hole on the front of the outer coldshield. This lid reduces the surface of the inner coldshield, which is seen from warmer parts of the KATRIN experiment. Since heat transfer is mainly due to radiation, this helps to achieve and maintain the required temperatures for proper operation.

5.5.5 Laser ellipsometry and ablation set-up

Ellipsometry is an optical method to investigate thickness and purity of a plain surface (see section 5.3). In case of the CKrS it is used to observe changes in the initial condensed krypton film, which can cause electron energy shifts and line broadening, due to solid state effects. Therefore a green Thorlabs HGP005 Laser, with 543 nm wavelength, shines through a linear polarizer and a quarter-wave plate to achieve circular polarized light, after being bend by a 45° dielectric mirror. Afterwards a rotatable linear polarizer and a compensator are introduced into the light beam, followed by two more dielectric mirrors with 1.5 m distance in between, pointing the laser spot onto the center of the substrate.

Depending on the surface properties the state of polarization is modified. The reflected light passes through a third linear polarizer, called analyzer, to a Si-PIN diode. Due to the analyzer the intensity of light seen by the diode varies depending on film purity and thickness. Here the null-ellipsometry method (section 5.3.2) is used, so the intensity vanishes at the photodiode for certain polarization states. This can be achieved by adjusting the polarizer and compensator angle via their rotatable mountings.

To clean the HOPG, the substrate is heated from behind via Zener diodes (see section 5.5.4) and an ablation laser. This laser, a Quantel Brilliant 2W, is a pulsed, frequency doubled Nd:YAG laser with a wavelength of $\lambda = 532\,\mathrm{nm}$ and energy output of $P_{\mathrm{Nd:YAG}} = 2\,\mathrm{W}$. During the process the laser illuminates

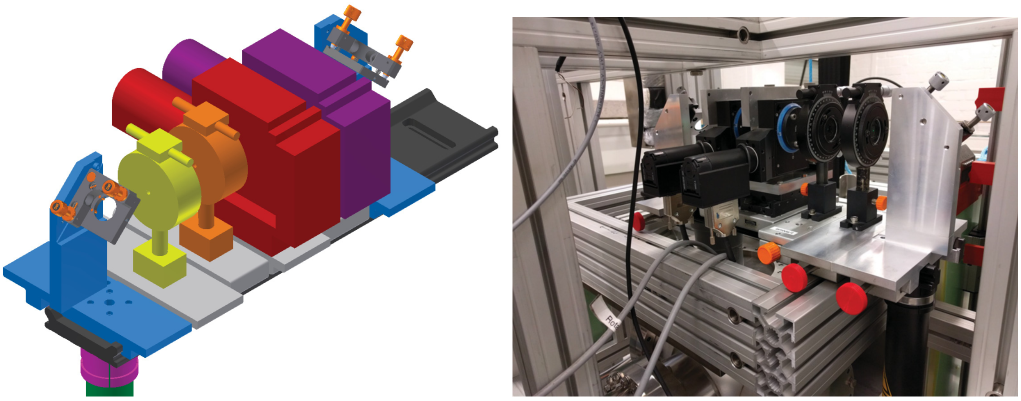

Figure 5.18: Ellipsometry laser and polarization preparation. The Laser light is deflected on a dielectric mirror (blue) pointing through a fixed linear polarizer (yellow) and quarter-wave plate (orange), two rotatable optical components, polarizer (red) and analyzer (purple) and a second mirror (blue) pointing inside of the CKrS. This set-up is space-saving and still tunable if it is out of adjustment.

the substrate with ultra short pulses ($\approx 5\,\mathrm{ns}$) at a repetition rate of 10 Hz for 180 s. Since the beam profile has been found to be non-gaussian [Bot12] in previous measurements, the laser beam is guided through a diffuser (Thorlabs UVFS Ground Glass Diffuser DGUV10-600) to homogenize it. Furthermore the diffuser paired with a collimating lens (Thorlabs Plano Convex Lense LA1027-A) acts as telescope. That way the laser beam covers the complete HOPG at one setting with a sufficient energy of $\mathcal{O}(300\,\mathrm{mWcm}^{-2})$ to evaporate frozen gases. The laser and telescope are installed in a light tight housing with an interlocked cover, in front of the ablation chamber. To access the chamber with the laser beam a window is placed directly after the laser telescope.

5.5.6 High voltage operation for post acceleration

Since the electron energy of the K-32 transition in $^{83\mathrm{m}}$Kr is 17.8243 keV [Sle15] and the tritium β-spectrum endpoint is near 18.6 keV, the CKrS is designed to be set on an elevated electric potential to overcome the energy gap. Therefore all movable parts of the set-up are electrically insulated against their surroundings. The bellow, connecting the CKrS vacuum and ablation chamber, is insulated against the CPS. On the movement platform the inner carriage is electrically decoupled by insulating plates. For safety issues, an interlocked high voltage fence surrounds the CKrS set-up to prevent unauthorized entering.

All devices connected to the CKrS vacuum chambers are operated on an elevated electric potential inside an isolated HV-rack. The same potential is applied to the coldfinger and therefore the substrate. The voltage required for this operation is generated by an external HV supply outside the HV-rack. During the krypton measurement campaign in 2017 the HV was grounded, hence commissioning and spectroscopic measurements of the krypton line have been performed without additional acceleration of the electrons.

5.5.7 Mechanical movement of substrate

The set up-of the condensed krypton source consists of a fixed scaffold, which is mounted on the CPS beamline and a movable lift, designed to enable the substrate region to enter and leave the CPS and furthermore to cover the complete flux tube. The movable structure consists of a carriage, which holds the main CKrS vacuum chamber, ellipsometry set-up, cryo- and gas system and is connected to the CPS with a bellow. In vertical direction the carriage is

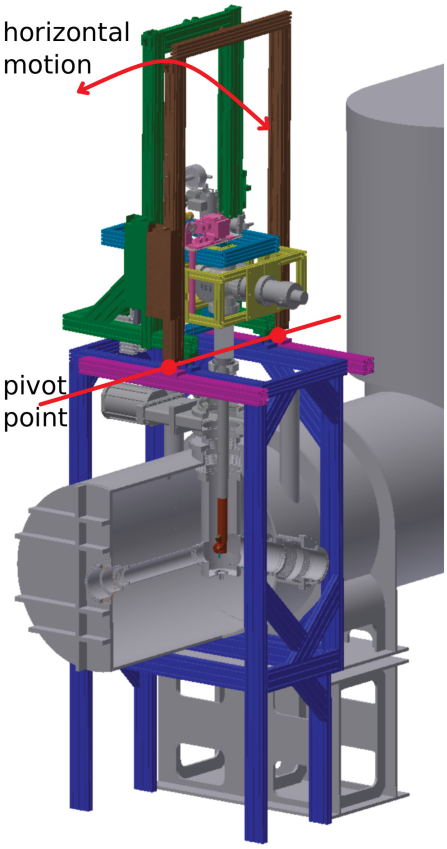

Figure 5.19: Horizontal motion of substrate region. The substrate is tilted around the pivot point. Combined with the linear vertical motion the substrate and therefore the active ^{83m}Kr film can be positioned anywhere in the whole flux tube.

moved along sliding rails with a motorized hoist, driven by an ISEL EC 86L synchronous motor and IMD 40 controller. To reduce stress on the motor the weight of the set-up is compensated with counterweights, so that only the force induced by the vacuum towards CPS has to be overcome. This mounting allows a free movement perpendicular to the beam axis. For horizontal displacements of the substrate within the flux tube, the structure allows for an angular movement around a pivot point driven by an ISEL synchronous motor, model EC 60L, regulated by an IMD 20 controller, since the load is smaller. The pivot point is positioned at the interconnection between the isolator above the ablation chamber and the bellow, see figure 5.19.

Considering, that the substrate and shielding must not collide with the inner walls of the CPS to prevent damage, a hardware and software safety system, directly coupled to the motor controls, is implemented. At the outer positions of the ranges of movement end stop switches by Euchner, model GLBF05R08-

552-M and GLBF04R08-552-M, are installed, which generate a stop signal for the ISEL controllers and thus stop the movement. These end stops define the safe movement space of the CKrS and are furthermore used to define an absolute position relative to the CPS beam tube. An automated routine [Sch17] determines the beam tube center position inside the CPS. The controlling and positioning is performed by a LabView program. This allows to enter a radius and an angle in KATRIN coordinates, which steers the substrate to the desired position. Hereby a detector pixel can be reproducibly illuminated.

In case of a hardware issue, that causes the motor controllers to move outside the safe parameter space, a second line of switches, Euchner NM01WOK-M, is in place to shutdown the motor power supply and therefore stop any movement. Additionally an emergency stop button is included in the hardware safety concept, which also causes power shutdown of the motion motors. Once one of these controls has been triggered the CKrS has to be moved manually back into the allowed range and reset afterwards. A drop in vacuum conditions or a safety failure in the KATRIN infrastructure leads to an automated extraction and parking of the CKrS. Such events are detected and processed independently by KATRIN’s PCS7 system, which then triggers the CKrS software for further steps.

5.6 Performance of the set-up

With the complete CKrS set-up placed within the KATRIN infrastructure, system checks are mandatory. The performance of the vacuum system and stable temperatures are crucial for purity of the condensed krypton films and to avoid freezing residual gases onto the substrate. To reach lowest pressures, a bakeout of the vacuum system is required. Unfortunately the time for this procedure has been very limited in the preparation of the 2017 Kr campaign. Therefore the bellow between CPS and CKrS main chamber has been baked out for 1 h at 120 °C. This temperature has been chosen to reach a sufficiently high temperature at the bellow and not to exceed the safety specifications of the cryocooler and the CPS valve. At the same time, the SAES getter pump was activated.

During pumping it was found that the prevacuum pump did not deliver the specified performance and had to be changed. The pressure readings of the CKrS main chamber gauge prior to and during the krypton measurement phase is displayed in figure 5.20. Until the change of the prevacuum pump the pressure readings were in the range of 10^{-7} mbar despite active cryopumping. After pump replacement, pumping and cryopumping (the coldest parts of the coldshields of the CKrS act as a cryopump for residual gases, improving the vacuum by about one order of magnitude) lead to a reliable and stable pressure within the CKrS main chamber, below the sensitivity of the used ITR 90 gauge at $< 10^{-9}\,\mathrm{mbar}$.

The temperature readings (see figure 5.21) indicate that the required substrate temperature below 30 K is reachable and reproducible. The bakeout of the bellow leads to a temperature rise of the internal components of 50 °C, which causes no harm to the cold head indium sealing gaskets and the CPS valve. Through the following two cryopumping cycles the critical temperature of 30 K of the HOPG substrate was surpassed each time, although the main chamber pressure started to rise. Improving the vacuum conditions enhanced the temperatures, especially for the sensors along the outer parts of the cryosystem. Capillary and nozzle temperature stayed above 130 K so the krypton does not freeze inside the piping [Ost08] and therefore no active

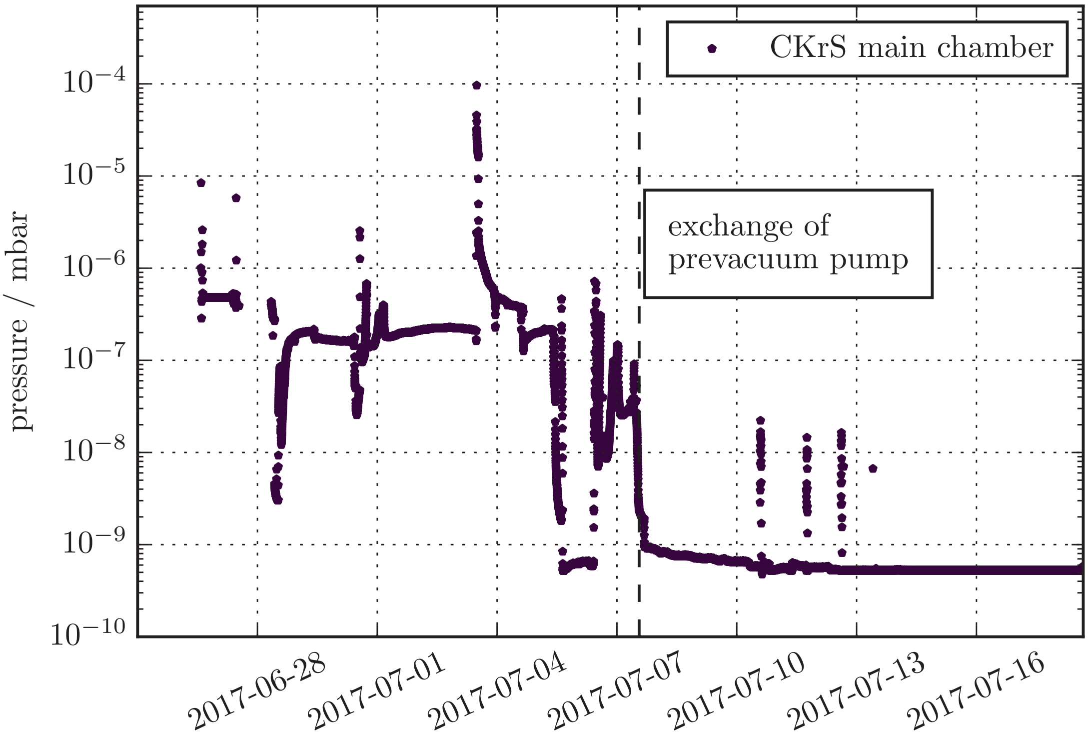

Figure 5.20: Pressure readings at the CKrS. Until the change of the prevacuum pump the pressure inside the CKrS staged in the 10^{-7} mbar range, even though the cryocooler was operating. Afterwards the pressure levels dropped below the gauges sensitivity at $< 10^{-9}\,\mathrm{mbar}$ and remained there during the measurement period.

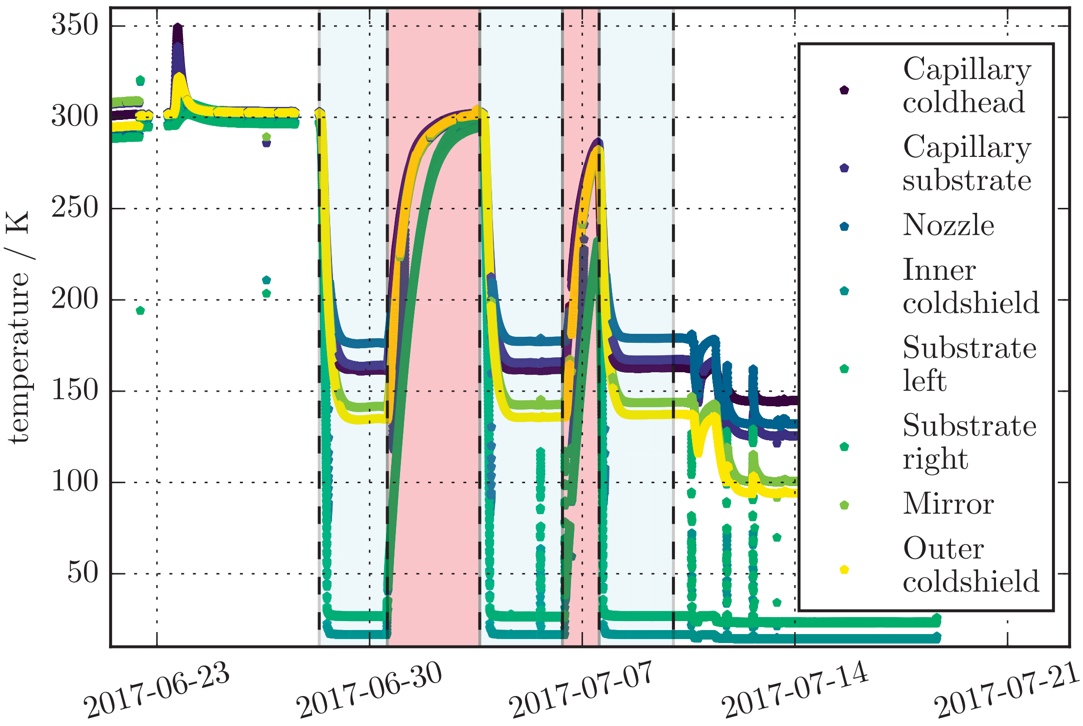

Figure 5.21: Cool down of substrate region. With cryocooling the temperatures for stable operation, substrate below 30 K, are reached reproducibly.

heating was necessary. The inner coldshield reaches down to ~16 K and thus acts as a cold trap for residual gases.

In figure 5.22 a detailed view of the temperature behavior while cleaning the HOPG substrate is given. For every cleaning cycle the two Tenma power supplies of the Zener diodes were set to 25 V and the current output was ramped up in 50 mA steps. After reaching the maximal current the ablation laser is activated three times for 180 s. The rise in substrate and inner coldshield temperature and pressure is clearly visible. After the first HOPG heating the temperatures of the outer cold parts decrease further. With the further falling pressure inside the vacuum chamber the temperatures fall again prior to the second cleaning of the HOPG. After the second and third heating cycle the temperatures stabilize afterwards at the same values and do not decrease further.

Since pressure and temperature behaved according to their specifications, the movement of the source inside the CPS had to be tested next. Therefore a $^{83\mathrm{m}}$Kr film was prepared on the HOPG, introduced into the beam tube and centered in the CPS. The first positioning has been performed manually without the LabView routines introduced in [Sch17], by live count rate readings of the

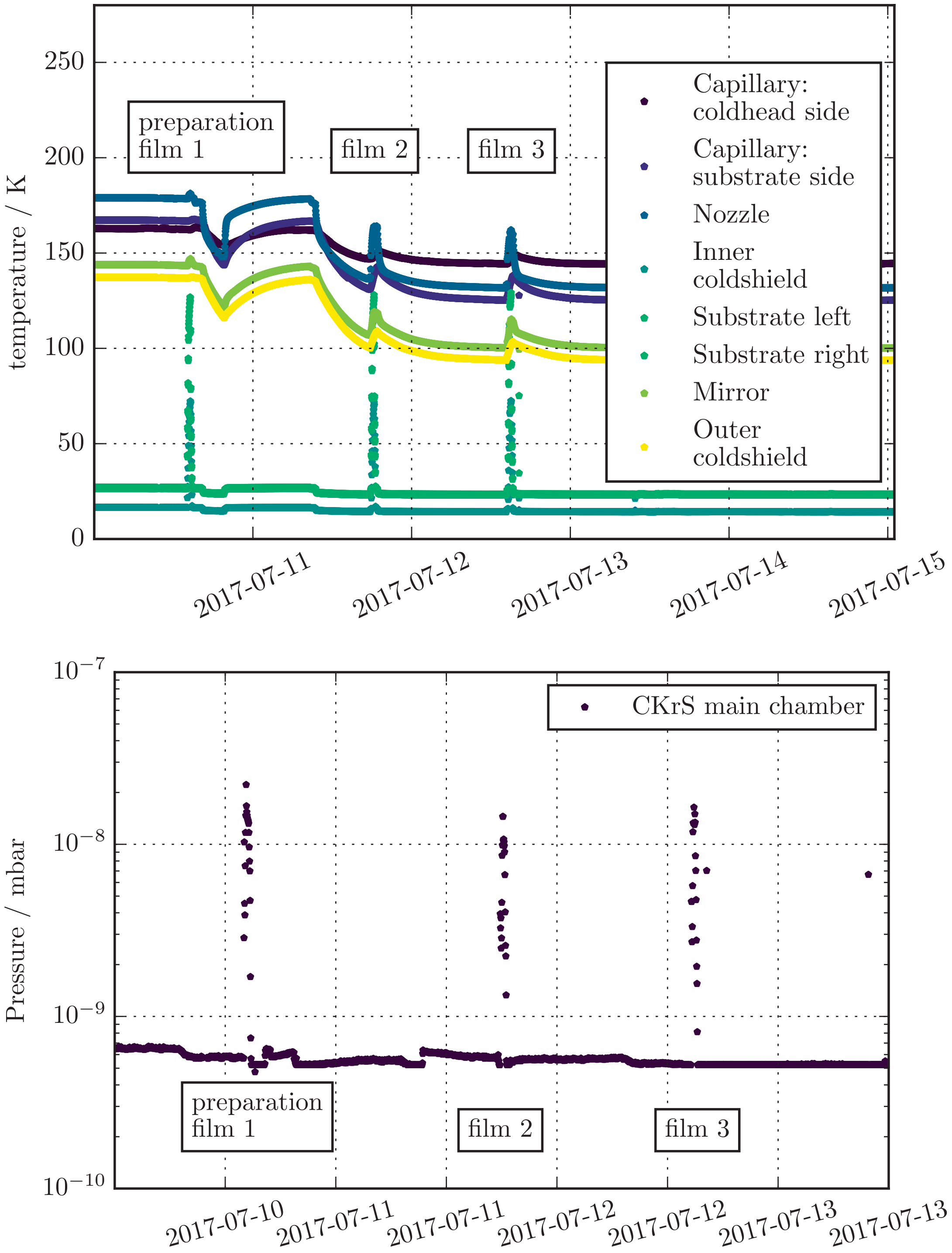

Figure 5.22: Detailed temperature and pressure readings during substrate heating. The local heating and ablation of the HOPG substrate increases the temperature sufficiently for cleaning (~120 K). The evaporated gases, krypton and residual gases, lead to a pressure increase, which gets pumped out. This leads to an improved pressure and temperature at the substrate.

FPD. This has been done to keep full control over the motor steering until the center position, visible on the FPD, has been reached. Starting from this position the CKrS was programmed to move to several positions inside the flux tube [RFD+17] [SMBFP17]. During the motorized movement, several minor software issues have been discovered, but could be corrected on site. Later positioning has been accomplished using the automated routines and all FPD pixels could be reproducibly reached. Figure 5.23, top, shows the first ^{83m}Kr electrons from the CKrS reaching the FPD. The spatial extend of the HOPG substrate leads to a signal spread, which is wider than a single pixel. Nevertheless, the maximal count rate is sufficiently localized. The bottom part of figure 5.23 displays data from four measurements, where the CKrS substrate was positioned subsequently on four pixels of ring 7 of the FPD.

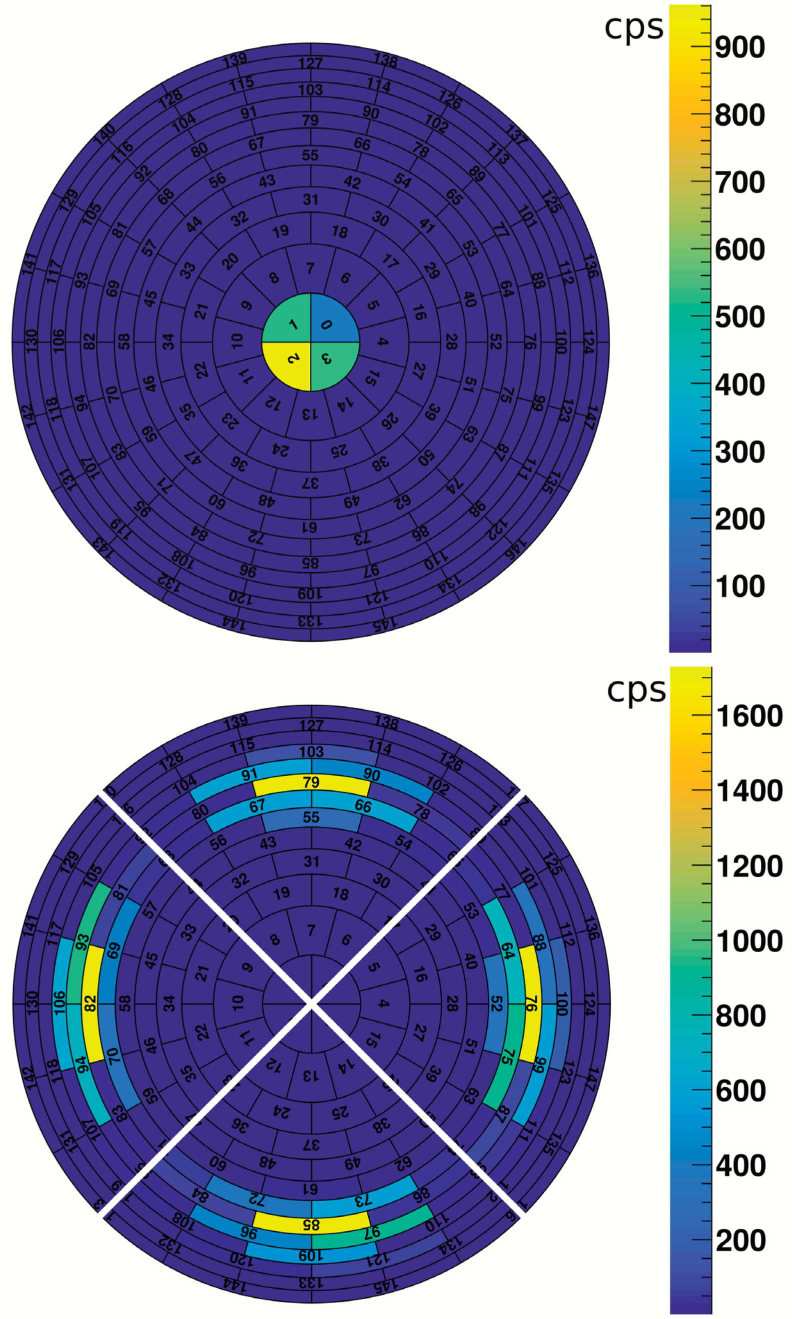

Figure 5.23: Electron count rate at the FPD for different CKrS positions. Starting from a centered position (top) the CKrS is moved to defined positions on ring 7 of the Focal Plane Detection System. Due to the spatial extent of the substrate, the source also illuminates smaller parts of pixels in the direct vicinity.

5.7 First measurements

Prior and during the Krypton measurement phase in July 2017 the condensed Krypton source has been commissioned and first measurements have been performed. During commissioning the interplay of all subsystems was tested in terms of reliability and reproducibility.

5.7.1 Krypton film activity

After cleaning the substrate, gaseous $^{83\mathrm{m}}$Kr is continuously introduced via the gas systems capillary, which ends at the HOPG substrate. At the substrate the krypton atoms condense on the cold substrate, if the temperature is sufficiently low (below 30 K [Ost08]). In a long term measurement the count rate evolution has been observed to estimate the time, which is needed to achieve a stable film activity after opening the valve to the ^{83}Rb generator. For this measurement the main spectrometer was set to a fixed voltage $U_{\mathrm{ret}} = -31.21\,\mathrm{kV}$ and the event rate on the FPD was monitored. In figure 5.7.1 the observed rate as a function of time is shown for a 20 h window.

By fitting the measured count rate N_{count} with a saturation curve,

$$N_{\mathrm{count}}(t) = a \cdot (1 - e^{-\lambda \cdot t}) + b\,, \tag{5.21}$$

with the amplitude a, the growth constant λ and the offset b, a saturation time can be calculated. After ca. 12 h the count rate reaches 99 % of the maximal value and from this time on, operation with stable activity is possible.

In longer measurements of the same prepared film the activity of the continuously condensing $^{83\mathrm{m}}$Kr is found to be slowly decreasing. This is due to the lifetime of the ^{83}Rb generator providing the krypton isomer. Its half-life and the exponential decay of the mother isotope reduces the activity of the frozen film. Figure 5.25 shows a prolonged measurement of the previously mentioned film. The dataset is approximated after the time estimated for film stabilization with an exponential fit. The fitted half-life of (86.5 ± 2.6) d [ABB^{+}18b] is within the uncertainties in agreement with the literature value of $T_{1/2} = (86.2 \pm 0.1)$ d [McC15].

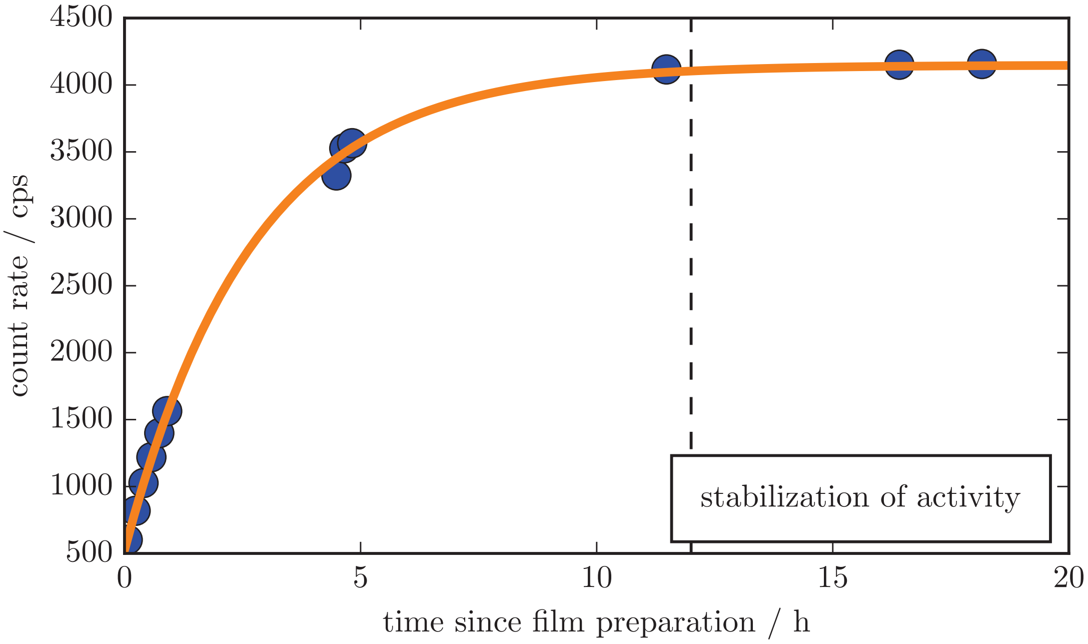

Figure 5.24: Observed electron rate as a function of time after opening the valve to the ^{83}Rb generator. After ca. 12 h the count rate saturates and becomes stable.

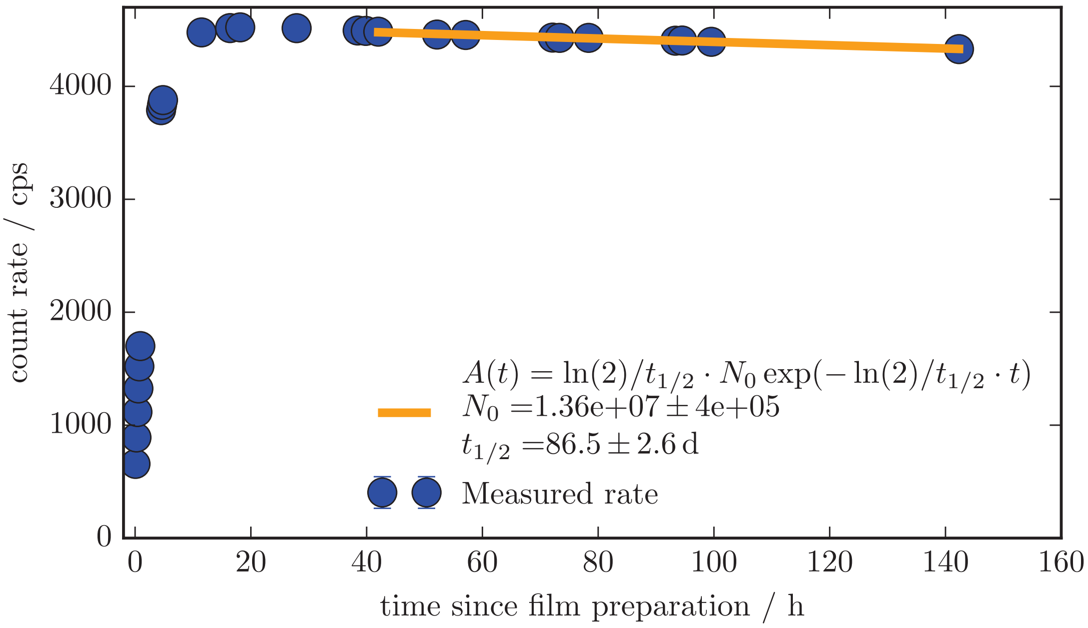

Figure 5.25: Longterm behavior of $^{83\text{m}}$Kr film. For long time scales the rate decreases with the half life of ^{83}Rb. Plot adapted from [ABB^{+}18b].

5.7.2 Estimation of the absolute film activity

A determination of the absolute substrate activity helps to understand the transport efficiency of Krypton gas from the Rubidium generator, through the capillary to the HOPG substrate. For that purpose the M_2/M_3 measurements from the Krypton measurement campaign were chosen. The count rates of these line measurements registered on the FPD are low enough to avoid detector effects like pile up or dead time issues [BE17]. To deduce the ^{83m}Kr activity the branching ratio of the considered lines are needed, which are $M_{2,\text{branch}}$: 2.99 % and $M_{3,\text{branch}}$: 4.65 %, see table 5.1. Furthermore an estimation of the electron transport efficiency from substrate to FPD and therefore the acceptance of the measurement was performed with a simple model of the CKrS substrate region introduced into the Kassiopeia simulation framework. It considers the geometry of the substrate, the aperture and the outer cold shield. The active area of the substrate is defined as the circular projection of the aperture on the HOPG. Although krypton gas will also freeze on the outer edges of the substrate and the cold copper parts in its vicinity, electrons emitted from these places will mostly be absorbed by the walls of the inner coldshield and therefore neglected. In the simulation $n_{\text{sim., started}} = 10000$ evenly distributed electrons were started on the HOPG. These electrons were generated with isotropically distributed starting angles between 0° and 90° w. r. t. the HOPG surface. At the detector $n_{\text{sim., hit}} = 9691$ events were registered. To speed up the simulation, the electrons were only tracked magnetically to the detector, therefore the hit events have to be corrected c_{mirror} for magnetic reflection at the pinch magnet. By calculating the cut-off angle $\vartheta_{\text{mirror}}$ at the pinch magnet,

$$\vartheta_{\text{mirror}} = \arcsin\left(\sqrt{B_{\text{start}}/B_{\text{pinch}}}\right) = 27.58° \,, \tag{5.22}$$

only 11.36 % of all hits are actually reaching the detector. Herein $B_{\text{start}} = 0.9\,\mathrm{T}$ denotes the magnetic field strength at the position, where the electrons are created (the HOPG substrate) and $B_{\text{pinch}} = 4.2\,\mathrm{T}$ describes the magnetic field strength of the pinch magnet. Taking transport, branching and measured event rates R_{event} for the M_2 and M_3 lines (run # 33526) into account the ^{83m}Kr activity on the HOPG can be calculated by:

$$R_{\text{HOPG}} = 2 \cdot R_{\text{event}} \cdot a_{\text{transport}} \cdot a_{\text{branch}} \,, \tag{5.23}$$

$$a_{\text{transport}} = \frac{n_{\text{sim., started}}}{n_{\text{sim., hit}} \cdot c_{\text{mirror}}} \,, \quad a_{\text{branch}} = \frac{1}{M_{2,\text{branch}} + M_{3,\text{branch}}} \tag{5.24}$$

Thus resulting in an activity of $638 \pm 4\,$kBq. Compared to the initial Rubidium generator ($\approx 7\,\mathrm{MBq}$) the transport efficiency of the capillary is therefore about 9.1 %.

5.7.3 First line measurements

With the condensed ^{83m}Kr film spectroscopic measurements of the several conversion electron lines are performed to investigate the line width and energy stability of the CKrS. This covered both the 32 keV and 9.4 keV γ transitions with their various lines (denoted in table 5.1). For a first analysis the focus lies on the M_2/M_3 lines of the K-32 transition, because detector effects like pile up or dead time issues [BE17] can be neglected. The integral spectrum of these two lines are measured among others in run #33295 to #33579 and described in [FTF$^+$17]. Exemplary the spectrum of run #33452 is shown in figure 5.26. To optimize the fit, relativistic effects are included in the routine. Additionally a sinusoidal ripple of the vessel high voltage, with an amplitude of 480 mV peak-to-peak [RRT17] [Res17], has to be considered. This leads to a reduced χ^2 of the fit of 1.82.

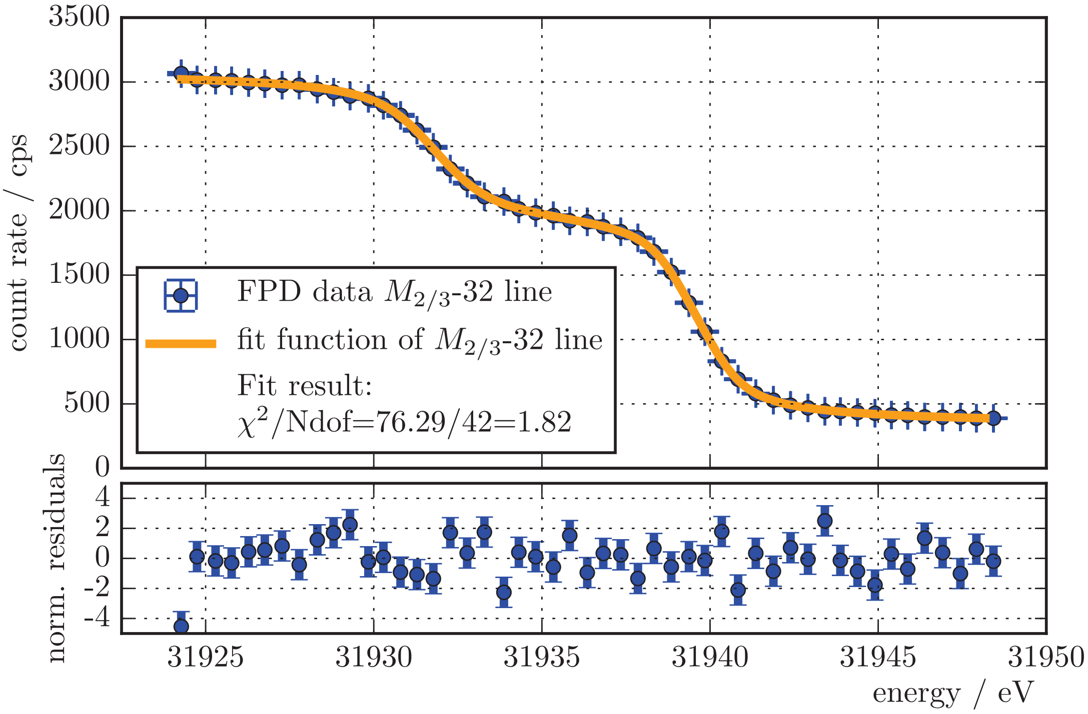

Figure 5.26: Integral spectrum of a K-32 M_2/M_3 line measurement with the condensed krypton source. In blue the measured data points and uncertainties are displayed. The orange line is the best fit including relativistic effects and a sinusoidal high voltage ripple.

5.7.4 Line stability

During the krypton measurement phase the films on the HOPG substrate have been continuously monitored by means of laser ellipsometry, see section 5.3. This is due to the fact that changes in the ellipsometry signal directly point to changes on the source properties, that will influence the position of conversion electron lines. Since three $^{83\mathrm{m}}$Kr film preparations have been performed during the campaign with prior cleaning by heating and laser ablation, these cycles are investigated, respectively.

For this purpose the polarizer and compensator angles are plotted in figure 5.27 and 5.28 against the time. Both graphs are subdivided into three parts for every new film preparation. The first two films have been cleaned after a period of nearly 24 h, the last one has been untouched for the rest of the measurement period to gain more insight into the long term behavior. Comparing the change for all three films it becomes obvious that the slope flattens for every new preparation. This indicates improving vacuum conditions and therefore less impurities accumulated on the HOPG. A detailed analysis of the film behavior will be given in [Fed19].

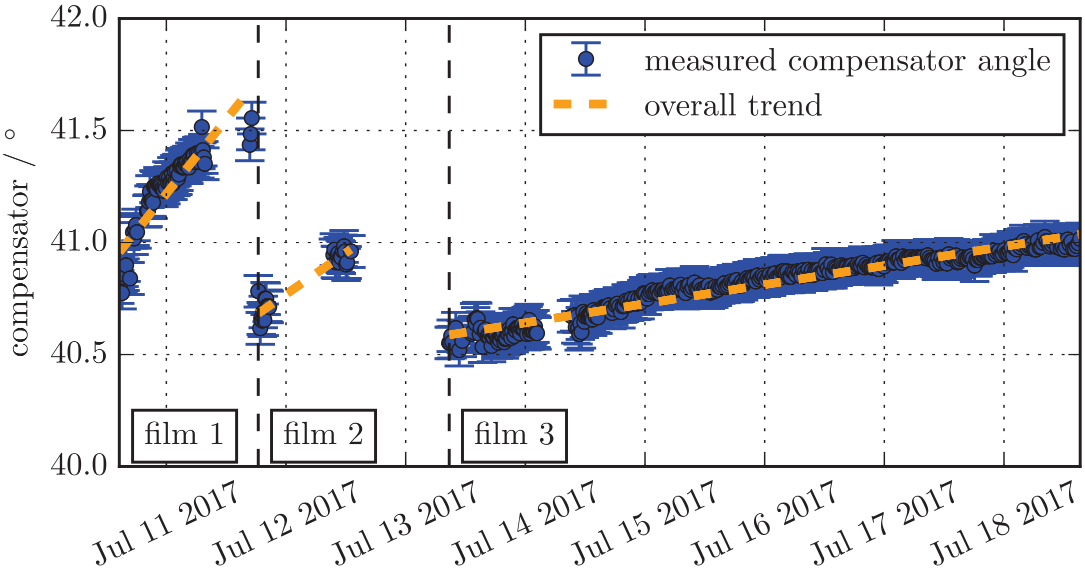

Figure 5.27: Change in compensator angle during CKrS campaign. With every cleaning of the substrate the film purity improves, since previously frozen residual gases are evaporated and pumped away. Furthermore the vacuum conditions improve by prolonged pumping times. This leads to a reduced rate of change of the compensator angle for film 3 compared to the first two films.

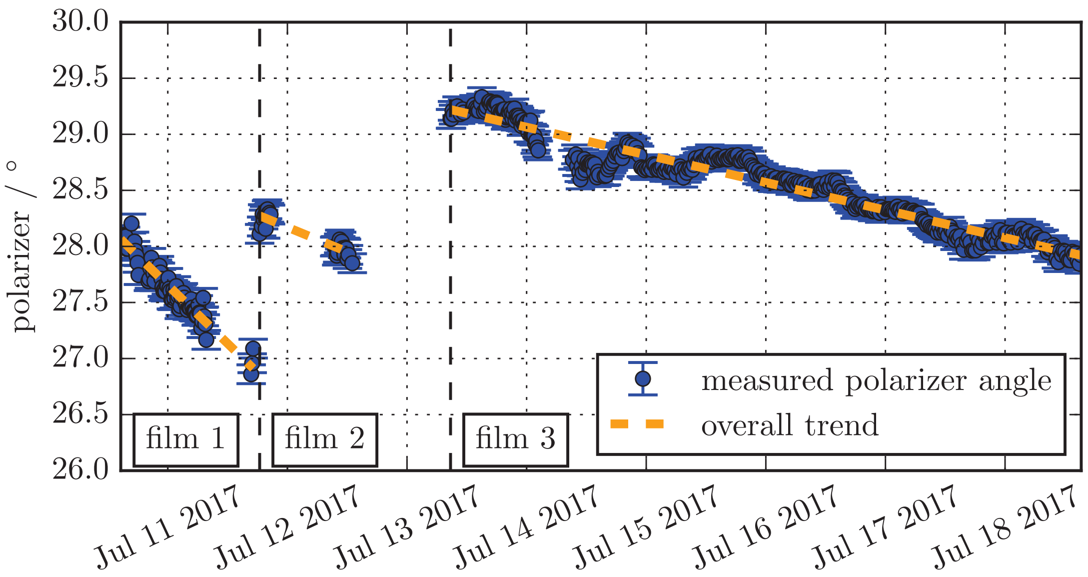

Figure 5.28: The polarizer angle shows a behavior similar to the compensator angle. With the newly frozen krypton films the slope of the angle drift flattens, which is due to improvements in vacuum conditions and film purity.

The effect of residual gas continuously condensing on the HOPG substrate together with the $^{83\mathrm{m}}$Kr is visible in the line position shifts in figure 5.29. The investigation has been performed by measuring the M_2 and M_3 line repeatedly. With increasing time after the initial film preparations the line positions shift to lower values, but as in the polarizer and compensator measurements these line positions shifts tend to flatten out.

After ca. 72 h the remaining line drift, of the measurement interval with film 3, is about 0.4 meV h^{-1}. To further improve on the line stability, an extended bakeout of the complete set-up, including the gas system and the ^{83}Rb generator has been performed prior to the 2018 CKrS measurements. In addition, to reduce the effect of image charges on the line position a pre-plated film of stable krypton has been applied to the HOPG substrate before freezing on $^{83\mathrm{m}}$Kr in the latest measurements. With these improvements, the stability of the line positions measured with the CKrS could be improved to the 0.3 meV h^{-1} level over the complete measurement period of 100 h [Ful19].

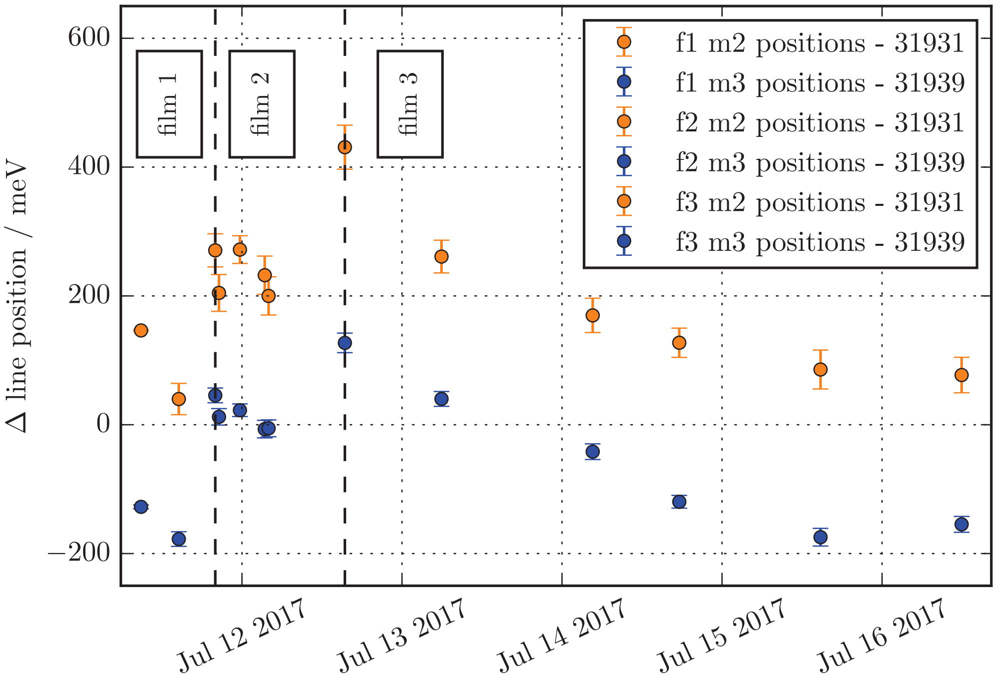

Figure 5.29: Relative change in line position of the M_2 and M_3 line measured with the CKrS during the 2017 measurement campaign. The prepared ^{83m}Kr films improve in their properties over time, which is visible in the reduced line shifts for the later measurement in the ellipsometry measurements (see figures 5.27 and 5.28). The remaining line drift at the end of the measurements with film 3 is about 0.4 meV h^{-1}.

Chapter 6

Conclusions and outlook

In the 30s of the last century neutrinos have been postulated by W. Pauli [Pau30] as an attempt to save the fundamental conservation laws of physics. This marks the beginning of neutrino physics as an independent field of research, within nuclear and particle physics. Although the standard model of particle physics describes the neutrino as a massless particle, neutrino oscillation experiments have proven, that the neutrino mass is non-zero. However, an absolute measurement of this property still needs to be accomplished and different approaches have emerged to determine the ν-mass. One of the most promising methods is the precise measurement of the endpoint region of the tritium β-spectrum. With this method the Mainz and Troitsk neutrino experiments obtained an upper limit for the average electron anti-neutrino mass of $m_{\bar{\nu}_\mathrm{e}} < 2\,\mathrm{eV}$ [KBB+04] [ABB+11].

The KATRIN experiment is based on the same technique (MAC-E filter) as the latter experiments and aims to improve the mass sensitivity by an order of magnitude to 0.2 $\mathrm{eV/c^2}$ at 90 % C.L.. The experiment is subdivided into five major sections, the rear section, the windowless gaseous tritium source, with an activity of about 10^{11} Bq, a transport section to remove residual tritium molecules, a following tandem of two MAC-E filter type spectrometers and the segmented focal plane detector. From the source onwards, the decay electrons are guided magnetically towards the detector. With the main spectrometer, a high precision energy analysis of the tritium β-electrons will be performed with a resolution of 0.93 eV. The spectrometer acts as a high pass filter for the kinetic energy of the decay electrons, allowing to measure an integrated electron spectrum, which is analyzed for the neutrino mass. To reach the anticipated sensitivity the experiment aims for a background level of about 10 mcps in the region of interest at the energy spectrum. Since the actual background exceeds the design level by more than one order of magnitude, suitable background reduction methods have to be discussed.

One of the systems designed to reduce experimental background and at the same time help to fine-tune the electric potentials inside the spectrometer is the inner wire electrode of the main spectrometer. During the first spectrometer bakeout, the wire electrode system inside the spectrometer vessel developed electrical short circuits between several wire layers. This was found to be due to the loss of stiffness of copper beryllium rods in the high voltage distribution system. In a repair effort several of the observed short circuits could be repaired. However, the evacuated spectrometer showed reappearing short circuits in the eastern dipole half of the spectrometer, although this half has undergone a repair. By calculating potential settings for western and eastern dipole half that create a joint effective potential inside the spectrometer, background measurements with part of the spectrometer operated in dual layer mode were performed and analyzed. The effect of the half-sided double layer electrode caused an evidently lowered background rate. In a further approach, the spectrometer has been temperature cycled, introducing a falling and later rising temperature gradient. This released the short circuit in the eastern dipole half for a certain time and allowed measurements with a full double layer operation of the central spectrometer region. Like in the effective potential settings, the background rate has been distinctly decreased for certain potential settings of the double layer electrode.

To understand the origin of the elevated background level, several dedicated measurements have been performed. Various processes like radon decays inside the spectrometer volume or temperature and pressure dependencies of the overall background have been discussed. Furthermore contributions by secondary electron emission of the vessel wall and muon induced background can explain the background events only to a certain degree. The remaining background is heavily discussed and one possible hypothesis is based on hydrogen Rydberg atoms, which are neutral atoms with high principle quantum numbers n. These states are believed to be created in radioactive decays of trace elements at the vessel surface. The neutral atoms can propagate freely through the spectrometer, because they are not affected by the magnetic field and electric potential present in the main spectrometer. Due to blackbody radiation of the spectrometer, the hydrogen Rydberg atoms can be ionized and therefore emit an electron. In order to reduce this volume dependent background and investigate the energy composition of the background electrons, alternative electric potential and magnetic field settings for the main spectrometer have been introduced. With these potential and field settings the analyzing plane has been shifted from the center of the spectrometer towards either the source side flat cone or the detector side flat cone. With this method the effective spectrometer volume between analyzing plane and focal plane detector can be varied, which alters the background rate seen at the detector. The measured rate for both shifted settings (source side: 709 ± 10 mcps / detector side: 165 ± 4 mcps) revealed a linear relation between the background events and the flux tube volume. Additionally this shifted analyzing plane setting allowed a spectroscopic measurement of the energy spectrum of the background electrons by increasing the potential barrier at the detector side. With a simplified simulation, the energy spectrum could be extracted. The best fit to the measured count rates at increasing blocking potentials shows two distinct features. Ca. 38 ± 4 % of the electrons creating the background have a kinetic energy in the range of 400 meV to 700 meV. A further fraction of 40 ± 17 % of the electrons have energies around 3.0 eV. An additional constant background term has been added to the fit to account for, among others, the remaining volume between analyzing plane and detector at maximum blocking potential. This constant background contributes 35 ± 4 mcps to the total rate. In [Pol18], more recent spectroscopic measurements are discussed, that aim to determine the energy composition of the background electrons with different approaches, using magnetic trapping and differently optimized electric potentials. Preliminary results from these newer measurements exhibit a similar energy distribution of the background electrons as has been observed in this work.

To investigate the shifted analyzing plane as a possible tritium β-measurement mode the spectrometer has been examined with an angular selective and monoenergetic electron source. This mode is considered because of its significant reduction in background rates. Simulations and measurements showed, that a ring-wise analysis of the detector is mandatory, since the transmission function is shifted by ca. 3 eV from inner to outer detector radii. Increasing the pitch angle of the starting electrons by varying the backplate angle of the electron source, also leads to a shift of the measured transmission functions, which corresponds to a broadening of the transmission function for an isotropically emitting source. Additionally the predicted maximal pitch angle (where electrons are magnetically reflected at the pinch magnet) could not be reached. For the highest pitch angles the shape of the transmission function changes and the rate seen on the detector starts to decrease. This indicates a change in transmission properties for electrons with high pitch angles passing the spectrometer, thus requiring more sophisticated measurements and simulations to fully characterize the shifted analyzing plane settings.

To calibrate the spectrometer transmission properties and to characterize the electric potential inside the spectrometer, a quench condensed krypton source (CKrS) has been set up and commissioned. This source isotropically emits monoenergetic electrons from $^{83\mathrm{m}}$Kr gas adsorbed on a cooled HOPG substrate. Horizontal and vertical movement of the substrate allows a spatial investigation of the transmission properties of the spectrometers. The CKrS set-up consists of a vacuum system to provide ultra high vacuum conditions, a cryo system to freeze the gaseous $^{83\mathrm{m}}$Kr to the HOPG substrate, a gas system to provide stable krypton for pre-plating and radioactive $^{83\mathrm{m}}$Kr gas from a ^{83}Rb generator for the measurement runs. Additionally a laser ellipsometry set-up monitors the condensed sub-monolayer $^{83\mathrm{m}}$Kr films for thickness and purity changes and a HV system allows to electrically elevate the HOPG for upcoming measurement phases. Previous to the krypton measurement campaign of 2017 the CKrS set-up has been installed in the KATRIN infrastructure and commissioned to verify the expected performance. The desired temperatures below 30 K at the substrate and pressures $\sim 10^{-10}$ mbar have been reproducibly reached. The movement system could be used to reach all allowed flux tube positions to project the $^{83\mathrm{m}}$Kr conversion electrons from the HOPG substrate to single pixels of the FPD. The measured count rates saturate ca. 12 h after the initial inlet of $^{83\mathrm{m}}$Kr gas. After the saturation the activity of the substrate has been deduced to be 638 ± 4 kBq for a 7 MBq ^{83}Rb generator by comparing measurements with electron transport simulations. First measurements in the 2017 krypton campaign allowed to scan the numerous $^{83\mathrm{m}}$Kr conversion lines. During the measurements, three $^{83\mathrm{m}}$Kr films have successfully been condensed after previous cleaning by heating with Zener diodes and laser ablation. For each new film the line stability was found to improve. The line drift of the third film saturated with a remaining line drift of $\sim 0.4\,\mathrm{meV\,h^{-1}}$ after ca. 72 h from the film preparation. In the 2018 campaign measurements, the line stability has been further improved to $0.3\,\mathrm{meV\,h^{-1}}$ over the full measurement period of 100 h. The analysis of data taken during the two measurement campaigns is subject of the PhD theses of Fulst [Ful19] and Fedkevych [Fed19]. The CKrS will be used in the future to recalibrate the transmission properties and HV stability in between tritium β-measurement runs.

References

[A^{+}05] J. Angrik, T. Armbrust, A. Beglarian et al. *KATRIN Design Report 2004, Wissenschaftliche Berichte FZKA 7090*. Technical report, Forschungszentrum Karlsruhe, 2005. URL: `http://bibliothek.fzk.de/zb/berichte/FZKA7090.pdf`.

[A^{+}12a] Y. Abe, C. Aberle, J. C. dos Anjos et al. *Reactor $\overline{\nu}_e$ disappearance in the Double Chooz experiment*. Phys. Rev. D, 86:052008, Sep 2012. URL: `http://link.aps.org/doi/10.1103/PhysRevD.86.052008`, `doi:10.1103/PhysRevD.86.052008`.

[A^{+}12b] J. K. Ahn, S. Chebotaryov, J. H. Choi et al. *Observation of Reactor Electron Antineutrinos Disappearance in the RENO Experiment*. Phys. Rev. Lett., 108:191802, May 2012. URL: `http://link.aps.org/doi/10.1103/PhysRevLett.108.191802`, `doi:10.1103/PhysRevLett.108.191802`.

[A^{+}12c] F. P. An, J. Z. Bai, A. B. Balantekin et al. *Observation of Electron-Antineutrino Disappearance at Daya Bay*. Phys. Rev. Lett., 108:171803, Apr 2012. URL: `http://link.aps.org/doi/10.1103/PhysRevLett.108.171803`, `doi:10.1103/PhysRevLett.108.171803`.

[A^{+}14] Ade, P. A. R., Aghanim, N., Armitage-Caplan, C. et al. *Planck 2013 results. XVI. Cosmological parameters*. Astron. Astrophys., 571:A16, 2014. URL: `http://dx.doi.org/10.1051/0004-6361/201321591`, `doi:10.1051/0004-6361/201321591`.

[AAA^{+}02] Q. R. Ahmad, R. C. Allen, T. C. Andersen et al. *Direct Evidence for Neutrino Flavor Transformation from Neutral-Current Interactions in the Sudbury Neutrino Observatory*. Phys. Rev. Lett., 89:011301, Jun 2002. URL: `https://link.aps.org/doi/10.1103/PhysRevLett.89.011301`, `doi:10.1103/PhysRevLett.89.011301`.

[AAA^{+}06] M. H. Ahn, E. Aliu, S. Andringa et al. *Measurement of neutrino oscillation by the K2K experiment*. Phys. Rev. D, 74:072003, Oct 2006.

URL: `https://link.aps.org/doi/10.1103/PhysRevD.74.072003`, `doi:10.1103/PhysRevD.74.072003`.

[AAB+04] S. N. Ahmed, A. E. Anthony, E. W. Beier et al. *Measurement of the Total Active* ^{8}B *Solar Neutrino Flux at the Sudbury Neutrino Observatory with Enhanced Neutral Current Sensitivity*. Phys. Rev. Lett., 92:181301, May 2004. URL: `https://link.aps.org/doi/10.1103/PhysRevLett.92.181301`, `doi:10.1103/PhysRevLett.92.181301`.

[AB87] R. M. A. Azzam, N. M. Bashara. *Ellipsometry and Polarized Light*. Elsevier Science Ltd., 1987.

[ABB+11] V. N. Aseev, A. I. Belesev, A. I. Berlev et al. *An upper limit on electron antineutrino mass from Troitsk experiment*. 2011. `arXiv:arXiv:1108.5034`, `doi:10.1103/PhysRevD.84.112003`.

[ABB+16] M. Arenz, M. Babutzka, M. Bahr et al. *Commissioning of the vacuum system of the KATRIN Main Spectrometer*. Journal of Instrumentation, 11(04):P04011, 2016. URL: `http://stacks.iop.org/1748-0221/11/i=04/a=P04011`.

[ABB+18a] M. Arenz, W. J. Baek, M. Beck et al. *Muon-induced background in the KATRIN main spectrometer*. 2018. `arXiv:arXiv:1805.12173`.

[ABB+18b] M. Arenz, W.-J. Baek, M. Beck et al. *First transmission of electrons and ions through the KATRIN beamline*. Journal of Instrumentation, 13(04):P04020, 2018. URL: `http://stacks.iop.org/1748-0221/13/i=04/a=P04020`.

[AEE+05] T. Araki, K. Eguchi, S. Enomoto et al. *Measurement of Neutrino Oscillation with KamLAND: Evidence of Spectral Distortion*. Phys. Rev. Lett., 94:081801, Mar 2005. URL: `https://link.aps.org/doi/10.1103/PhysRevLett.94.081801`, `doi:10.1103/PhysRevLett.94.081801`.

[AR87] W. David Arnett, Jonathan L. Rosner. *Neutrino mass limits from SN1987A*. Phys. Rev. Lett., 58:1906–1909, May 1987. URL: `https://link.aps.org/doi/10.1103/PhysRevLett.58.1906`, `doi:10.1103/PhysRevLett.58.1906`.

[Arl09] H. Arlinghaus. *Investigation of the muon-induced secondary electron background in the KATRIN Experiment*. Diploma thesis, Westfälische Wilhelms-Universität Münster, 2009.

[Bab14] Martin Babutzka. *Design and development for the Rearsection of the KATRIN experiment*. PhD thesis, 2014.

[Bau13] S. Bauer. *Energy calibration and stability monitoring of the KATRIN experiment*. PhD thesis, Westfälische Wilhelms-Universität Münster, 2013.

[BBB+12] M Babutzka, M Bahr, J Bonn et al. *Monitoring of the operating param-*

eters of the KATRIN Windowless Gaseous Tritium Source. New Journal of Physics, 14(10):103046, 2012. URL: `http://stacks.iop.org/1367-2630/14/i=10/a=103046`.

[BCG$^+$13] J.D. Behrens, T.J. Corona, F. Glück et al. *EMD consequences of electrical shorts at the inner electrode system*. Technical report, Forschungszentrum Karlsruhe, 2013. URL: `https://fuzzy.fzk.de/bscw/bscw.cgi/d875477/430-doc-3-9002-EMD%20consequences%20of%20electrical%20shorts%20at%20the%20inner%20electrode%20system.pdf`.

[BDD$^+$13] K. Blaum, A. Doerr, C. E. Duellmann et al. *The Electron Capture ^{163}Ho Experiment ECHo*, 2013. `arXiv:arXiv:1306.2655`.

[BE17] Fabian Block, Sanshiro Enomoto. *Recommendation on FPD Rate Estimation Method for Krypton2017*. internal document, 2017.

[Beh16] J. Behrens. *Design and commissioning of a mono-energetic photoelectron source and active background reduction by magnetic pulse at the KATRIN experiment*. PhD thesis, Westfälische Wilhelms-Universität Münster, 2016.

[BGS$^+$13] S. Bauer, B. Grees, D. Spitzer et al. *Ellipsometry with polarisation analysis at cryogenic temperatures inside a vacuum chamber*. 2013. `arXiv:arXiv:1307.5879`, `doi:10.1063/1.4838555`.

[BM14] R. A. Battye, A. Moss. *Evidence for Massive Neutrinos from Cosmic Microwave Background and Lensing Observations*. Phys. Rev. Lett., 112:051303, Feb 2014. URL: `http://link.aps.org/doi/10.1103/PhysRevLett.112.051303`, `doi:10.1103/PhysRevLett.112.051303`.

[Bot12] R. Bottesch. *Set-up of the motion control and characterization of the ablation laser for the condensed ^{83m}Kr conversion electron source of the KATRIN experiment*. Diploma thesis, Westfälische Wilhelms-Universität Münster, 2012.

[BPT81] G Beamson, H Q Porter, D W Turner. *The collimating and magnifying properties of a superconducting field photoelectron spectrometer*. Journal of Physics E: Scientific Instruments, 14(2):256, 1981. URL: `http://stacks.iop.org/0022-3735/14/i=2/a=526`.

[C$^+$98] Bruce T. Cleveland, Timothy Daily, Jr. Raymond Davis et al. *Measurement of the Solar Electron Neutrino Flux with the Homestake Chlorine Detector*. Astrophys. J., 496(1):505, 1998. URL: `http://stacks.iop.org/0004-637X/496/i=1/a=505`.

[Cam01] J.L. Campbell. *Width of the atomic K–N7 levels*. Atomic Data and Nuclear Data Tables, 77(1):1–56, 2001. URL: `https://doi.org/10.1006/adnd.2000.0848`, `doi:10.1006/adnd.2000.0848`.

[Cha14] J. Chadwick. *Intensitätsverteilung im magnetischen Spektren der β-Strahlen von Radium B + C*. Verhandlungen der Deutschen Physikalischen Gesellschaft, 16:383–391, 1914.

[col12a] ATLAS collaboration. *Combined search for the Standard Model Higgs boson using up to* $4.9\ fb^{-1}$ *of pp collision data at* $s = 7\,\mathrm{TeV}$ *with the ATLAS detector at the LHC*. Physics Letters B, 710(1):49 – 66, 2012. URL: `http://www.sciencedirect.com/science/article/pii/S0370269312001852`, doi:`https://doi.org/10.1016/j.physletb.2012.02.044`.

[col12b] CMS collaboration. *Combined results of searches for the standard model Higgs boson in pp collisions at* $s = 7\,\mathrm{TeV}$. Physics Letters B, 710(1):26 – 48, 2012. URL: `http://www.sciencedirect.com/science/article/pii/S0370269312002055`, doi:`https://doi.org/10.1016/j.physletb.2012.02.064`.

[CRH$^+$56] C. L. Cowan, F. Reines, F. B. Harrison et al. *Detection of the Free Neutrino: a Confirmation*. Science, 124(3212):103–104, 1956. URL: `http://science.sciencemag.org/content/124/3212/103`, arXiv:`http://science.sciencemag.org/content/124/3212/103.full.pdf`, doi:`10.1126/science.124.3212.103`.

[Cry17] LakeShore Cryotronics. *Cernox product page*, 2017. URL: `https://www.lakeshore.com/products/cryogenic-temperature-sensors/cernox/models/pages/overview.aspx`.

[D$^+$14] S. Dyba et al. *Repair of electrical short-circuits in wire electrode system - status and perspectives*. Technical report, Westfälische Wilhelms-Universität Münster, 2014. URL: `https://fuzzy.fzk.de/bscw/bscw.cgi/d931902/30-WRP-3506-01-Wire_Electrode_Repair_Report-DRAFT-V2014-07-21.pdf`.

[DEF$^+$15] S. Dyba, M. Erhard, F. Fränkle et al. *Shifted AP Spectroscopy*, Jul 2015. electronic logbook (internal site). URL: `https://neutrino.ikp.kit.edu:8080/SDS-Measurements+Phase+2/152`.

[DEH$^+$15] S. Dyba, M. Erhardt, D. Hilk et al. *Shift of the Analyzing Plane*, Jan 2015. electronic logbook (internal site). URL: `https://neutrino.ikp.kit.edu:8080/SDS-Measurements+Phase+2/80`.

[DGMR13] P. S. Bhupal Dev, Srubabati Goswami, Manimala Mitra et al. *Constraining neutrino mass from neutrinoless double beta decay*. Phys. Rev. D, 88:091301, Nov 2013. URL: `https://link.aps.org/doi/10.1103/PhysRevD.88.091301`, doi:`10.1103/PhysRevD.88.091301`.

[DHMW08] G. Drexlin, V. Hannen, S. Mertens et al. *Current Direct Neutrino Mass Experiments*. Advances in High Energy Physics, 71(2013):39, 2008. URL: `https://doi.org/10.1155/2013/293986`.

[DHRW14] S. Dyba, D. Hilk, P. Ranitzsch et al. *Potentials for dual layer mode*, Dec 2014. electronic logbook (internal site). URL: `https://neutrino.ikp.`

`kit.edu:8080/SDS-Measurements+Phase+2/44`.

[DKR$^+$15] S. Dyba, M. Kraus, P. Ranitzsch et al. *Double layer inner wire electrode testing during cooldown*, Feb 2015. electronic logbook (internal site). URL: `https://neutrino.ikp.kit.edu:8080/SDS-Measurements+Phase+2/110`.

[Dre15] G. Drexlin. *Excited Molecules and Atoms as background source*. Technical report, Karlsruhe Institut für Technologie, 2015. URL: `fuzzy.fzk.de/bscw/bscw.cgi/d950495/95-TRP-5833-D1.3-GDrexlin.pptx`.

[DRHK14] S. Dyba, P. Ranitzsch, F. Harms et al. *Background with dual wire electrode on west side*, Dec 2014. electronic logbook (internal site). URL: `https://neutrino.ikp.kit.edu:8080/SDS-Measurements+Phase+2/46`.

[DRTO15] S. Dyba, P. Ranitzsch, N. Trost et al. *Tank Potential Survey for Shifted AP*, Jul 2015. electronic logbook (internal site). URL: `https://neutrino.ikp.kit.edu:8080/SDS-Measurements+Phase+2/151`.

[EBB$^+$14] M Erhard, S Bauer, A Beglarian et al. *High-voltage monitoring with a solenoid retarding spectrometer at the KATRIN experiment*. Journal of Instrumentation, 9(06):P06022, 2014. URL: `http://stacks.iop.org/1748-0221/9/i=06/a=P06022`.

[EBB$^+$18] M. Erhard, J. Behrens, S. Bauer et al. *Technical design and commissioning of the KATRIN large-volume air coil system*. Journal of Instrumentation, 13(02):P02003, 2018. URL: `http://stacks.iop.org/1748-0221/13/i=02/a=P02003`.

[Erh16] M. Erhard. *Influence of the magnetic field on the transmission characteristics and the neutrino mass systematic of the KATRIN experiment*. PhD thesis, Karlsruhe Institut für Technologie, 2016.

[F$^+$98] Y. Fukuda, T. Hayakawa, E. Ichihara et al. *Evidence for Oscillation of Atmospheric Neutrinos*. Phys. Rev. Lett., 81:1562–1567, Aug 1998. URL: `http://link.aps.org/doi/10.1103/PhysRevLett.81.1562`, `doi:10.1103/PhysRevLett.81.1562`.

[Fed19] M. Fedkevych. *doctoral thesis in preparation*. PhD thesis, Westfälische Wilhelms-Universität Münster, 2019.

[Fer34] E. Fermi. *Versuch einer Theorie der β-Strahlen. I.* Z. Phys., 88(3):161–177, Mar 1934. URL: `http://link.springer.com/article/10.1007/BF01351864`, `doi:10.1007/BF01351864`.

[FGT$^+$17] Daniel Furse, Stefan Groh, Nikolaus Trost et al. *Kassiopeia: a modern, extensible C++ particle tracking package*. New Journal of Physics, 19(5):053012, 2017. URL: `http://stacks.iop.org/1367-2630/19/i=5/a=053012`.

[Fis14] Sebastian Fischer. *Commissioning of the KATRIN Raman system and* *durability studies of optical coatings in glove box and tritium atmospheres*. PhD thesis, 2014.

[Fla04] B. Flatt. *Voruntersuchungen zu den Spektrometern des KATRIN-Experiments*. PhD thesis, Johannes Gutenberg-Universität Mainz, 2004.

[For12] Richard G Forbes. *Extraction of emission parameters for large-area field emitters, using a technically complete Fowler–Nordheim-type equation*. Nanotechnology, 23(9):095706, 2012. URL: `http://stacks.iop.org/0957-4484/23/i=9/a=095706`.

[FTF+17] M. Fedkevych, L. Thorneand, F. Fränkle et al. *CKrS line scans on 2017-07-12*, Jul 2017. electronic logbook (internal site). URL: `https://neutrino.ikp.kit.edu:8080/KryptonJuly17/67`.

[Ful19] A. Fulst. *doctoral thesis in preparation*. PhD thesis, Westfälische Wilhelms-Universität Münster, 2019.

[Gal88] T F Gallagher. *Rydberg atoms*. Reports on Progress in Physics, 51(2):143, 1988. URL: `http://stacks.iop.org/0034-4885/51/i=2/a=001`.

[Gal94] Thomas F. Gallagher. *Electric fields*. page 70–102, 1994. `doi:10.1017/CBO9780511524530.007`.

[GBB+10] W. Gil, J. Bonn, B. Bornschein et al. *The Cryogenic Pumping Section of the KATRIN Experiment*. IEEE Transactions on Applied Superconductivity, 20(3):316–319, June 2010. `doi:10.1109/TASC.2009.2038581`.

[GBD+13] L. Gastaldo, K. Blaum, A. Doerr et al. *The Electron Capture* ^{163}*Ho Experiment ECHo: an overview*. 2013. `arXiv:arXiv:1309.5214`, `doi:10.1007/s10909-014-1187-4`.

[Glü] F. Glüeck. *The electric shielding factor of the wire electrode*. internal document.

[Glü15] F. Glück. *Calculation of H atom Rydberg state transitions*, 2015. KATRIN Analysis Workshop (internal site)). URL: `https://fuzzy.fzk.de/bscw/bscw.cgi/d1243685/Rydberg%20transition%20simulations.pdf`.

[Gro10] S. Groh. *Untersuchung von UV-Laser induziertem Untergrund am KATRIN Vorspektrometer*. Diploma thesis, Karlsruhe Institut für Technologie, 2010.

[HAA+11] V Hannen, E Aprile, F Arneodo et al. *Limits on the release of Rb isotopes from a zeolite based 83m Kr calibration source for the XENON project*. Journal of Instrumentation, 6(10):P10013, 2011. URL: `http://stacks.iop.org/1748-0221/6/i=10/a=P10013`.

[Hac15] H. Hackenjos. *Die differentielle Pumpstrecke des KATRIN-Experiments - Inbetriebnahme und Charakterisierung des supraleitenden Magnetsystems*. Diploma thesis, Karlsruhe Institut für Technologie, 2015.

[Hac17] Moritz Thomas Hackenjos. *KATRIN "First Light" - Commissioning and Modelling of the Beamline.* PhD thesis, Karlsruher Institut für Technologie (KIT), 2017. `doi:10.5445/IR/1000078933`.

[Har14] F. Harms. *Background with baffle in pp2 cold*, Dec 2014. electronic logbook (internal site). URL: `https://neutrino.ikp.kit.edu:8080/SDS-Measurements+Phase+2/43`.

[Har15] Fabian Thomas Harms. *Characterization and Minimization of Background Processes in the KATRIN Main Spectrometer.* PhD thesis, 2015. 51.03.01; LK 01. `doi:10.5445/IR/1000050027`.

[HHW$^+$17] V. Hannen, I. Heese, C. Weinheimer et al. *Deconvolution of the energy loss function of the KATRIN experiment.* Astroparticle Physics, 89:30 – 38, 2017. URL: `http://www.sciencedirect.com/science/article/pii/S0927650517300348`, `doi:https://doi.org/10.1016/j.astropartphys.2017.01.010`.

[Hil11] B. Hillen. *Untersuchung von Methoden zur Unterdrückung des Spektrometeruntergrunds beim KATRIN Experiment.* PhD thesis, Westfälische Wilhelms-Universität Münster, 2011.

[Hil17] D. Hilk. *Electric field simulations and electric dipole investigations at the KATRIN main spectrometer.* PhD thesis, Karlsruhe Institut für Technologie, 2017.

[HM24] O. Hahn, L. Meitner. *Das β-Strahlenspektrum von Radium und seine Deutung.* Z. Physik, 26(1):161–168, 1924. URL: `https://doi.org/10.1007/BF01327324`, `doi:10.1007/BF01327324`.

[Hös16] M. Höschele. *Weiterentwicklung der Laser-Ellipsometrie für den Aufbau der neuen Krypton-Quelle an der CPS.* Bachelor’s thesis, Westfälische Wilhelms-Universität Münster, 2016.

[HOZW13] V. Hannen, H.-W. Ortjohann, M. Zacher et al. *Electrical short circuits in the main spectrometer wire electrode.* Technical report, Westfälische Wilhelms-Universität Münster, 2013. URL: `https://fuzzy.fzk.de/bscw/bscw.cgi/d875473/430-doc-3-9001-shortcircuit_report.pdf`.

[I$^+$83] J. P. Issi et al. *Electronic and lattice contributions to the thermal conductivity of graphite intercalation compounds.* Phys. Rev. B, 27(2):1333–1347, 1983.

[Jan15] Alexander Jansen. *The Cryogenic Pumping Section of the KATRIN Experiment - Design Studies and Experiments for the Commissioning.* PhD thesis, 2015.

[KBB$^+$04] Ch. Kraus, B. Bornschein, L. Bornschein et al. *Final Results from phase II of the Mainz Neutrino Mass Search in Tritium β Decay.* 2004. `arXiv:arXiv:hep-ex/0412056`, `doi:10.1140/epjc/s2005-02139-7`.

[KKK06] H. V. Klapdor-Kleingrothaus, I. V. Krivosheina. *The evidence for the observation of $0\nu\beta\beta$ decay: the identification of $0\nu\beta\beta$ events from the full spectra*. Modern Physics Letters A, 21(20):1547–1566, 2006. URL: `https://www.worldscientific.com/doi/abs/10.1142/S0217732306020937`, `arXiv:https://www.worldscientific.com/doi/pdf/10.1142/S0217732306020937`, `doi:10.1142/S0217732306020937`.

[Kle14] Marco Kleesiek. *A Data-Analysis and Sensitivity-Optimization Framework for the KATRIN Experiment*. PhD thesis, 2014.

[Kos12] Andreas Kosmider. *Tritium Retention Techniques in the KATRIN Transport Section and Commissioning of its DPS2-F Cryostat*. PhD thesis, 2012. A coherent study of the suppression methods regarding Tritium induced background in the KATRIN Experiment. Focus lies on the KATRIN Transport Section, cascaded and differential high vacuum systems, cryo-pumping, Tritium-steel-interactions and handling of ionized Tritium.

[Kra16] Marcel Kraus. *Energy-Scale Systematics at the KATRIN Main Spectrometer*. PhD thesis, Karlsruher Institut für Technologie (KIT), 2016. `doi:10.5445/IR/1000054447`.

[LBB+12] S. Lukić, B. Bornschein, L. Bornschein et al. *Measurement of the gas-flow reduction factor of the KATRIN DPS2-F differential pumping section*. Vacuum, 86(8):1126 – 1133, 2012. URL: `http://www.sciencedirect.com/science/article/pii/S0042207X11003800`, `doi:https://doi.org/10.1016/j.vacuum.2011.10.017`.

[LDH+06] X. Luo, Chr. Day, V. Hauer et al. *Monte Carlo simulation of gas flow through the KATRIN DPS2-F differential pumping system*. Vacuum, 80(8):864 – 869, 2006. URL: `http://www.sciencedirect.com/science/article/pii/S0042207X05003891`, `doi:https://doi.org/10.1016/j.vacuum.2005.11.044`.

[Lei14] Benjamin Leiber. *Investigations of background due to secondary electron emission in the KATRIN-experiment*. PhD thesis, 2014.

[Lin15] J. Linek. *Investigation of the muon induced background at the KATRIN main spectrometer*. Master's thesis, Karlsruhe Institut für Technologie, 2015.

[LP06] J. Lesgourgues, S. Pastor. *Massive neutrinos and cosmology*. Phys. Rep., 429(6):307 – 379, 2006. URL: `http://www.sciencedirect.com/science/article/pii/S0370157306001359`, `doi:10.1016/j.physrep.2006.04.001`.

[LS85] V.M. Lobashev, P.E. Spivak. *A method for measuring the electron antineutrino rest mass*. Nuclear Instruments and Methods in Physics Research Section A: Accelerators, Spectrometers, Detectors and Associated Equipment, 240(2):305 – 310, 1985. URL: `http://www.sciencedirect.com/`

science/article/pii/0168900285906400, doi:https://doi.org/10.1016/0168-9002(85)90640-0.

[M+62] Ziro Maki et al. *Remarks on the Unified Model of Elementary Particles.* Progress of Theoretical Physics, 28(5):870–880, 1962. URL: http://ptp.oxfordjournals.org/content/28/5/870.abstract, doi:10.1143/PTP.28.870.

[MAC14] CARLA and MACOLINO. *RESULTS ON NEUTRINOLESS DOUBLE-BETA DECAY FROM GERDA PHASE I.* Modern Physics Letters A, 29(01):1430001, 2014. URL: https://www.worldscientific.com/doi/abs/10.1142/S0217732314300018, arXiv:https://www.worldscientific.com/doi/pdf/10.1142/S0217732314300018, doi:10.1142/S0217732314300018.

[McC15] E.A. McCutchan. *Nuclear Data Sheets for A = 83.* Nuclear Data Sheets, 125:201 – 394, 2015. URL: http://www.sciencedirect.com/science/article/pii/S0090375215000034, doi:https://doi.org/10.1016/j.nds.2015.02.002.

[Mei24] L. Meitner. *Über die Rolle der* γ*-Strahlen beim Atomzerfall.* Z. Physik, 26(1):169–177, 1924. URL: https://doi.org/10.1007/BF01327325, doi:10.1007/BF01327325.

[Nob95] *The Nobel Prize in Physics 1995 – Press Release*, 1995. Nobelprize.org. URL: http://www.nobelprize.org/nobel_prizes/physics/laureates/1995/press.html?

[Nob02] *The Nobel Prize in Physics 2002 – Press Release*, 2002. Nobelprize.org. URL: http://www.nobelprize.org/nobel_prizes/physics/laureates/2002/press.html?

[Nob08] *The Nobel Prize in Physics 2008 – Press Release*, 2008. Nobelprize.org. URL: http://www.nobelprize.org/nobel_prizes/physics/laureates/2008/press.html?

[Nob15] *The Nobel Prize in Physics 2015 – Press Release*, 2015. Nobelprize.org. URL: http://www.nobelprize.org/nobel_prizes/physics/laureates/2015/press.html?

[OG14] K.A. Olive, Particle Data Group. *Review of Particle Physics.* Chin. Phys. C, 38(9):090001, 2014. 2015 update. URL: http://stacks.iop.org/1674-1137/38/i=9/a=090001, doi:10.1088/1674-1137/38/9/090001.

[Oly15] Olympus. *Zoom-Schwenkprisma Boreskope*, 2015. Product page. URL: https://www.olympus-ims.com/de/zoom-swing-prism-borescopes/.

[Ost08] B. Ostrick. *Eine kondensierte* ^{83m}*Kr-Kalibrationsquelle für das KATRIN-Experimen.* PhD thesis, Westfälische Wilhelms-Universität Münster, 2008.

[OW08] E W Otten, C Weinheimer. *Neutrino mass limit from tritium β-decay*. Reports on Progress in Physics, 71(8):086201, 2008. URL: `http://stacks.iop.org/0034-4885/71/i=8/a=086201`.

[P+92a] A. Picard et al. *A solenoid retarding spectrometer with high resolution and transmission for keV electrons*. Nuclear Instruments and Methods in Physics Research Section B: Beam Interactions with Materials and Atoms, 63(3):345–358, 1992. URL: `https://doi.org/10.1016/0168-583X(92)95119-C`, `doi:10.1016/0168-583X(92)95119-C`.

[P+92b] A. Picard et al. *Precision measurement of the conversion electron spectrum of ^{83m}Kr with a solenoid retarding spectrometer*. Z. Physik A - Hadrons and Nuclei, 342(1):71–78, 1992. URL: `https://doi.org/10.1007/BF01294491`, `doi:10.1007/BF01294491`.

[Pau30] W. Pauli. *Offener Brief an die Gruppe der Radioaktiven bei der Gauvereins-Tagung zu Tübingen*, Dez 1930. URL: `https://cds.cern.ch/record/83282?ln=fr`.

[PD+15] Nathalie Palanque-Delabrouille, Christophe Yèche, Julien Baur et al. *Neutrino masses and cosmology with Lyman-alpha forest power spectrum*. J. Cosmol. Astropart. Phys., 2015(11):011, 2015. URL: `http://stacks.iop.org/1475-7516/2015/i=11/a=011`, `doi:10.1088/1475-7516/2015/11/011`.

[Pet15] S. Peters. *Adaption of the PC-Ellipsometry for the Condensed Krypton Calibration Source Setup, Converted for the Operation at the KATRIN-Experiment*. Bachelor's thesis, Westfälische Wilhelms-Universität Münster, 2015.

[Pol18] A Pollithy. *Characterizing the residual background in KATRIN*. Talk at 34. KATRIN Collaboration Meeting, Karlsruhe, 29 Oct 2013, 2018.

[Pra11] M. Prall. *Background Reduction of the KATRIN Spectrometers: Transmission Function of the Pre-Spectrometer and Systematic Tests of the Main-Spectrometer Wire Electrode*. PhD thesis, Westfälische Wilhelms-Universität Münster, 2011.

[R+78a] F. Rösel et al. *Internal conversion coefficients for all atomic shells*. Atomic Data and Nuclear Data Tables, 21(2-3):91–289, 1978. URL: `https://doi.org/10.1016/0092-640X(78)90034-7`, `doi:10.1016/0092-640X(78)90034-7`.

[R+78b] F. Rösel et al. *Internal conversion coefficients for all atomic shells*. Atomic Data and Nuclear Data Tables, 21(4):291–514, 1978. URL: `https://doi.org/10.1016/0092-640X(78)90009-8`, `doi:10.1016/0092-640X(78)90009-8`.

[Rei09] S. Reimer. *Ein elektrostatisches Dipolsystem zur Eliminierung von Ionen in der DPS2-F des KATRIN Experimentes*. Diploma thesis, Karlsruhe

Institut für Technologie, 2009.

[Res17] O. Rest. *HV ripple during 2017 krypton campagin*. 2017.

[Res19] R. Rest. *doctoral thesis in preparation*. PhD thesis, Westfälische Wilhelms-Universität Münster, 2019.

[RFD$^+$17] P. Ranitzsch, F. Fränkle, M. Deffert et al. *first look at the condensed Krypton source*, Jul 2017. electronic logbook (internal site). URL: `https://neutrino.ikp.kit.edu:8080/KryptonJuly17/60`.

[RK$^+$18] P. Ranitzsch, L. Kippenbrock et al. *Gamma-induced backgrounds in the KATRIN Main Spectrometer*. 2018. paper in preparation.

[RRT17] C. Rodenbeck, O. Rest, T. Thümmler. *Ripple of Precision Supply*, Jul 2017. electronic logbook (internal site). URL: `https://neutrino.ikp.kit.edu:8080/High-Voltage/19`.

[SBB$^+$13] R. W. Schnee, M. A. Bowles, R. Bunker et al. *Removal of long-lived ^{222}Rn daughters by electropolishing thin layers of stainless steel*. AIP Conference Proceedings, 1549(1):128–131, 2013. URL: `https://aip.scitation.org/doi/abs/10.1063/1.4818092`, `arXiv:https://aip.scitation.org/doi/pdf/10.1063/1.4818092`, `doi:10.1063/1.4818092`.

[Sch17] S. Schindler. *Aufbau und Funktionstest des CKrS-Positionssystems für das KATRIN-Experiment*. Master's thesis, Westfälische Wilhelms-Universität Münster, 2017.

[SGW13] Th. Thümmler S. Görhardt, J. Wolf. *Vacuum Conditioning of the KATRIN Main Spectrometer*. Technical report, Forschungszentrum Karlsruhe, 2013. URL: `https://fuzzy.fzk.de/bscw/bscw.cgi/d875469/430-doc-3-9000-MainSpec-Baking-Report-2013-03-09.pdf`.

[Sle13] M. Slezák. *The source of monoenergetic electrons for the monitoring of spectrometer in the KATRIN neutrino experiment*. Diploma thesis, Karlsruhe Institut für Technologie, 2013.

[Sle15] M. Slezák. *Monitoring of the energy scale in the KATRIN neutrino experiment*. PhD thesis, Czech Academy of Sciences, 2015.

[SMBFP17] H. Seitz-Moskaliuk, J. Behrens, M. Fedkevych et al. *CKrS measurements of Thu July 13*, Jul 2017. electronic logbook (internal site). URL: `https://neutrino.ikp.kit.edu:8080/KryptonJuly17/72`.

[Spi11] D. Spitzer. *Alternative Ellipsometrie-Varianten bei kryogenen Temperaturen für das KATRIN-Experiment*. Diploma thesis, Westfälische Wilhelms-Universität Münster, 2011.

[Tay66] R. Taylor. *The thermal conductivity of pyrolytic graphite*. The Philosophical Magazine: A Journal of Theoretical Experimental and Applied Physics, 13(121):157–166, 1966. URL: `https://doi.org/10.1080/`

`14786436608211993`, `doi:10.1080/14786436608211993`.

[Thü07] T. Thümmler. *Präzisionsüberwachung und Kalibration der Hochspannung für das KATRIN-Experiment*. PhD thesis, Westfälische Wilhelms-Universität Münster, 2007.

[Tro18] N. Trost. *doctoral thesis in preparation*. PhD thesis, Karlsruher Institut für Technologie (KIT), 2018.

[V⁺15] P. Vogel, L.J. Wen, C. Zhang. *Neutrino oscillation studies with reactors*. Nat. Commun., 6(6935), Apr 2015. URL: `http://www.nature.com/articles/ncomms7935`, `doi:10.1038/ncomms7935`.

[Val09] K. Valerius. *Spectrometer-related background processes and their suppression in the KATRIN experiment*. PhD thesis, Westfälische Wilhelms-Universität Münster, 2009.

[vBH10] O. von Baeyer, O. Hahn. *Magnetische Linienspektren von P-Strahlen*. Z. Physik, 11:488–493, 1910.

[VD⁺06] A. Vénos, O. Dragoun et al. *Precise energy of the weak 32 keV gamma transition observed in ^{83m}Kr decay*. Nuclear Instruments and Methods in Physics Research Section A, 560:352–359, 2006.

[VGH⁺76] S. Väisälä, G. Graeffe, J. Heinonen et al. *Levels of $^{83}\mathrm{Kr}$ populated in the decay of $^{83}\mathrm{Rb}$ and $^{83}\mathrm{Br}$*. Phys. Rev. C, 13:372–376, 1976. URL: `https://link.aps.org/doi/10.1103/PhysRevC.13.372`, `doi:10.1103/PhysRevC.13.372`.

[WA03] K. Winter, G. Altarelli. *Neutrino Mass*. Springer-Verlag Berlin Heidelberg, 2003.

[WAH⁺57] C. S. Wu, E. Ambler, R. W. Hayward et al. *Experimental Test of Parity Conservation in Beta Decay*. Phys. Rev., 105:1413–1415, 1957. URL: `https://link.aps.org/doi/10.1103/PhysRev.105.1413`, `doi:10.1103/PhysRev.105.1413`.

[Wan13] N. Wandkowsky. *Study of background and transmission properties of the KATRIN spectrometers*. PhD thesis, 2013.

[Z⁺13] M. Zbořil et al. *Ultra-stable implanted ^{83}Rb / ^{83m}Kr electron sources for the energy scale monitoring in the KATRIN experiment*. Journal of Instrumentation, 8(03):P03009, 2013. URL: `http://stacks.iop.org/1748-0221/8/i=03/a=P03009`.

[Zac09] M. Zacher. *Electromagnetic design and field emission studies for the inner electrode system of the KATRIN main spectrometer*. Diploma thesis, Westfälische Wilhelms-Universität Münster, 2009.

[Zac14] M. Zacher. *High-field electrodes design and an angular-selective photoelectron source for the KATRIN spectrometers*. PhD thesis, Westfälische Wilhelms-Universität Münster, 2014.

[Zbo11] M. Zbořil. *Solid electron sources for the energy scale monitoring in the KATRIN experiment*. PhD thesis, Westfälische Wilhelms-Universität Münster, 2011.